High-Resolution Tandem Mass Spectrometry of Complex Mixtures with a Multiple-Reflection Time-of-Flight Mass-Spectrometer

Inauguraldissertation zur Erlangung des Doktorgrades der
Naturwissenschaftlichen Fakultät Justus-Liebig-Universität Gießen

vorgelegt von

Julian Bergmann
geboren in Gießen

Fachbereich 07 - Mathematik und Informatik, Physik, Geographie
II. physikalisches Institut Justus-Liebig-Universität Gießen

February 20, 2024

Betreuer: Prof. Dr. Christoph SCHEIDENBERGER
Justus-Liebig-Universität Gießen
GSI Helmholtzzentrum für Schwerionenforschung in Darmstadt

2. Gutachter: Prof. Dr. Wolfgang SCHRADER
Max-Planck-Institut für Kohlenforschung in Mülheim an der Ruhr

3. Prüfer: Prof. Dr. Michael DÜRR
Justus-Liebig-Universität Gießen

4. Prüfer: Prof. Dr. Christian FISCHER
Justus-Liebig-Universität Gießen

Contents

Zusammenfassung

In dieser Arbeit wurde ein Mehrfachreflexions-Flugzeit-Massenspektrometer (MR-TOF-MS) angepasst und zum ersten Mal für die analytische Tandem-Massenspektrometrie mit ultrahoher Auflösung eingesetzt, um isobare Moleküle in einer schweren Rohölprobe zu analysieren. Dank des ultrahohen Präkursor-Separationsvermögens des Geräts und fortschrittlicher Datenanalysetechniken konnten neue Strukturformeln ermittelt werden.

Eine neue Ionen-Schnittstelle für athmospherischen Druck (API) wurde gebaut, um mehrere Ionenquellen parallel zu betreiben und den Transport für viskose Proben zu optimieren. Dabei bietet Ein Radiofrequenz Carpet eine effiziente Methode, Ionenquellen zu kombinieren und weiter zur Analyse zu führen. Der parallele Betrieb vermeidet dabei chemische Reaktionen zwischen Kalibranten und Analyten.

Für den Betrieb des Geräts sowie für die Aufnahme und Analyse von Massenspektren wurde ein Softwarepaket entwickelt. Die Software ermöglicht dabei die automatische Einrichtung der Messung anhand direkter Eingabe der gwünschten Mess-Parameter wie z.B. der gewünschte Massenbereich. Weitere automatisierte Messfunktionen sind eine Flugzeitdriftkorrektur, ein Scannen der Messparameter und eine automatische Gain-Control. Darüber hinaus biete die Software zwecks Analyse eine zeitaufgelöste Kalibrierungstechnik und eine erweiterte Bestimmung der Elementzusammensetzung. Außerdem wurden Datenanalyseverfahren entwickelt, um den Massenbereich zu vergrößern und gleichzeitig eine hohe Massengenauigkeit und ein hohes Massenauflösungsvermögen für beizubehalten. Auch an Teilchenbeschleunigern mit MR-TOF-MS-Geräten wird diese Software eingesetzt, z. B. das MR-TOF-MS des FRS Ion Catcher an der GSI in Darmstadt und das MR-TOF-MS des TITAN-Experiments am TRIUMF in Vancouver.

Das Gerät in dieser Arbeit besitzt ein Massenauflösungsvermögen (FWHM) von bis zu 300 000, eine Empfindlichkeit von 10 mol/l, einen linearen Dynamikbereich von 5 Größenordnungen und eine Massengenauigkeit von 0.3 ppm. Die neuartige Re-Trapping-Technik ermöglicht ein Präkursor-Separationsvermögens von bis zu 250 000 bei einer Effizienz von 10 % oder bis zu 100 000 mit einer Effizienz von 80 % bir zur vierten Stufe (MS^4). Außerdem wurden schweren Moleküle wie Humaninsulin (5810 u) analysiert.

Tandem-Massenspektrometrie (MS^2) wurde für eine Probe von Rückständen mittelschwerem Rohöls durchgeführt, und vier isobare Massensignale nahe 322.2 u/e mit einem Isolationsfenster von 10 mu und einem Unterdrückungsfaktor von 200 isoliert mithilfe des ultrahohen Präkursor-Separationsvermögens isoliert. Die erzeugten Fragmente innerhalb des Massenbereichs von 300 - 500 u wurden mit einem Massenauflösungsvermögen von 200 000 und einer Massengenauigkeit von besser als 1 ppm gemessen und ihre elementare Zusammensetzung bestimmt.

Mit die Zusammenarbeit mit der Arbeitsgruppe *Massenspektrometrie* von Prof. Dr. Wolfgang Schrader am Max-Planck-Institut für Kohleforschung in Mülheim an der Ruhr wurden 26 Molekülstrukturen für die beiden isobaren Präkursor-Moleküle, $C_{23}H_{32}N^+$ und $C_{23}H_{28}ON^+$, identifiziert. Für künftige Anwendungen des Geräts sind die Untersuchung von weniger bekannten Rohölproben sowie Anwendungen in den Biowissenschaften vorgesehen.

Abstract

In this work, a multiple-reflection time-of-flight mass spectrometer (MR-TOF-MS) was adapted and employed, for the first time, for ultra-high resolution analytical tandem mass spectrometry. The device was deployed to analyze isobaric molecules in a heavy crude oil sample and to derive new structure formulas thanks to the device's ultra-high separation power and advanced data analysis techniques.

A new atmospheric pressure interface (API) was built to operate multiple ion sources in parallel and to optimize the transmission for viscous samples, like crude oil residue. A radio-frequency carpet funnels the ions to the RFQ transport line, providing a compact, efficient, and fast method to combine ions from different sources in parallel to introduce calibrants, while avoiding chemical reactions with the analyte. Ion sources of three different types, nano-ESI, micro-ESI, and thermal ^{133}Cs, were designed, built, coupled to the API, and operated to acquire the data shown in this thesis.

A software package was developed for operating the device and for acquiring and analyzing mass spectra. The software allows automatically setting up the measurement by converting parameters like the desired mass range to voltages and HV pulse sequences in real time. Further automated measurement features are a time-of-flight drift correction, a scanning of measurement parameters, and an automatic gain control. In addition, its calibration technique and its enhanced elemental composition identification further assist in analysis. Furthermore, data analysis procedures were developed to increase the mass range, while retaining a high mass accuracy and mass resolving power for closed-path MR-TOF-MS. The software is also used together with MR-TOF-MS devices at particle accelerators, i.e. the MR-TOF-MS of the FRS Ion Catcher at GSI, Darmstadt, and the MR-TOF-MS of the TITAN experiment at TRIUMF in Vancouver.

The device in this work features a mass resolving power (FWHM) of up to 300 000, a sensitivity down to 10 mol/l, a linear dynamic range of 5 orders of magnitude, and mass accuracy of 0.3 ppm. Its re-trapping technique allows for a precursor mass separation power of up to 250 000 at an efficiency of 10 % or up to 100 000 with an efficiency of 80 % for tandem mass spectrometry. These capabilities were shown for tandem mass spectrometry measurements up to the fourth stage (MS^4). Furthermore, molecules as heavy as human insulin (5810 u) have been analyzed.

Tandem mass spectrometry of a sample of medium-heavy crude oil residue was performed and four isobaric mass signals close to 322.2 u/e were isolated with an isolation window of 10 mu and a suppression factor of 200. This was only possible thanks to this device's ultra-high mass separation power. The resulting fragments within a mass range of 300 - 500 u were measured at a mass resolving power of 200 000 and a mass accuracy of better than 1 ppm, and their elemental compositions were identified. With the help of our collaboration with the workgroup *Mass Spectrometry* of Prof. Dr. Wolfgang Schrader at the Max Planck Institute für Kohleforschung in Mülheim an der Ruhr, 26 molecular structures for the two isobaric precursor molecules, $C_{23}H_{32}N^+$ and $C_{23}H_{28}ON^+$, were identified. For future applications of the device, investigation of less understood crude oil samples as well as applications in life sciences are envisioned.

1 Motivation

Mass spectrometry has become an integral part of many fields of today's science due to its ability to determine exact mass values and the relative abundance of atoms and molecules. For this purpose, different instrumental approaches nowadays offer a variety of techniques with distinct advantages for each field's requirements. Multiple-reflection time-of-flight mass spectrometers (MR-TOF-MS) receive increasing interest and application due to their unique combination of performance advantages.

In nuclear physics, mass spectrometers are often utilized at particle accelerators for high-precision mass measurements of short-lived nuclei [YAMAGUCHI et al. 2021]. The particle binding energy B can be derived from the exact mass value's difference from the sum of the masses of its constituents [WEIZSÄCKER 1935]. For an atom with N neutrons of mass m_n and Z protons of mass m_p, the binding energy is given by

$$N \cdot m_n + Z \cdot m_p + \frac{B(N,Z)}{c^2} \quad . \tag{1.0.1}$$

With knowledge of the binding energy, insights into nuclear structure and verification of nuclear models are obtained. It also gives key information for the understanding of the creation of elements in the universe. Due to its short measurement time, high sensitivity, and broadband measurement capability, the MR-TOF-MS has become an efficient instrument at many accelerator facilities [PLASS, T. DICKEL, PURUSHOTHAMAN, et al. 2013; JESCH et al. 2015; SCHURY et al. 2009; WOLF, ERRIT, et al. 2011; PLASS, T. DICKEL, AYET SAN ANDRÉS, et al. 2015].

The combination of a highly sensitive broadband mass spectrometer with a high mass resolving power and short measurement time is also attractive for analytical mass spectrometry, for example, in life science or for studying complex samples like heavy crude oil. Tandem mass spectrometry investigates bond energies, fragmentation pathways, and molecule structure by isolating precursor ions that are then dissociated and their product ions measured. By utilizing the novel technique of re-trapping [Timo DICKEL et al. 2017], an MR-TOF-MS can apply tandem mass spectrometry with a highly-resolved precursor-selection stage. Typical commercial mass spectrometers usually provide only a low to medium-resolution precursor selection [GLISH et al. 2008], while a tandem MR-TOF-MS with a closed flight path can reach a high resolution in each re-trapping stage. The high mass separation power allows precursor molecules to be isolated with a mass window range of down to a few mu, allowing the isolation of individual isobars, whereas conventional instruments have isolation windows of about 0.5 u/e.

This work focuses on extending the capabilities of an MR-TOF-MS for analytical mass spectrometry [Timo DICKEL et al. 2017] and for the first time providing high resolution MS^4 in an MR-TOF-MS and highly accurate data on structural analysis of crude oil with the device. Furthermore, a specialized software package was developed to provide extended hardware control, specialized data acquisition, and semi-automated data analysis. In addition, a new atmospheric pressure interface was built and commissioned, utilizing various ion sources and inlets and using the novel design of a radio frequency carpet for transportation.

2 Basic Principles

2.1 Special Terms

This thesis follows the IUPAC recommendations of 2013 for mass spectrometry terminology [Murray et al. 2013]. The following section will explain deviations and extensions.

Mass Value

Mass m is a body property and determines its resistance to acceleration.

The SI unit for mass is the kilogram, which since 2019 has been defined by natural constants [EU-directive 2019]. It is derived from the Planck constant h of $6.626\,070\,15 \cdot 10^{-34}\,\frac{\mathrm{kg\,m^2}}{\mathrm{s}}$.

For measurements in the molecular mass scale, the atomic mass unit u is usually chosen, defined as 1/12 of the mass of a free ^{12}C ground-state atom. One u equals $1.660\,538\,86(28) \cdot 10^{-27}\,\mathrm{kg}$ [units 2006].

Time-of-flight mass spectrometers measure the mass-to-charge ratio m/q, and thus, plots shown here use u/e units (atomic mass unit over electron charge). Unless stated otherwise, singly charged molecules are assumed, and mass values are given in u.

Mass Range

Mass range $m_{\mathrm{max}}/m_{\mathrm{min}}$ is a dimensionless fraction of the largest over the smallest mass that can be simultaneously measured. The fraction notation describes the capability of a mass spectrometer. The interval notation $[m_{\mathrm{min}}, m_{\mathrm{max}}]$ is used in this work to describe a specific target range.

Mass Accuracy

Mass accuracy $\delta m/m$ shows how accurate a mass value can be measured. It is given by the expected margin of error δm as the difference to the measured mass value m_{exp} over the real mass value $m_m athrmlit$ in units of ppm.

$$\frac{\delta m}{m} = \frac{m_{\mathrm{exp}} - m_{\mathrm{lit}}}{m_{\mathrm{lit}}} \tag{2.1.1}$$

Sensitivity

Sensitivity describes the lowest concentration of an analyte within dissolved samples that a device can detect, typically given in terms of *ppm* of volume or units of mol/l.

Mass Resolving Power

Mass resolving power MRP describes how well a mass spectrometer can resolve two ion species with adjacent masses. It is expressed as a fraction of the mass value over the minimum distance Δm between masses that can still be resolved [Murray et al. 2013]. In this thesis, two mass signals are defined as resolved when their determined value exceeds their signal form's full width at half of its maximum $FWHM$.

$$MRP = \frac{m}{\Delta m} = \frac{m}{FWHM} \tag{2.1.2}$$

Linear Dynamic Range

The *linear dynamic range* describes an interval of concentration in which the detected signal intensity is proportional to the analyte concentration. Measurements of composition or identification by branching ratios require operation inside the linear region. Non-linear effects range from electrical and chemical noise at low concentrations to saturations of detector or digitizer and space charge effects at high concentrations.

2.2 Mass Spectrometers

A *mass spectrometer* is a device capable of measuring the spectrum of masses of molecules or atoms inside a sample.

In all cases relevant to this work, measured molecules and atoms need to be ionized, which leads to spectra depicting abundances (ordinate) against the mass-to-charge ratio m/q.

To measure a spectrum, most devices, including the one in this work, are separated into four main parts:

1. An *Ion Source* (see Section 2.4) that prepares, ionizes the sample.
2. A *Beam Preparation System* (see Section 3.4) for collecting, filtering, cooling, bunching, and injecting ions into the analyzer.
3. An *Analyzer* (see Section 2.6.2) capable of separating ions according to their mass-to-charge ratios in time or space.
4. A *Detector System* (see Section 2.7) to detect and quantify the ions, making its data further processable.

2.3 Tandem Mass Spectrometry

An effective technique to investigate fragmentation pathways of molecules and molecular structure is *tandem mass spectrometry* (also tandem-MS or MS^N).

Tandem mass spectrometry denotes two or more (N) consecutive stages of mass separation between which molecular fragmentation is applied.In each but the final stage, a precursor ion is isolated, dissociated, and the product ions are prepared for the next stage. The final stage records the mass spectrum.

Examining the resulting fragmentation spectrum for specific patterns or dissociation energy dependence allows conclusions about the precursor's molecular structure and fragmentation pathways.

While there are tandem mass spectrometers with two separate analyzers (tandem-in-space), the device in this work uses the same trap and analyzer for each stage (tandem-in-time). After their re-capture inside the trap, collision-induced dissociation fragments the isolated precursor molecules(see Section 2.5.3), which, once sufficiently cooled again, are injected into the analyzer for the next stage.

2.4 Ion Sources

The device used in this work allows for a modular combination of different ion sources. The following section will give an overview of the ionization techniques used.

2.4.1 Electrospray Ionization

The main type of ionization used in this work is based on *electrospray ionization* (ESI) [Dole et al. 1968].

A thin capillary with a sharp tip and a conducting surface is filled with a liquid sample. A strong electric field is generated at the capillary's tip by applying a high voltage between the capillary and the mass spectrometer inlet. In combination with the analyte's surface tension, this field causes the sample to form a *Taylor cone*. This cone emits a small liquid jet from the capillary's tip [Taylor 1964]. By solvent evaporation and coulomb fission, the jet forms highly charged droplets which, after reaching a specific surface charge density (Rayleigh limit [Rayleigh 1882]), disperse into smaller droplets and finally charged molecules [Bruins 1998].

This atmospheric ionization method allows for a soft formation of singly to multiply charged ions of even large molecules with little fragmentation [Choi et al. 2013].

ESI needles have a tip with an inner diameter of 50 - 200 µm and flow rates of 4 - 200 $\frac{\mu\mathrm{L}}{\mathrm{min}}$. High flow rates allow for higher statistics and more viscous samples but require an extra container, usually a syringe, tubing, and a pump.

Nano-ESI uses a reduces the capillary diameter of 1 - 10 µm tip size to lower the flow rate to 20 - 100 $\frac{\mathrm{nL}}{\mathrm{min}}$. The capillary force is enough at this flow rate to supply the tip with the capillary's content [Wilm et al. 1994]. This ionization method does not require a pump and improves the formation of ions [Karas et al. 2000].

2.4.2 Thermal Ionization

Increasing a sample's surface thermal energy, for example, with a metal heating filament, gives atoms a higher probability of desorption and ionization from the surface. Thermal ionization follows the Langmuir-Saha equation [Langmuir et al. 1925]:

$$p_{\text{ion}} = \left[1 + \frac{g_{\text{neutral}}}{g_{\text{ion}}} \cdot \exp\left(\frac{e(\Phi_{\text{ion}} - \Phi_W)}{k_B \cdot T}\right)\right]^{-1} \qquad (2.4.2.1)$$

with p_{ion} the probability of ionization at thermal surface equilibrium, $g_{\text{ion/neutral}}$ the total angular momentum of the ionized and neutral atom, Φ_{ion} the ionization potential, Φ_W the work function of the surface material, and T the surface temperature.

Thermal ion sources have a simple design, work reliably, and produce a stable emission rate with maximum temperatures around 2500 °C. While this thermal energy is not large enough to ionize elements with high ionization energies, it can fragment molecules and oxidize samples.

2.5 Radio Frequency Field Assisted Ion Motion

2.5.1 Radio Frequency Quadrupoles

A *Radio frequency quadrupole* (RFQ) consists of four conducting rods aligned parallel and centered around the beam axis at the same distance to each other. A radiofrequency voltage is applied to confine charged particles in the (x/y)-plane orthogonal to their transport direction (z) [Paul et al. 1956].

Opposing rods share the same potential while neighboring rods are phase-shifted by 180°. Due to the changing repelling and attracting forces, ions are forced into oscillating trajectories,

$$x = x_0 \cos(\Omega t) + (\dot{x}_0/\Omega)\sin(\Omega t) \tag{2.5.1.1}$$

$$y = y_0 \cos(\Omega t) + (\dot{y}_0/\Omega)\sin(\Omega t) \quad , \tag{2.5.1.2}$$

with Ω the applied angular frequency. For stable trajectories, ions are strongly confined within the (x/y)-plane while maintaining their velocity in the z-direction or being transported by an additional DC gradient.

These oscillations can become unstable for too high or low mass-to-charge ratios depending on RF frequency and amplitude, allowing its application as a mass filter [Mathieu 1868].

2.5.2 RFQ Mass Filter

An RFQ utilized for ion transport can also restrict transmission to ions only within a specific mass range. Since ion transport requires a stable ion motion, introducing an additional DC field to apply a mass-dependent distortion of the trajectory results in a mass range of ions transmitted through the RFQ.

With the established *Mathieu parameters*

$$q_x = -q_y = \frac{4qV}{m\Omega^2 r_0^2} \qquad \text{and} \qquad a_x = -a_y = \frac{8qU}{m\Omega^2 r_0^2} \tag{2.5.2.1}$$

the equation of motion Equation (2.5.1.1) for an electric potential on the RFQ electrodes following the form

$$\Phi(t) = \pm\left(U + V \cdot \cos(\Omega t)\right) \tag{2.5.2.2}$$

with U a direct voltage, V an alternating voltage, and Ω the applied angular frequency, can be written as Mathieu's differential equations [Mathieu 1868]

$$\frac{d^2x}{d\xi^2} + \left(a_x + 2q_x \cdot \cos(2\xi)\right)x = 0 \tag{2.5.2.3}$$

$$\frac{d^2y}{d\xi^2} + \left(a_x + 2q_x \cdot \cos(2\xi)\right)y = 0 \tag{2.5.2.4}$$

$$\xi = \frac{1}{2}\Omega t \tag{2.5.2.5}$$

with ion charge q, mass m, and r_0 distance between rod surface and beam axis.

Assuming the homogenous solution of the Mathieu equation is of the form [McLachlan 1947]

$$F(\xi) = e^{i\nu_u\xi} \cdot G(\xi) \qquad , u \in \{x, y\} \tag{2.5.2.6}$$

expanding $G(\xi)$ in a Fourier series leads to the general solution

$$u(\xi) = \lambda_u e^{\nu_u\xi} \sum_{n=-\infty}^{\infty} C_{2n,u} \cdot e^{2in\xi} + \mu_u e^{-\nu_u\xi} \sum_{n=-\infty}^{\infty} C_{2n,u} \cdot e^{-2in\xi} \tag{2.5.2.7}$$

with λ_u, μ_u constants and $C_{2n,u}$ as well as ν_u depending on q_x and a_x.

Solutions that keep Equation (2.5.2.7) finite are called stable solutions and follow the form

$$u(\xi) = \lambda_u \sum_{n=-\infty}^{\infty} C_{2n,u} \cdot \cos\left(\xi(2n+\beta_u)\right) + \mu_u \sum_{n=-\infty}^{\infty} C_{2n,u} \cdot \sin\left(\xi(2n+\beta_x)\right) \ . \tag{2.5.2.8}$$

The parameter β_u can be calculated by continued fraction expression.

$$\beta_u^2 = a_u + \cfrac{q_u^2}{(\beta_u+2)^2 - a_u - \cfrac{q_u^2}{(\beta_u+4)^2 - a_u - \cfrac{q_u^2}{(\beta_u+6)^2 - a_u - \dots}}} \tag{2.5.2.9}$$

$$+ \cfrac{q_u^2}{(\beta_u-2)^2 - a_u - \cfrac{q_u^2}{(\beta_u-4)^2 - a_u - \cfrac{q_u^2}{(\beta_u-6)^2 - a_u - \dots}}} \tag{2.5.2.10}$$

In the case $q_u < 0.4$ (Dehmelt approximation), β_u can be approximated as

$$\beta_u \approx a_u + \frac{1}{2} q_u^2 \ . \tag{2.5.2.11}$$

If β_u is small, ion motion can be approximated by a harmonic oscillation with angular frequency ω_u and the initial condition of position u_0 inside a parabolic potential well V_{pseudo} [Major et al. 1968; March et al. 2005].

$$V_{\text{pseudo}} = \frac{V q_u u^2}{4u_0^2} \qquad \omega_u = \frac{\beta_u \Omega}{2} \tag{2.5.2.12}$$

For a given set of U and V, all ions lie on the mass scan line in the stability diagram:

$$a_x = \frac{2U}{V} \cdot q_x \tag{2.5.2.13}$$

The overlap of the mass scan line with the stability region defines the transported mass range of the RFQ filter. The corresponding q_x range $[q_{x,\mathrm{min}}, q_{x,\mathrm{max}}]$ can be converted to mass-to-charge ratio by Equation (2.5.2.1):

$$\left(\frac{m}{q}\right)_{[\mathrm{max,min}]} = \frac{4V}{q_{x,[\mathrm{min,max}]}\Omega^2 r_0^2} \tag{2.5.2.14}$$

The ion motion is only stable for specific sets of the Mathieu parameters. Figure 2.5.1 shows the combinations of a_x and q_x producing, stable trajectories for $q_x \in (0, 1)$ and $a_x \in (0, 0.25)$. Ions with unstable x/y motion will not pass the RFQ filter.

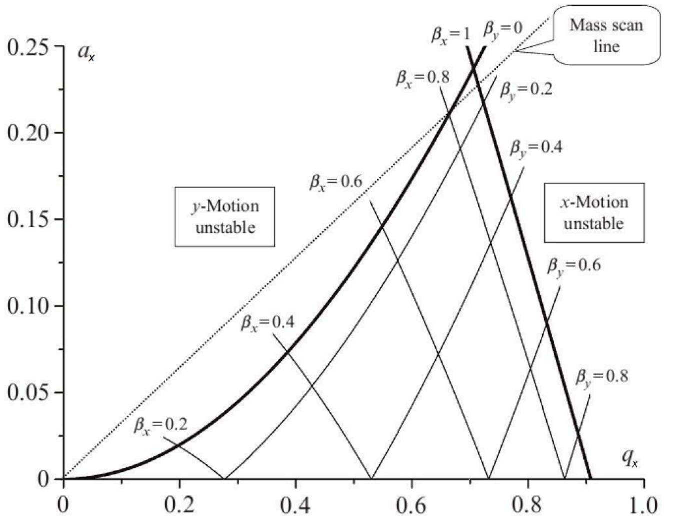

Figure 2.5.1: Stability diagram of Mathieu parameters q_x and a_x showing the first area of stable trajectories. Taken from [M. YAVOR 2009].

2.5.3 Collision-Induced Dissociation

In an RFQ, *collision-induced dissociation* (CID) can be applied to investigate molecular structures and compositions using tandem mass spectrometry.

The ion trajectory in an RFQ ion trap is composed of the two fundamental secular frequency components $\omega_{r,0}$ and $\omega_{z,0}$ [MARCH et al. 2005]:

$$\omega_{u,n} = (n + \frac{1}{2}\beta_u)\Omega \qquad \text{for } 0 \leq n < \infty \tag{2.5.3.1}$$

$$\omega_{u,n} = -(n + \frac{1}{2}\beta_u)\Omega \qquad \text{for } -\infty < n < 0 \tag{2.5.3.2}$$

$$\tag{2.5.3.3}$$

Applying an additional RF field at the secular frequency ω_0 excites resonant ion motion, which leads to higher collision energies with the neutral surrounding buffer gas. The maximum energy transfer per interaction between ion and gas molecule in the ion's center-of-mass system E_{cms} is calculated by

$$E_{\mathrm{cms}} = \frac{m_{\mathrm{gas}}}{m_{\mathrm{ion}} + m_{\mathrm{gas}}} \cdot E_{\mathrm{kin}} \tag{2.5.3.4}$$

with E_{kin} being the kinetic energy in the lab system. The induced vibrational energy spreads over the whole molecule leading to unimolecular dissociation after a few milliseconds [Wells et al. 2005]. The resulting fragments still contained in the RFQ can then be measured in the next tandem-mass-spectrometry stage. In practice, lower amplitudes at a longer duration are applied to improve trapping efficiency and resonant excitation.

2.5.4 RF Carpet

An *RF carpet* combines RF and DC-drag fields to extract a dispersed ion cloud from gas-filled chambers. This technique is used in this work's API to efficiently transport ions toward the following RFQ elements and simultaneously use multiple ion sources. The PCB layout of the RF carpet is depicted in Figure 2.5.2.

The carpet is composed of concentrically aligned ring electrodes. Neighboring rings are supplied with a 180° phase-shifted RF signal in the order of a few MHz. A DC component is added across the rings to create a drag potential toward the nozzle aperture at the carpet's center. An electrode above the carpet applies a field to push ions toward the carpet.

The RF component repels ions from the carpet's surface, similar to the motion in RF quadrupoles (Section 2.5.1). According to [Dehmelt 1967] the pseudopotential can be written as

$$V_{\mathrm{pseudo}}(r) = \frac{q}{4m\Omega^2} E^2_{\mathrm{RF}}(r) \tag{2.5.4.1}$$

with $\Omega = 2\pi f$ the angular frequency, where the RF field can be expressed as [Wada et al. 2003]

$$E_{\mathrm{RF}}(r) = \frac{r}{r_0} E_{\mathrm{max}} \qquad \text{for } 0 < r < r_0 \quad , \tag{2.5.4.2}$$

where r_0 equals half the distance between ring electrodes. The pseudopotential can be derived as

$$E_{\mathrm{pseudo}} = -\nabla V_{\mathrm{pseudo}} = -\nabla \left(\frac{q}{4m\Omega^2} \left(E_{\mathrm{max}} \frac{r}{r_0} \right)^2 \right) = \frac{qU^2_{\mathrm{RF}}}{2m\Omega^2 r_0^3} \cdot \left(\frac{r}{r_0} \right) \quad , \tag{2.5.4.3}$$

where U_{RF} is the voltage of the applied RF.

Since ions lose energy due to collisions with buffer gas atoms, a dampening coefficient γ must be defined for the effective field [Tolmachev, Chernushevich, et al. 1997].

$$E_{\mathrm{eff}} = E_{\mathrm{pseudo}} \cdot \gamma = E_{\mathrm{pseudo}} \cdot \frac{\Omega^2 \tau^2}{1 + \Omega^2 \tau^2} \tag{2.5.4.4}$$

The velocity relaxation time τ was introduced by Tolmachev with the the ion mobility κ [Tolmachev, Chernushevich, et al. 1997]:

$$\tau = \kappa \frac{m}{q} \ . \tag{2.5.4.5}$$

This relaxation time is small enough for high-pressure regions to approximate $\tau \ll \frac{1}{\Omega}$ and, therefore,

$$\frac{\Omega^2 \tau^2}{1 + \Omega^2 \tau^2} \approx \Omega^2 \tau^2 \ . \tag{2.5.4.6}$$

Thus, for fixed temperature and pressure, the effective field can be expressed by the ion mobility κ [Wada et al. 2003]

$$E_{\text{eff}} = \frac{mU_{\text{RF}}^2}{2qr_0^3} \cdot \frac{r}{r_0} \cdot \kappa^2 = \frac{mU_{\text{RF}}^2}{2qr_0^3} \cdot \frac{r}{r_0} \kappa_0^2 \frac{p_0^2}{p^2} \frac{T^2}{T_0^2} \quad , \tag{2.5.4.7}$$

with κ_0 the reduced ion mobility. and with the ideal gas law $pV = Nk_BT$ written in dependence of number density $n = N/V$:

$$E_{\text{eff}} = \frac{1}{2qk_B^2 r_0^3} \cdot \left(\frac{r}{r_0}\right) \cdot \left(\kappa_0 \frac{p_0}{T_0}\right)^2 \cdot \frac{m}{n^2} U_{\text{RF}}^2 \quad , \tag{2.5.4.8}$$

where For $r = r_0$, the first term becomes constant, and the effective potential can be simplified to

$$E_{\text{eff}} = \text{const} \cdot \frac{m}{n^2} U_{\text{RF}}^2 \tag{2.5.4.9}$$

This effective field needs to be at least as large as the DC field that pushes ions toward the carpet to keep ions from impacting and to let the DC drag field transport them toward the nozzle:

$$E_{\text{push}} \overset{!}{=} E_{\text{eff}} = \text{const} \cdot \frac{m}{n^2} U_{\text{RF}}^2 \tag{2.5.4.10}$$

For a constant pushing DC field E_{push} and a given mass m, the number density n becomes proportional to the required RF amplitude $n \propto U_0$.

An additional transport-suppressing effect on light ions is caused by their higher energy transfer during collisions with the buffer gas. Faster ions will move further than r_0 within an RF phase and impact onto the carpet [Tolmachev, Udseth, et al. 2000]. Thus lighter masses require a high frequency in addition to higher amplitudes.

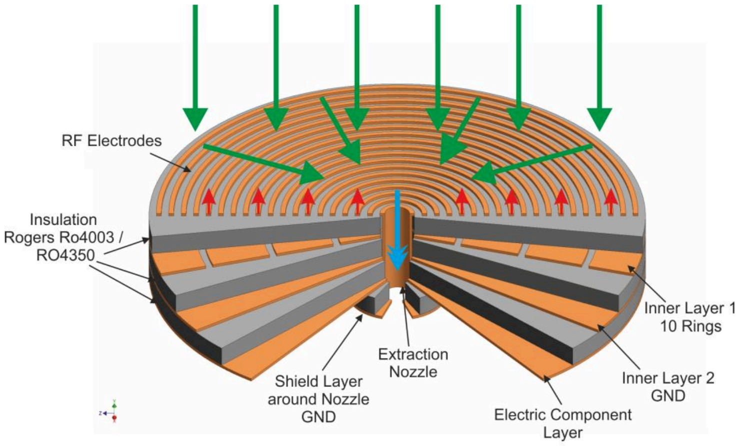

Figure 2.5.2: Schematic figure of the RF carpet, showing each layer of the PCB setup used in this device. Green arrows indicate the electric force from DC fields, namely a pushing field from the top and a dragging field toward the center. Red arrows show the repelling pseudo potential keeping the ions from impacting onto the surface. The blue arrow represents the force the gas flow applied toward the vacuum chamber below. Taken from [Reiter 2015].

2.6 Time-of-Flight Mass Spectrometry

2.6.1 Principle

Accelerating charged particles in an electric field increases their kinetic energy. For a previously resting ion at z=0, the kinetic energy can be expressed as

$$E_{\text{kin}} = q \cdot U(z) = \frac{1}{2} m \Big(v(z) \Big)^2 \qquad\qquad v(z) = \sqrt{2 \frac{q}{m} \cdot U(z)} \tag{2.6.1.1}$$

with $U(z)$ the potential difference to $U(z = 0)$, $\frac{m}{q}$ the ion mass-to-charge ratio, and $v(z)$ their velocity at position z. The velocity depends on the applied potential along its flight path z. By integrating the path of flight, we can calculate the time the ion takes to reach a specific point:

$$t = \sqrt{\frac{m}{q}} \int_s \frac{dz}{\sqrt{2U(z)}} \tag{2.6.1.2}$$

The path integral can be substituted with an effective potential U_{eff}. With the total *time-of-flight* (TOF) t_{total} and the total flight path l_{total}, the mass-to-charge ratio can be expressed as

$$\frac{m}{q} = \frac{2U_{\text{eff}}}{l_{\text{total}}} \cdot t_{\text{total}}^2 = a \cdot t^2 \tag{2.6.1.3}$$

with a as a calibration factor.

By measuring t_{total} for known masses, a can be calibrated, thus providing mass identification for measured TOF values. Due to delays caused by electric modules and cables, the measured TOF t_{exp} includes an offset t_0 as a second calibration parameter [Ayet San Andrés et al. 2019].

$$t_{\text{total}} = t_{\text{exp}} - t_0 \quad , \tag{2.6.1.4}$$

leading to the calibration equation

$$\frac{m}{q} = a \cdot (t_{\text{exp}} - t_0)^2 \quad . \tag{2.6.1.5}$$

This expression can be used to calculate the MRP in Equation (2.1.2) directly by the TOF.

$$\Delta m = \ 2at_{\text{total}} \cdot \Delta t \tag{2.6.1.6}$$

$$R = \frac{m}{\Delta m} = \frac{at_{\text{total}}^2}{2at_{\text{total}}\Delta t} = \frac{t_{\text{total}}}{\Delta t} \quad . \tag{2.6.1.7}$$

Main contributions to the FWHM Δt are the initial time spread Δt_i and time spread caused by ion-optical aberrations Δt_{ion} [Plass 1997].

$$\Delta t = \sqrt{\Delta t_i^2 + \Delta t_{\text{ion}}^2} \tag{2.6.1.8}$$

The main cause for the initial speed is the turn-around time Δt_{ta} [Plass 1997]. Due to the initial distribution of thermal velocities v, some ions fly in the opposite direction to the trap extraction as the trap opens. They move against the closed trap potential, turn around, and return to their initial position with inverted velocity. The time needed to return to this point is called turn-around time. For the mass-to-charge ratio m/q at temperature T and an extraction field strength E, it is given by

$$\Delta t_{\mathrm{ta}} = \frac{2mv}{qE} \quad , \tag{2.6.1.9}$$

and by expressing v in terms of ion temperature, the time spread can be expressed as $\Delta t_{\mathrm{ta,FWHM}}$ [Plass 1997]:

$$\Delta t_{\mathrm{ta,FWHM}} = \frac{\sqrt{8 \ln(2) \cdot m k_B T}}{qE} \quad . \tag{2.6.1.10}$$

2.6.2 Multiple-Reflection TOF-MS

To increase the MRP according to Equation (2.6.1.6), aside from lowering aberrations, one can increase the total TOF by increasing the flight path. However, high MRP requires flight paths of hundreds of meters, making a linear setup too space-consuming and expensive.

Another approach is to use electrostatic reflectors to re-use the existing space and fold the flight path into itself [Wollnik et al. 1990]. Electrostatic mirrors allow us to reflect ions several thousand times, leading to flight paths of kilometers and thus MRP of a few hundred thousand [T. Dickel 2010].

Figure 2.6.1 depicts different ways of multi-reflection or multi-turn analyzers. Open-path designs avoid overlaps in the flight path leading to a fixed path length for all ions.

Closed-path analyzers have a compact setup and variable flight paths, allowing a theoretically unlimited number of turns. The disadvantage is that multiple mass-to-charge ratio lines overlap in a measured spectrum. Once the electrostatic exit mirror opens, ions with a different number of reflections are detected (see Figure 2.6.2).

The device in this work uses the closed-path approach. Reflecting an ion two times until it reaches its initial point inside the analyzer is hereafter referred to as one *turn*.

The transmitted mass range can be limited to ions reaching the detector with the same number of turns to avoid misidentification in a folded spectrum by use of a mass filter RFQ or the MRS described in Section 2.6.4. Ideally, according to [M. I. Yavor et al. 2015], after N turns, this *unambiguous mass range* is limited to

$$\frac{m/q_{\mathrm{max}}}{m/q_{\mathrm{min}}} = \left(\frac{N}{N-1}\right)^2 \quad . \tag{2.6.2.1}$$

The effective mass range is reduced due to the area inside the extraction mirror seeing pulsed fields while it opens:

$$\frac{m/q_{\mathrm{max}}}{m/q_{\mathrm{min}}} = \left(\frac{N+\lambda_{\mathrm{inj}}}{N+\lambda_{\mathrm{inj}}-(1-\lambda_{\mathrm{mir}})}\right)^2 \tag{2.6.2.2}$$

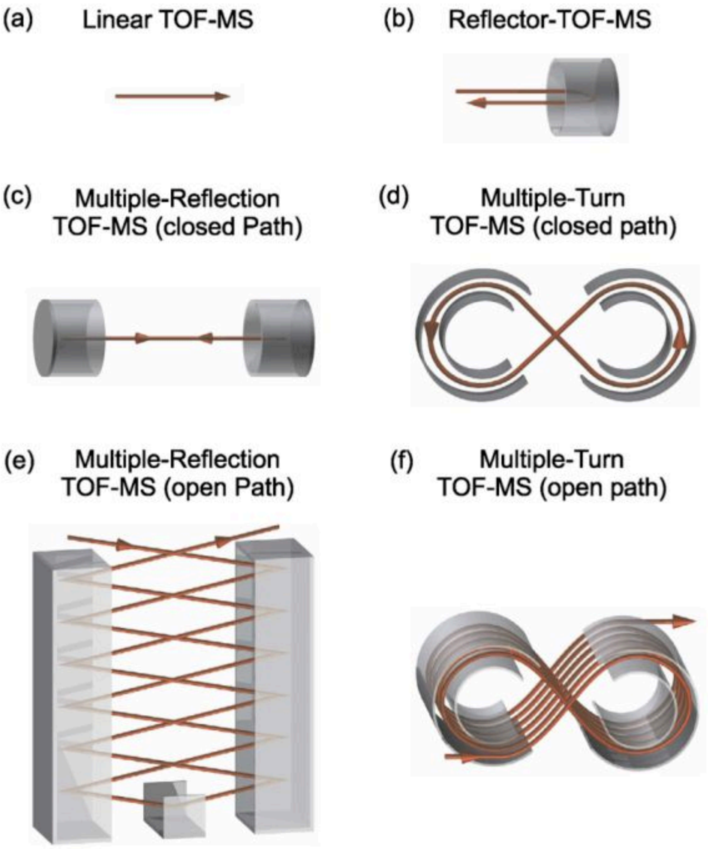

Figure 2.6.1: Different types of analyzers for TOF mass spectrometry. Taken from [Plass, T. Dickel, and Scheidenberger 2013].

$$\lambda_{\text{inj}} = \frac{t_{\text{inj}}}{t_a} \qquad \lambda_{\text{mir}} = \frac{t_{\text{mir}}}{t_a} \tag{2.6.2.3}$$

with t_a the time needed for mass m to fly one turn, q the ion charge, N the number of turns m did fly before, t_{inj} the time the ion needs to reach the reflector the first time, and t_{mir} the time required to pass the reflector region.

Since ions pass the same flight path multiple times, ions detected at a similar TOF can have completed a different number of turns. The changed flight path length s, depending on the turn Number N, can be expressed as

$$s = s_0 + N \cdot s_{\text{turn}} \tag{2.6.2.4}$$

with s_0 the flight path length without reflections and s_{turn} the distance traveled during a turn. Calibration can still be achieved, provided the turn number is known. Equation (2.6.1.2) can then be expressed with the flight path in dependence on the number of turns N

$$\frac{m}{q} = \frac{2eU}{s_0^2 \cdot (1 + N \cdot s_{\text{turn}}/s_0)} = \frac{a \cdot (t - t_0)^2}{(1 + N \cdot b)^2} \tag{2.6.2.5}$$

with $b = \frac{s_{\text{turn}}}{s_0}$ as a calibration parameter in addition to $a = \frac{2eU}{s_0}$ and t_0 [Ayet San Andrés et al. 2019].

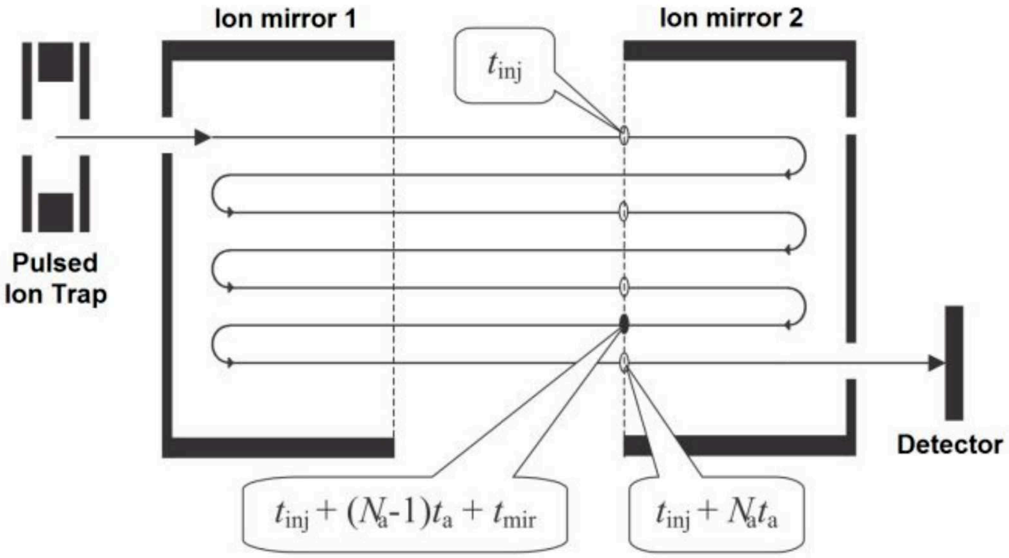

Figure 2.6.2: Flight path projection over time in a closed-path multiple-reflection system. Ions reach mirror 2 with a TOF of t_{inj} travel for several turns N_a, which takes a TOF of t_a each until mirror 2 is opened, and they fly toward the detector. Taken from [M. I. YAVOR et al. 2015].

2.6.3 Time Focus Shift

A closed-loop MR-TOF-MS has a primary time focus formed by the trap extraction field. The analyzer electrodes acting as electrostatic lenses are set to allow stable flight paths inside the analyzer for high turn numbers. The focus can be gradually shifted during each pass to set the time focus again on the detector after the final turn (Figure 2.6.3). However, this method requires adapting the mirror and lens potentials for a given number of turns [WOLF, MARX, et al. 2012].

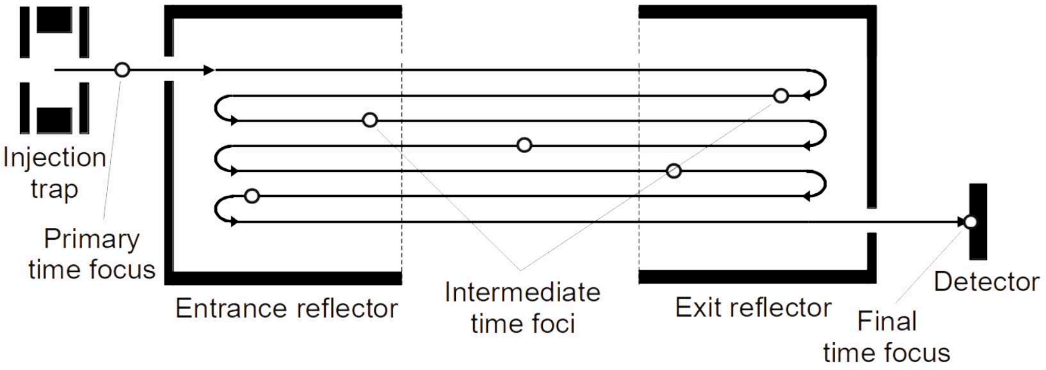

Figure 2.6.3: Typical way of focusing ions inside closed-turn MR-TOF-MS. With constant mirror reflection potentials, the focus is gradually shifted in each turn to settle on the detector finally. Taken from [M. I. YAVOR 2014].

Figure 2.6.4 shows the approach of *time focus shift* (TFS) which is realized in the MR-TOF-MS of this work [T. DICKEL, M. I. YAVOR, et al. 2017]. When ions enter the analyzer, the first half of the electrodes let the ions pass, while the second half is set for the initial TFS. This voltage puts the time focus between the two analyzer mirrors. While the ions of interest are inside this mirror, the first mirror switches to its TFS set of voltages. Ions that fly back and pass the first mirror then have their time focus shifted to the final position at the detector. Afterward, the second and later the first mirror switch to potentials that maintain the focus for each turn at the same position (*Isochronous Turn* IT), which allows stable voltages for a freely selectable amount of turns while the time focus stays on the detector.

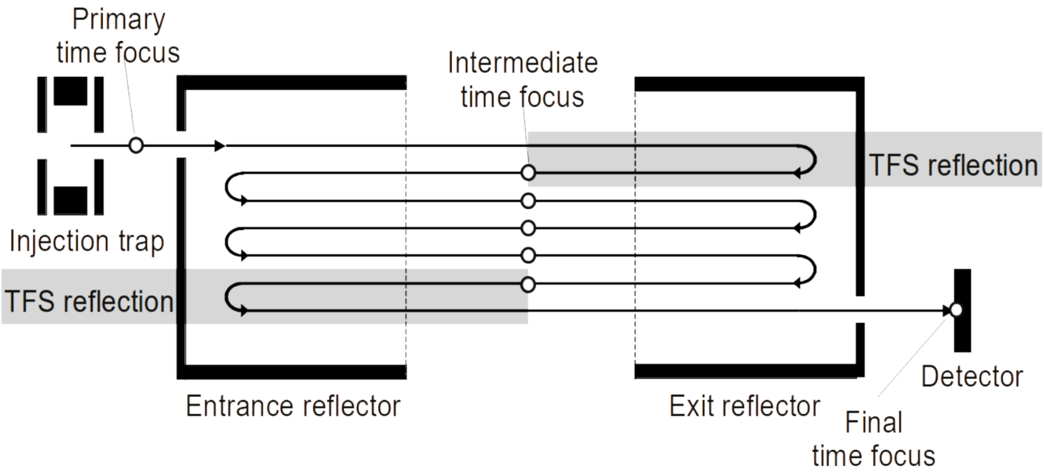

Figure 2.6.4: Using separate voltages for the TFS reflections to set the focus onto the detector. Focus-preserving isochronous turns can occur before, after, or in-between the two TFS reflections. Taken from [M. I. Yavor 2014].

While the previously mentioned method of doing the first TFS reflection at the start of the measurement and the second after the ITs has a superior time focus compared to the other methods, its energy focus also leads to a prominent self-bunching of ion packages due to their space charge as shown in [Lippert 2016].

The self-bunching effect suppresses deviations from isochronous motions of ions in the analyzer and is more dominant for large amounts of ions [Grinfeld et al. 2014]. However, the phase space of two ion species of close masses will start to overlap (peak coalescence), which leads to reduced mass accuracy [Lippert 2016].

Space charge effects pose a separate limitation caused by mutual repulsing ions of the same species. While the effect is negligible at a low amount of ions, it limits the maximum number of ions before affecting MRP [Grinfeld et al. 2014].

This device uses the TFS+IT mode, doing both detector-focusing TFS-reflections before the isochronous turns. In [Lippert 2016], the IT+TFS mode has the best behavior regarding peak coalescence and space charge. However, first-order time-focus corrections can also be applied to both modes.

2.6.4 Mass Range Selector

TOF-MS mass lines can be ambiguous inside a folded spectrum of a closed-path multiple-reflection. Limiting the mass range to the ions fitting inside a single turn helps to avoid misidentification. Since RFQ mass filters have only a low MRP, which is insufficient to isolate the ions that fit into one turn at a high number of turns, the *mass range selector* MRS is used to achieve precise and versatile mass ranges.

It can also compensate for a misaligned beam by steering the flight path toward the analyzer's axis upon the first pass of ions [T. Dickel, Plass, et al. 2015; Toker et al. 2009].

The mass range selector is a segmented ring electrode at the center of the analyzer. A dipole potential applied to opposing electrode segments deflects passing ions. Switching the dipole field precisely between a passing and a deflecting potential allows selecting the mass range by their TOF.

This deflecting potential is applied periodically at a frequency and offset set to let the ions of interest pass while decreasing the transmitted mass range at each turn. To allow a range of ions of different mass centered at m_{pass} to pass, the cutting pulse frequency f_{mrs} is derived from the time m_{pass} requires to fly for one turn inside the MR-TOF-MS analyzer $t_{1T,\text{pass}}$:

$$f_{mrs} = \frac{2}{t_{1\text{T,pass}}} \tag{2.6.4.1}$$

Passing also requires the correct phase, so the center between cutting pulses happens at t_{pass} when m_{pass} is at the MRS center. Applying a shorter periodical deflection pulse increases the mass range precision and is thus preferred to a single deflection at the measurement's start. While only the last applied deflection creates the final mass range, preceding deflections guarantee mass ambiguity. Otherwise, ions of masses outside the desired mass range but within the analyzer area unaffected by the deflection pulse would pass the MRS.

Two separate mass ranges can be transmitted by interconnecting their corresponding parameter set for $m_{\text{pass},1}$ with a second set for $m_{\text{pass},2}$. Gating the required deflection pulses of both sets on each other allows both mass ranges to be transmitted. However, since the lower duration of applying deflection pulses of the two sets dominates, the degree of freedom within each set is reduced by one. With $\Delta m_{pass} = m_{\text{pass,max}} - m_{\text{pass,min}}$, they can be scaled linearly by

$$\lambda_{\text{pass},1} = \lambda_{\text{pass},2} * \left(2 - \frac{\Delta m_{\text{pass},2}}{\Delta m_{\text{pass},1}} \cdot \frac{m_{\text{pass},1}}{m_{\text{pass},2}}\right) . \tag{2.6.4.2}$$

2.6.5 Mass Selective Re-Trapping

When using *mass selective re-trapping*, the analyzer entrance mirror is opened instead of the exit mirror toward the detector. When the ions of interest reach the trap center, their potential is switched from ejection to a re-trapping potential. The trap not only cuts off ions that are too fast (light) or too slow (heavy) to reach the trap in time but also changes the kinetic energy of ions off-center within the trap, as shown in Figure 2.6.5.

The re-trapping separation power can be expressed using the analyzer MRP Equation (2.6.1.6) by the following expression [Timo Dickel et al. 2017]:

$$R = \frac{m}{\delta m} = \frac{t}{2\Delta t + \frac{2}{E_r}\sqrt{\frac{2mU_r}{q}}} \tag{2.6.5.1}$$

With E_r the retarding electric field and U_r the re-trapping potential of the trap. Re-trapping allows for high separation powers, as shown in [Lippert 2016], where values of up to 70 000 are achieved.

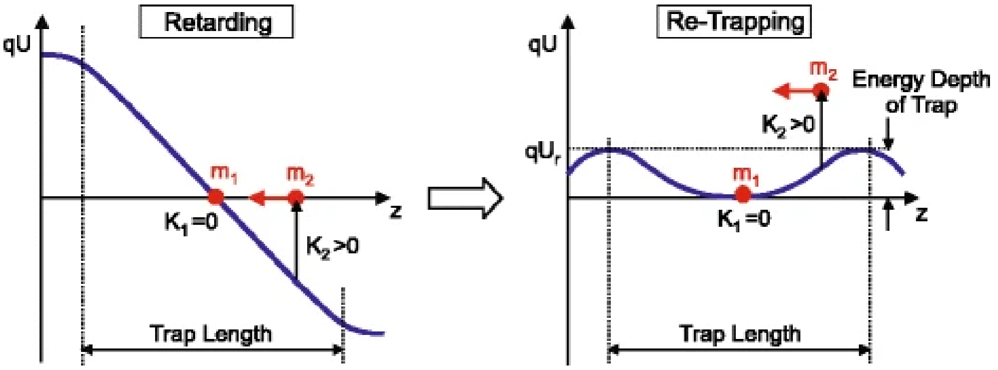

Figure 2.6.5: Left: Ions arrive at trap still at ejection potential. The ion of interest m_1 is at the center of the trap. Right: Trap is switched to re-trapping potential. m_2 is within trap limits but gains kinetic energy and is rejected. Taken from [Timo Dickel et al. 2017].

2.7 Detector and Digitizer

2.7.1 MagneTOF Detector

The detector used in this device is a *MagneTOF DM167* from ETP. A picture of the device and a view of its operation principle are shown in Figure 2.7.1 (from datasheet [ETP electron multipliers 2013]). It is based on isochronous interdynode electron transfer described in [Stresau et al. 2006]. After ions pass the entrance grids and impact onto a 3 mm thick, coated, and flattened stainless steel plate, a magnetic field focuses the emitted electrons in time-of-flight to the next dynode.

Compared to *micro channel plates* (MCP), the MagneTOF™ allows an average detection pulse width of 400 ps, a linear dynamic range even during and after bursts of up to 300 000 ions, and detection efficiency of up to 80 % (low mass) [ETP electron multipliers 2013].

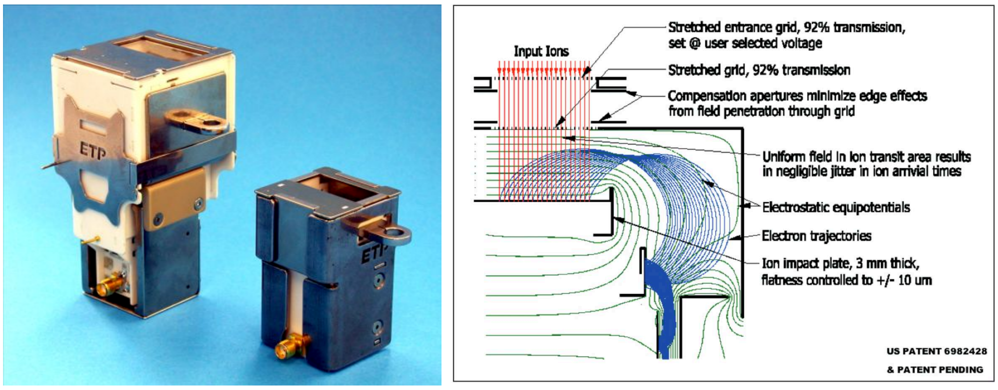

Figure 2.7.1: Left: Picture of MagneTOF™detector range: DM291 (left), DM167 (right); Right: Electron optics inside the DM167. Taken from published datasheet [ETP electron multipliers 2013].

2.7.2 Digitizers

The detector signal needs to be converted into digital form for further analysis. The MR-TOF-MS of this work utilizes two different digitizers by splitting the detector signal to preserve dynamic range and resolution. The digitizers are then operated from the same computer by two instances of the same analysis software.

Analog-to-Digital Converter

The *analog-to-digital converter* (ADC) scans the input signal and quantizes its amplitude into channels at a fixed sample rate (see Figure 2.7.2(a)). The ADC preserves the original signal form, allowing the detection of ions impacting simultaneously or baseline investigations. A disadvantage is the required sampling rate for high resolution (1 ns requires 1 GHz), transmitting and analyzing the large quantity of data, and low signal rates disappearing in baseline noise.

In this work, the Signal Recovery ADQ412 is used at a sampling rate of 3.6 GHz, 12-bit vertical resolution (0.2 mV), and 2 GHz analog bandwidth.

Time-to-Digital Converter

The *time-to-digital converter* (TDC) detects when the input signal crosses a certain threshold. The transferred list of timestamps corresponds to the difference between a given start trigger and the detected signals (see Figure 2.7.2(b)).

Using a threshold minimizes baseline and noise influence while reducing the amount of data to process. Instead of the signal shape information, just the peak position is transmitted. The result is a clean spectrum and high detection efficiency down to single ions. Furthermore, extended analyzing methods can be applied thanks to storing time-of-flight information for each event, even in accumulated spectra. However, since processing the signal takes time, most TDCs have a non-extending dead time in which they are deaf to new events. In addition, the input signal does not fall below the threshold at high rates, which causes an extending dead time effect, making TDCs unsuitable for high signal rates.

The TDCs used in this work are the MCS6A and MCS8 from Fast ComTec.

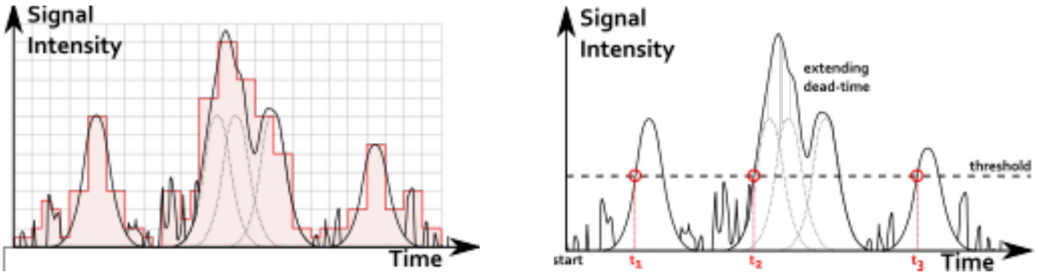

(a) ADC concept with a fixed sample rate and vertical resolution. The result is a table of quantized time against quantized voltage.

(b) TDC concept with a signal threshold and leading-edge trigger. The result is a list of timestamps relative to the start pulse.

Figure 2.7.2: Digitizing ADC/TDC concepts in comparison. The input signal is in black, digitized result is in red.

2.8 Kendrick Mass Defect Analysis

Molecule fragmentation-based spectra can be densely populated and thus appear convoluted depending on the precursor molecule and fragmentation degree. However, the separation of multiples of small molecules K from the precursor molecule leads to a series of equidistant mass lines corresponding to different fragment ions. Plotting their mass excess against the mass value will thus put all molecules of a chain into a slanted line. Their fragmentation chains and building blocks can be estimated by comparing the mass excess between fragment molecules.

Kendrick mass defect (KMD) analysis optimizes this visualization by scaling mass value and excess to shift molecules of a specific fragmentation chain of multiples of the molecule K into a horizontal line [Kendrick 1963]. Scaling is realized by calculating the *Kendrick mass* KM by

$$KM = m \cdot \frac{\lfloor m_K \rfloor}{m_K} \quad , \tag{2.8.1}$$

where m is the measured mass, m_K the real mass of K, and $\lfloor m_K \rfloor$ its nominal mass. By plotting the Kendrick mass against the Kendrick mass defect

$$KMD = \lfloor m \rfloor - KM \quad , \tag{2.8.2}$$

the slant of molecules missing multiples of K becomes horizontal. The slant K_a is calculated for the two Kendrick masses m_1 and m_2 with

$$\begin{aligned} a &= \frac{KMD_2 - KMD_1}{KM_2 - KM_1} && (2.8.3)\\ &= \frac{\lfloor m_2 \rfloor - m_2 * \lfloor m_K \rfloor / m_K - \lfloor m_1 \rfloor + m_1 * \lfloor m_K \rfloor / m_K}{m_2 * \lfloor m_K \rfloor / m_K - m_1 * \lfloor m_K \rfloor / m_K} && (2.8.4)\\ &= \frac{\lfloor m_2 \rfloor - \lfloor m_1 \rfloor}{(m_2 - m_1) * \lfloor m_K \rfloor / m_K} - 1 \quad , && (2.8.5) \end{aligned}$$

which becomes zero in case $m_K \cdot k = m_2 - m_1$ and $\lfloor m_K \rfloor \cdot k = \lfloor m_2 \rfloor - \lfloor m_1 \rfloor$ where $k \in \mathbb{N}$.

Plot points with a similar KMD form horizontal lines and belong to the same molecule but are missing a varying multiple of the reference mass. Slanted lines indicate repeated separation of a different reference mass.

A typical application uses the reference mass $K = \mathrm{CH_2}$ with

$$\lfloor m_K \rfloor / m_K = 14/14.01565 \quad . \tag{2.8.6}$$

Figure 2.8.1 shows a KMD analysis of fragments of $\mathrm{C_{23}H_{32}N^+}$, which is acquired in this work in Section 6.2.5. The point size indicates the detected ion rate for each fragment. The plot points of higher intensity form multiple horizontal lines where a molecule lost multiples of $\mathrm{CH_2}$. In addition, almost vertical lines corresponding to the loss of H-atoms are shown.

2.9 Double Bond Equivalent Analysis

The double bond equivalent (DBE), or the degree of unsaturation, measures the number of double bonds and ring systems in organic molecules. Hence, it also represents the number of hydrogen pairs in a molecule required to saturate the structure. This number changes with the number of carbon rings and molecule bonds and can thus be used for fragmentation path analysis.

The DBE can be calculated with the number of atoms of an element n_i and their valence v_i by

$$\mathrm{DBE} = 1 + \tfrac{1}{2} \sum n_i (v_i - 2) \quad , \tag{2.9.1}$$

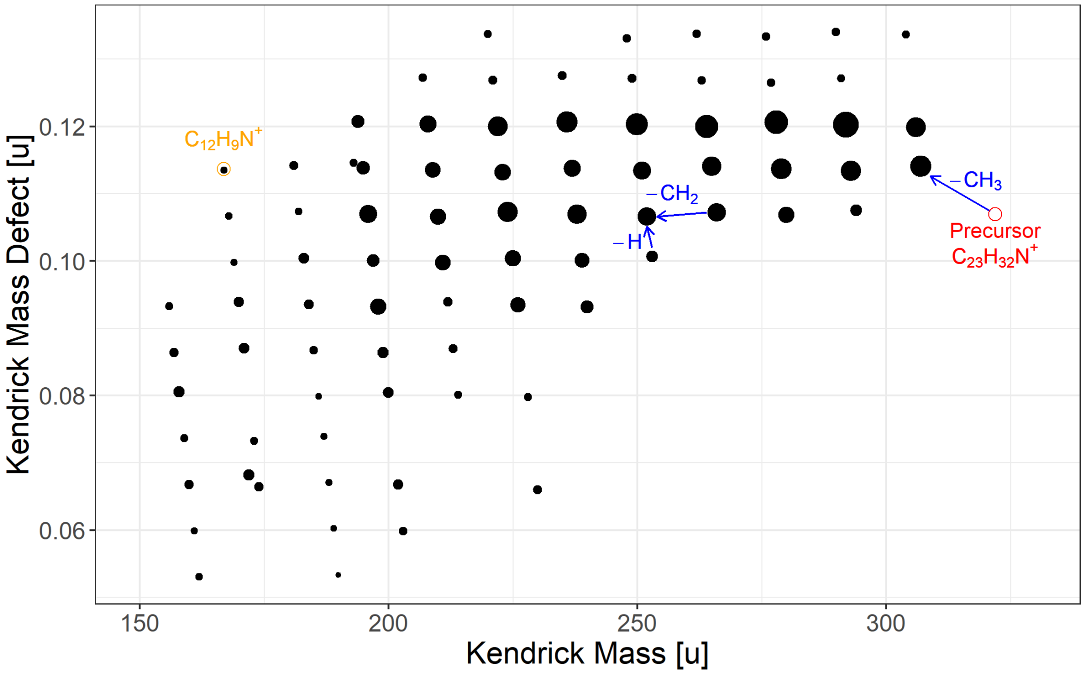

Figure 2.8.1: Kendrick Mass Defect Plot for the Fragmentation of $C_{23}H_{32}N^+$.

which is often simplified to

$$DBE = 1 + C + \frac{N}{2} - \frac{H}{2} - \frac{X}{2} \quad , \tag{2.9.2}$$

where C, N, H, and X are the number of carbon, nitrogen, hydrogen, and halogen atoms inside the molecule, respectively. Other elements are added according to their valence electrons. Divalent elements like oxygen are disregarded since they don't change the molecule's saturation [Badertscher et al. 2001].

A common approach for analyzing fragmentation patterns of complex samples is plotting the DBE value of all produced fragments against the amount of contained carbon atoms. The size of each fragment's point typically represents the abundance. Since certain molecule classes naturally assume specific DBE values and fragmentation processes cause specific DBE changes, information on molecular structures can be gained by analyzing the distribution of DBE values [Marshall et al. 2008].

2.10 Fragmentation Processes

A major goal of tandem mass spectrometry is the structural analysis of the examined precursor molecule. However, once the precursor molecule is isolated, fragmented, and its fragments measured and identified, the reconstruction of the precursor molecules's structure is only possible by understanding fragmentation processes. To this end, the formed fragments are compared to a theoretical set of ions produced by applying known fragmentation processes to the precursor molecule.

The first step in understanding fragmentation processes is locating the charge-carrying atom inside a molecule. Ionization by losing an electron happens at the electron with the lowest ionization energy. With decreasing preference, this happens for non-bonding electrons, π-electrons, and σ-electrons. π-electrons are inside π-bonds, which have two areas of overlap in their atomic orbitals and which can not rotate without breaking. σ-electrons are inside σ-bonds, the strongest type of covalent bond due to their direct overlap of atomic orbitals [Dass 2007].

As depicted in Figure 2.10.1, most fragmentation processes can be divided into bond-cleavage and rearrangement reactions. The prevalent fragmentation processes are simple bond-cleavage reactions, where a bond between atoms is broken without new connections between the constituents. Reactions, where both product molecules retain their binding electron, are called *homolytic*. If one molecule keeps both binding electrons, the reaction is called *heterolytic*.

Cleavage reaction can be divided into σ and α cleavages. σ-cleavage refers to the severance of a σ-bond, while α-cleavage describes the severance of a C-C bond adjacent to the carbon bearing a functional group. A special case is a benzylic cleavage where a hydrogen atom is severed from an alkylic adduct in a carbon ring. A tropylium cation is then likely produced, which is a regular heptagonal, planar, and cyclic carbon ring $C_7H_7{}^+$. The most prominent rearrangement reaction is the McLafferty rearrangement: A hydrogen atom at a Y-shaped branch is rearranged, which moves a bond to compensate for radicals after the severance [Dass 2007].

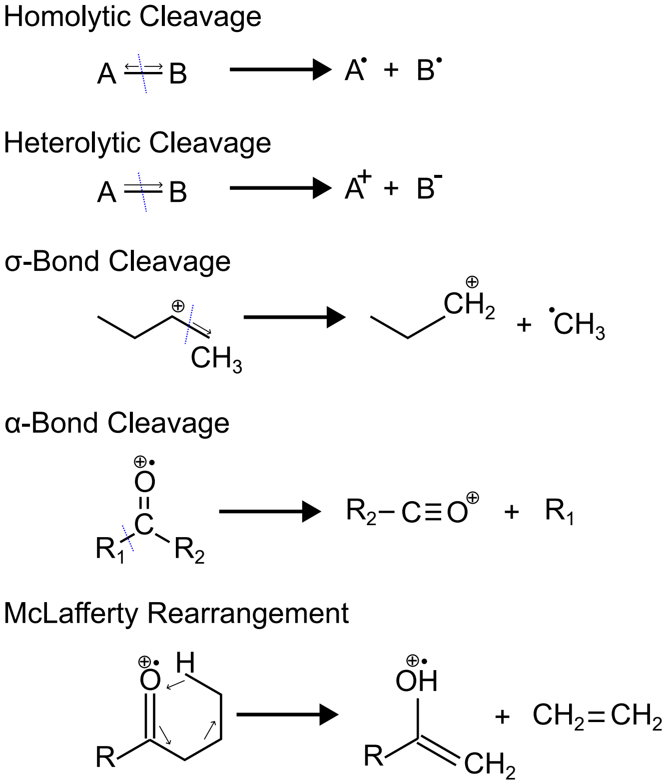

Figure 2.10.1: schematics and examples of common fragmentation processes.

3 Experimental Setup

3.1 Overview

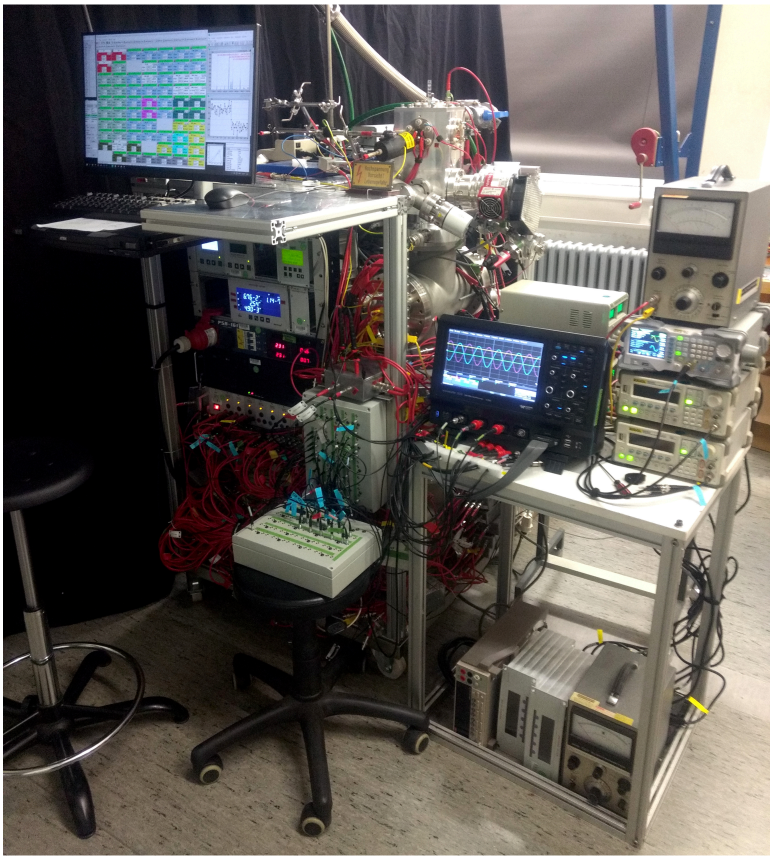

Figure 3.1.1: Photograph of the setup. The front features the user peripherals, pressure gauge displays, the trigger system, and crate power supplies. The micro-ESI source and digitizers are placed on the top of the rack. The right side contains the vacuum chambers and turbomolecular pumps. The RF voltage generation and high voltage switches are positioned at the backside.

The system (Figure 3.1.1) is based on a design with the primary objective of constructing an MR-TOF-MS, which is mobile but still capable of providing very high mass resolving power. Figure 3.1.2 shows the main components of each vacuum section and its operating pressure. The robust and compact design allows transportation for in-situ measurements. The three DN150 CF crosses, including pumps and electronics, fit into a volume of $0.8\,\mathrm{m}^3$ and operate at $1.5\,\mathrm{kW}$ from a single three-phase power supply.

Its original design is based on the MR-TOF-MS developed in [T. Dickel 2010], commissioned in [Lang 2016], and further improved in [Lippert 2016]. While the data presented in these works is already impressive, this work further improves the design, reliability, and usability of the device and its software system. A significant point in design improvements concerns the reliable production and insertion of ions into the system.

Following the ion's path through the system, they first enter the *atmospheric pressure interface* (API), which directs them to the *beam preparation system* RFQs, where they are filtered and cooled before they reach the RFQ trap. This trap collects the ions before it injects them in bunches into the TOF analyzer with set kinetic energy. In the analyzer, they separate due to different velocities. After the analyzer is opened, they impact onto the detector, which digitizers convert into data for the data acquisition software.

The ions are produced at atmospheric pressure and enter the API at 1 - 10 mbar, depending on open inlets, through inlet capillaries. The API's carpet transports them through its 1 mm exit nozzle to the transmission control RFQ vacuum chamber at $1 \cdot 10^{-4}$ mbar. They are then filtered by the mass filter RFQ at $1 \cdot 10^{-5}$ mbar before entering the cooler RFQ chamber. There they are cooled using nitrogen buffer gas at $1 \cdot 10^{-3}$ mbar while they are led toward the trap RFQ. After trap ejection, ions enter the analyzer chamber, where they travel path lengths of up to 1 km at $1 \cdot 10^{-7}$ mbar.

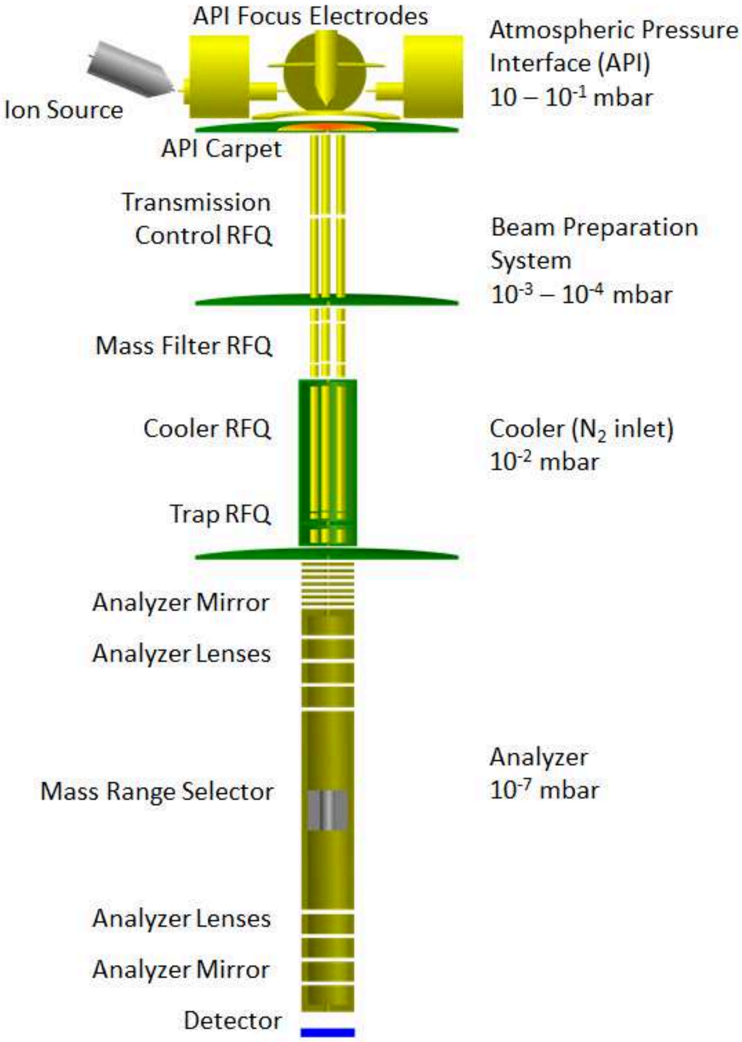

Figure 3.1.2: Schematic layout of the MR-TOF-MS. Essential components are labeled. The three stages API, beam preparation system (including cooling RFQ) are listed with their operating pressure regime.

3.2 Ion Sources

The API features five mounting positions for DN63 flanges to mount independent ion sources allowing higher compatibility and, thus, application versatility. Furthermore, this modular setup allows for better maintenance and adjustability. All modules ensure a rejecting electric potential similar to the other modules and moderate leak tightness.

The module-like designed jet disruptor occupies the top mounting position, while the other positions are occupied by a blind flange, two heatable inlet capillaries, and a thermal ^{133}Cs-source.

Ion sources operating at atmospheric pressures can be set in front of the heatable inlet capillaries to inject ions into the API chamber. This allows for high compatibility with self-build and commercial ion sources that can be exchanged or refilled while the system is running. Two self-build ion sources used in this work are the nano-ESI offline ion source and the micro-ESI online ion source. Typical parameters used to operate the ion sources for the analytes that were investigated in this work are shown in Table 3.1.

Source Type	Analyte	Parameter	Value
Nano-ESI	crude oil sample 250 ppm in 1:1 MeOH + toluene	Emitter tip Ionization potential Inlet temperature	4 µm 1300 V 200 °C
	Agilent tuning mix G1969-85000	Emitter tip Ionization potential Inlet temperature	1 µm 1600 V 120 °C
	Caffeine $1 \cdot 10^{-5}$ mole/l in 1:1 H_2O + MeOH	Emitter tip Ionization potential Inlet temperature	1 µm 1600 V 120 °C
Micro-ESI	crude oil sample 250 ppm in 1:1 MeOH + toluene	Flow rate Ionization potential Inlet temperature	0.10 ml/h 2800 V 200 °C
	Agilent tuning mix G1969-85000	Flow rate Ionization potential Inlet temperature	0.05 ml/h 2800 V 120 °C
	Caffeine $1 \cdot 10^{-5}$ mole/l in 1:1 H_2O + MeOH	Flow rate Ionization potential Inlet temperature	0.05 ml/h 2800 V 120 °C
Thermal	Caesium	Power	4.5 W

Table 3.1: Typical Ion Source properties for the analytes used in this work. The medium-heavy crude oil sample was provided by the workgroup of Prof. Dr. W. Schrader at the MPI für Kohleforschung in Mülheim an der Ruhr.

3.2.1 Heatable Inlet Capillaries

The heatable inlet capillaries (Figure 3.2.1) allow any atmospheric ion source to be coupled to the API. The actual inlet capillary is commercially available as *Thermo Velos Ion Transfer Tubes* to simplify maintenance and repair. It is screwed into a copper block that also houses four 20 W heating cartridges and a temperature sensor coupled with a PID controller. With the capillary inner diameter of 0.58 mm and possible heating

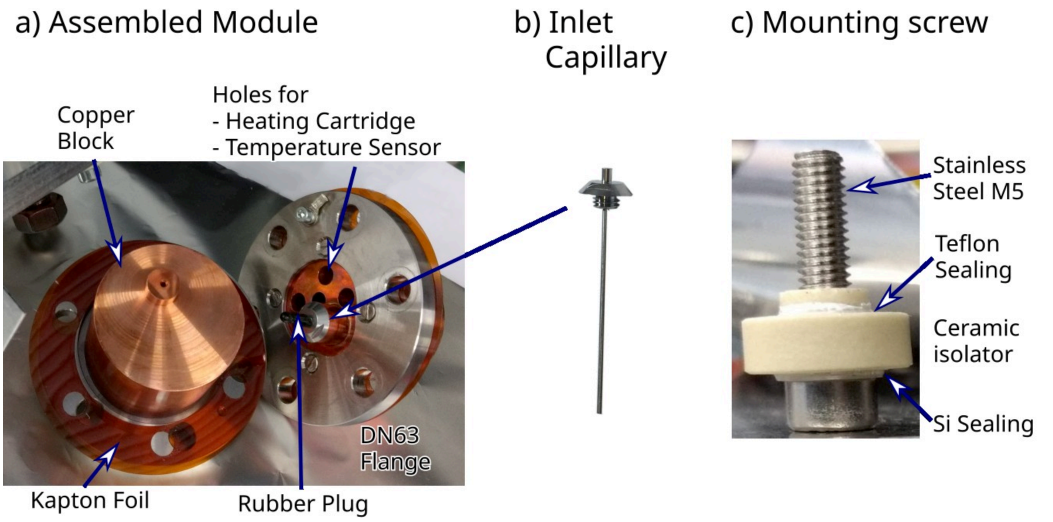

Figure 3.2.1: Heatable inlet module for the API.
a) Assembled front and back side.
b) Ion transfer tubes (Thermo Fisher Scientific, Velos Ion transfer Tube, 0.58 ID).
c) Mounting screw with centering and isolation.

of up to 250 °C along its whole length, this setup is highly resistant to clogging and contamination.

Since the API requires an electric field to repel ions from the inlets, the aluminum frame holding the copper block is connected to a power supply. A Kapton foil and ceramic screw spacers ensure electrical isolation toward the chamber. Due to the spacers, the chamber requires additional leakage sealing for the screws (silicon) and spacers (Teflon) to maintain its vacuum. In operation, each open inlet increases the pressure in the chamber by 2.5 mbar.

3.2.2 Nano-ESI Offline Ion Source

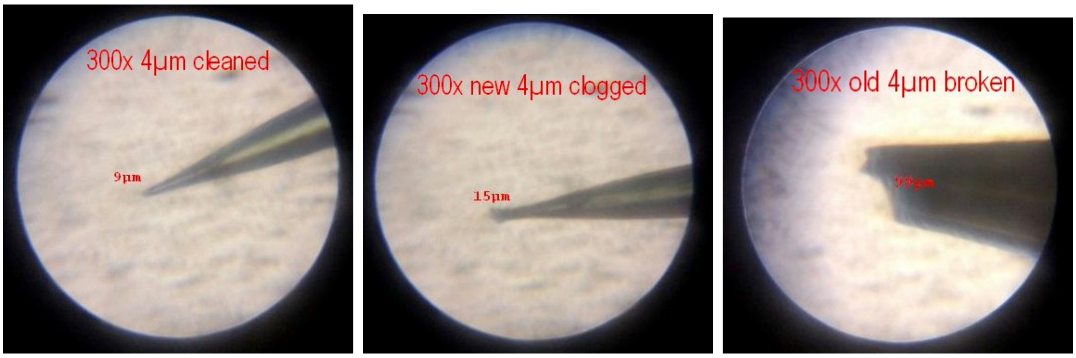

(a) After cleaning **(b)** Clogged tip **(c)** Broken tip

Figure 3.2.2: Nano-ESI emitters with 4 µm tip in various states magnified 300 times using a compound microscope.

A metal-coated hollow glass needle realizes nano-ESI with an outer diameter of 1.2 mm and an inner diameter of 0.94 mm, ending in a tip of 4 µm diameter (GlassTip$^{\text{TM}}$ BG12-94-4 by New Objective, Littleton, USA). As an offline emitter, the needle's volume serves as its reservoir, being emptied by capillary force without a pump. Once empty, it needs to be refilled by hand using a syringe.

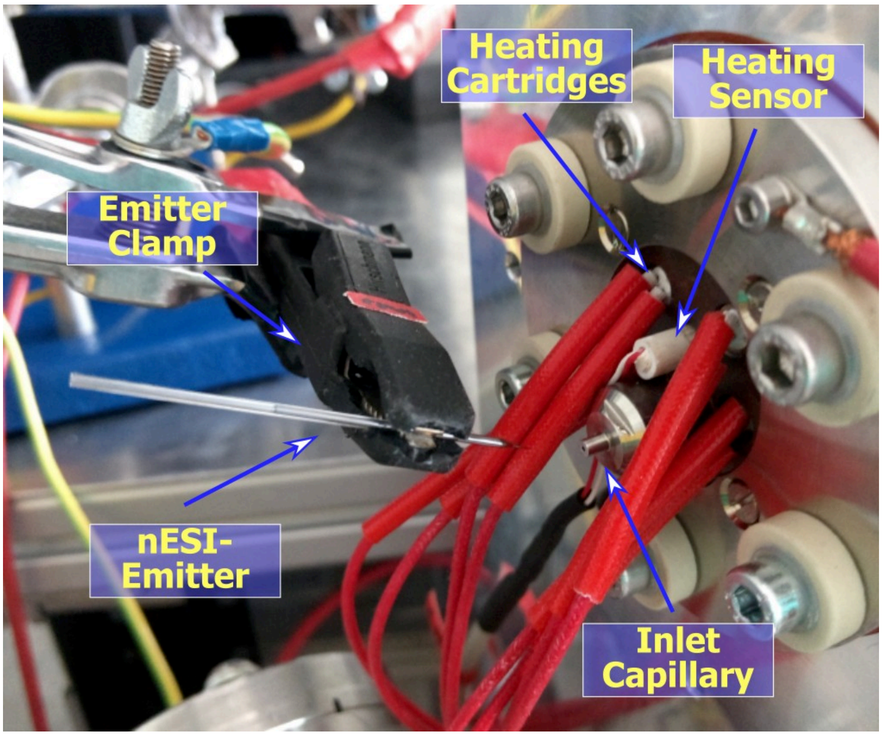

Figure 3.2.3: Setup of nano-ESI source. The black clamp electrically contacts the glass emitter needle, whose tip is metal-coated. The resulting spray is directed toward the heated API inlet capillary.

Figure 3.2.3 shows the emitter inside an aluminum cushion held by a clamp, which applies 1200 - 1900 V to produce the Taylor cone described in Section 2.4.1. The tip is positioned 3 - 8 mm toward the heatable inlet capillary described in Section 3.2.1. A 10 nl/min flow rate produces a total ion current of about 10 nA.

While the setup design is simple, it comes with a few drawbacks. Filling the fragile glass needles can be difficult, and repeated use easily damages the delicate tips. While they can be used repeatedly as long as the coating lasts, they require careful cleaning and easily clog depending on the analyte. Their fine tip is also highly sensitive to its positioning toward the inlet capillary and ambient gas flow, leading to inconsistent ion rates. Figure 3.2.2 shows the 4 µm wide emitter tip in a cleaned, clogged, and broken state magnified 300 times using a compound microscope.

3.2.3 Micro-ESI Online Ion Source

A new ion source was designed to counter the shortcomings of the nano-ESI emitter. Figure 3.2.4 shows a graph of the assembled system of the newly designed micro-ESI online source. Core parts of the design are shown in Figure 3.2.5. They include a motor-driven syringe, which is connected to a thin, blunt metal needle of 0.16 mm diameter. The needle is set into a larger needle of 0.4 mm diameter for electrical contact. PEEK tubing, unions, and ferules acting as sealing connect the needle to the syringe. The holding structure is based on a custom design and was 3D-printed using PLA plastic (polylactide). An operation with a flow rate of 0.1 - 0.5 µl/min and emitter voltage of 2 - 3 kV depending on the analyte produces a total ion current of 200 nA.

The system has a small dead volume below 100 µl, is easy to clean, and has only a low chance of clogging, which has been tested with a crude oil residue sample with

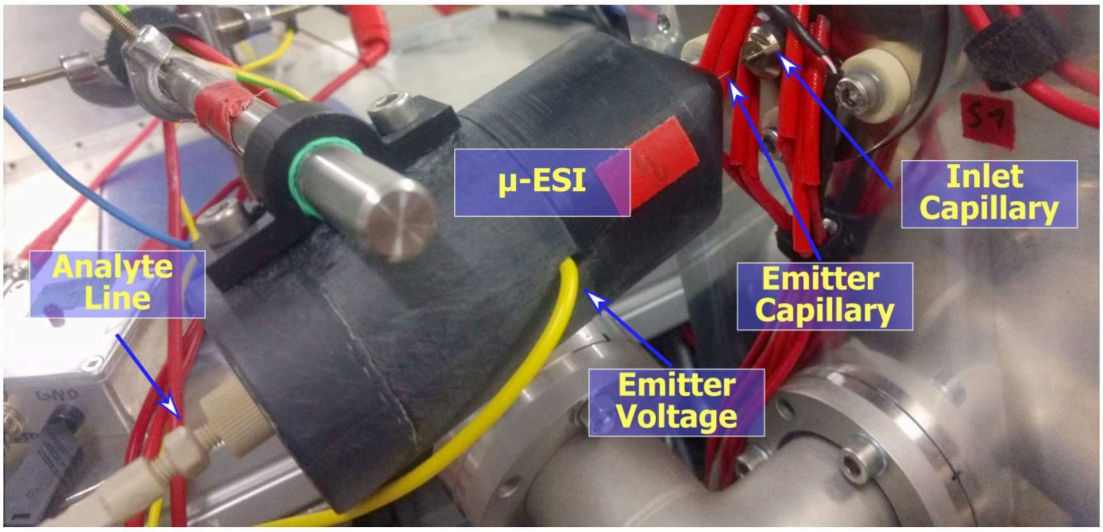

Figure 3.2.4: Photograph of the self-designed micro-ESI online ion source.

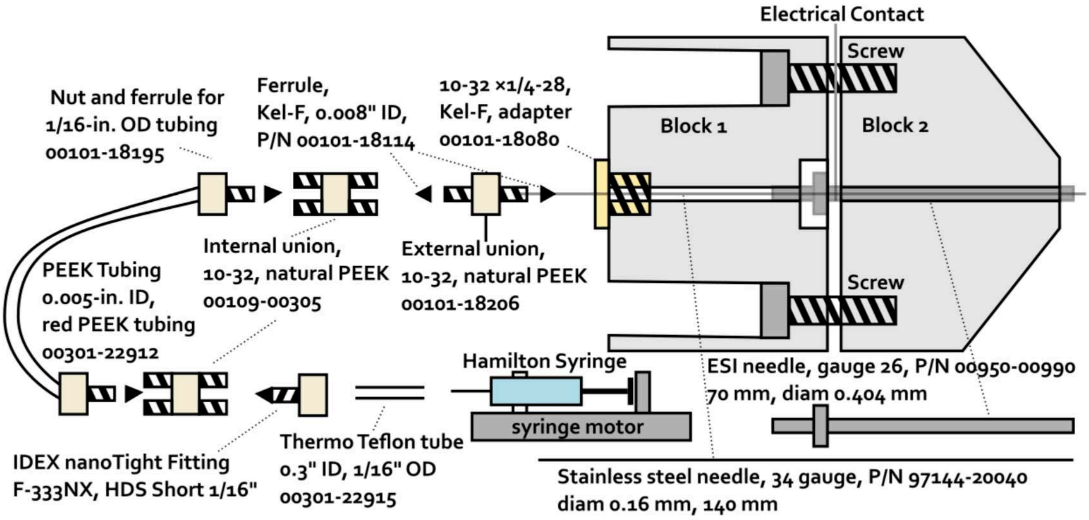

Figure 3.2.5: Parts and composition of the newly designed micro-ESI online source. Part pictograms are not true to scale. Product numbers for products of Thermo Fisher Scientific, Waltham, USA.

a concentration of 250 ppm for months of daily use. It is more forgiving regarding its alignment to the inlet capillary and produces a consistent ion rate. Furthermore, compared to the glass capillaries of the nano-ESI emitters, the stainless steel needle enables electrochemical reaction of the analyte, providing a wider field of applications, for example, investigating fullerenes.

The following experimental data in the thesis is obtained using this ion source. All measurements also used the same syringe and PEEK tubing, which were flushed with toluene and methanol when switching analytes.

3.2.4 Thermal Cs Ion Source

A thermal ion source shown in Figure 3.2.6 was designed and built to provide a steady, contaminant-free current of ^{133}Cs ions for diagnostics and optimization.

A heating filament (Model 101139, HeatWave Labs, Watsonville, USA) is heated by a current of 1.45 A and consumes a power of 3.6 W. Generated ions are accelerated by a 30 V potential drop toward a 5 mm nozzle leading to the carpet chamber. To prevent oxidization, the source is primarily operated at 1 mbar with the other inlets closed.

Figure 3.2.7 shows the ion production during the initial heating period. Surface contaminating ions are ionized first until, after about one hour of heating, ^{133}Cs ions dominate the spectrum. After 1 hour, the source emits a stable ion current of 10 nA. The ^{133}Cs ions can be used for calibration and diagnostics.

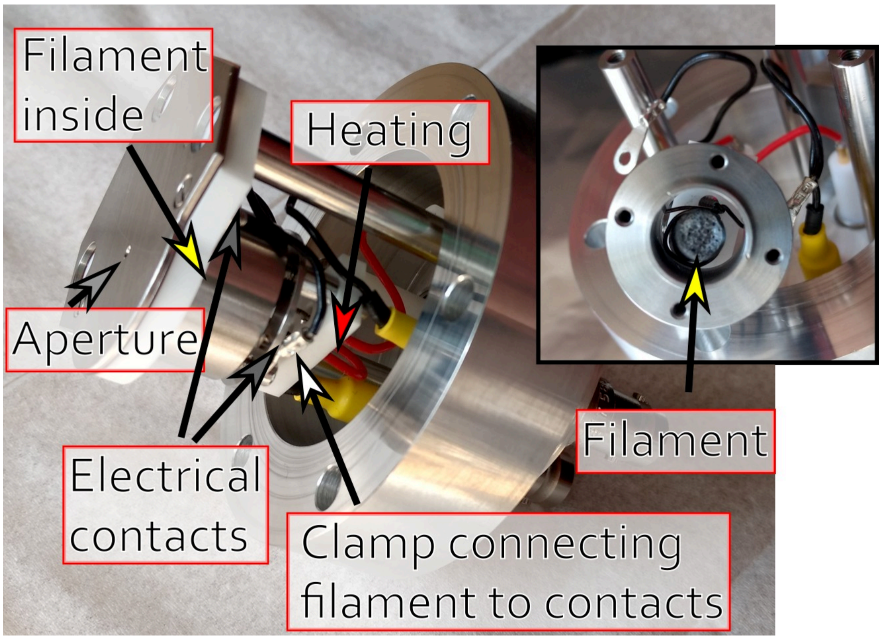

Figure 3.2.6: Photograph of the ^{133}Cs ion source API module. The filament from HeatWave Labs, (Watsonville, USA), is connected to the feedthroughs by clamps in a Makor block. Its surrounding steel cylinder is set to a higher potential as the aperture plate accelerates ions toward and through the nozzle.

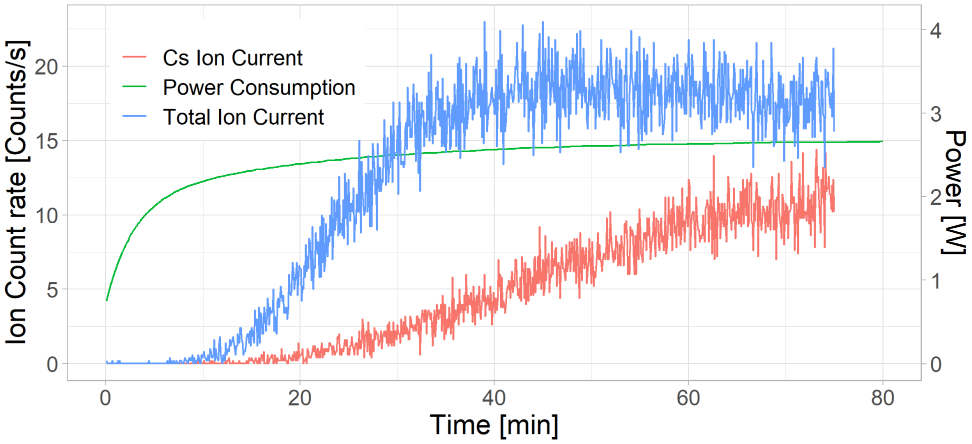

Figure 3.2.7: Rate of ions produced by the thermal ^{133}Cs ion source and detected by the MR-TOF-MS within the first 75 minutes after starting heating the source. Shown are the total ion rate (blue), the rate of ^{133}Cs ions (red), and the heating correlated power consumption (green).

3.3 Atmospheric Pressure Interface

The *atmospheric pressure interface* collects ions from different sources at atmospheric pressure and feeds them into the following beam preparation system RFQs.

Compared to the old design used in [Lippert 2016; Lang 2016] consisting of a single heatable inlet capillary and a skimmer, the new design has improved transmission, and cleaning access and is less prone to clogging. In addition, the new design allows the parallel use of various ion source systems in independent configurations.

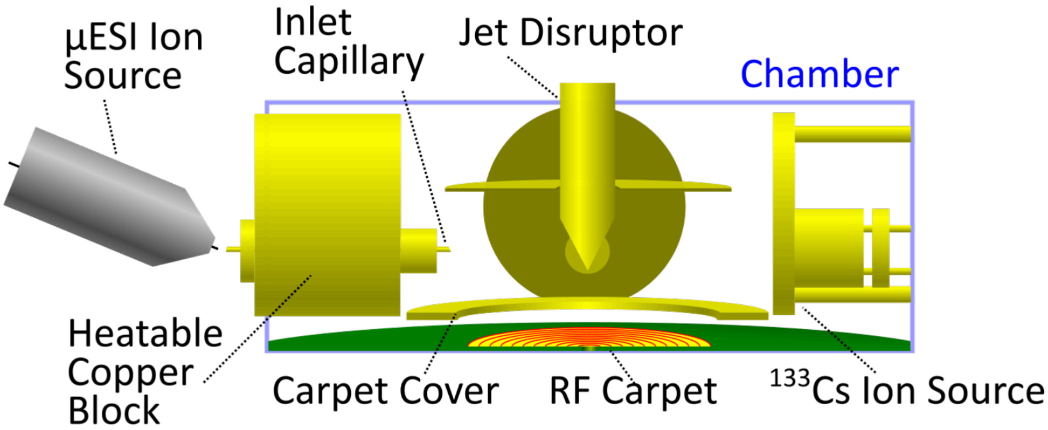

Figure 3.3.1: Schematic figure of the API.

3.3.1 Design

The new design as depicted in Figure 3.3.1 consists of modules transporting or producing ions into a low-vacuum chamber, where the ion jet is dispersed. An RF carpet collects the resulting ion cloud and transports it toward the beam preparation system.

The API frame features five module mounting positions for DN63 flanges (Figure 3.3.2). Currently, four modules are mounted: a ^{133}Cs in-vacuum source, two heatable inlet capillaries for atmospheric ion sources like ESI, and the jet disruptor. Ions produced inside or outside the chamber from different sources are mixed mid-air inside the chamber at 3 mbar.

Inside the chamber, the orthogonal injection and the *jet disruptor* deflects neutral particles inside the collimated gas jet while the disruptor disperses ions into a cloud (Figure 3.3.3). A static electric field pushes the cloud from a *pushing plate* electrode at the top toward the RF carpet at the bottom of the chamber. A *carpet cover* electrode protects the electric components of the RF carpet and directs ions toward its center. The chamber allows a high rate of ions above 10 nA ($\sim 6 \cdot 10^{10}$ particles/s) with a transport efficiency of 77 %.

An RF carpet, as described in Section 2.5.4, then uniformly transports the ion cloud toward the exit nozzle. The RF carpet is an PCB board with 50 concentric ring electrodes. An RF signal is applied to each ring with a 180° phase shift between neighboring electrodes, creating a pseudopotenial. This pseudopotential keeps the ion floating 1 mm above the RF carpet's surface while a DC-gradient directs them to its nozzle at the center. The exit nozzle has a slightly repulsing potential to steepen the angle at which ions pass through the nozzle and to increase transport efficiency toward the following beam preparation system.

The design offers high resistance against clogging using modular heatable inlet capillaries that can be adapted to the analyte consistency. Furthermore, the jet disruptor prevents most neutral particles from impacting on the carpet. Due to its low-mass cutoff, the carpet loses most of the light molecules along its surface. Thanks to the modular design and usage of mostly flat and easily accessible surfaces, the system can be cleaned quickly and efficiently.

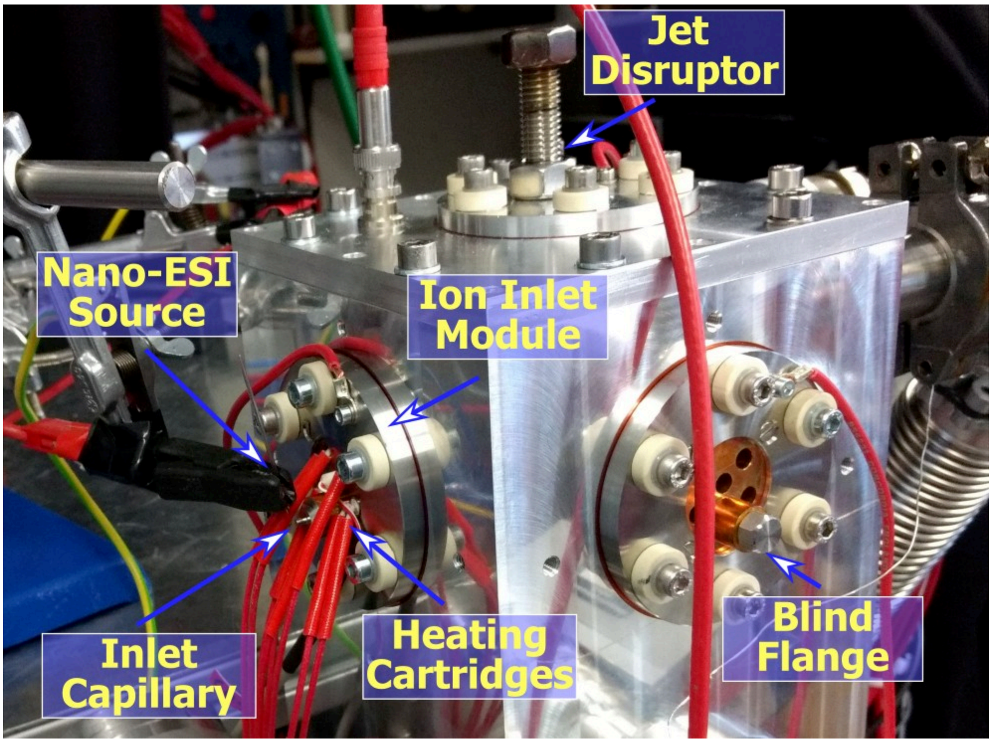

Figure 3.3.2: Photograph of the new API built and in use. A heated ion inlet module with a nano-ESI source can be seen on the left. The adjustable jet disruptor protrudes from its mounting module at the top.

3.3.2 Ion Optical Simulations

Since the new API is a newly designed ion optical system, simulations were performed to determine the ion's flight paths, the dependence on ion mobility, and the optimal electric potentials to guarantee a high, mass-independent transport efficiency.

A virtual API setup shown in Figure 3.3.1 is created to simulate ion interaction with the electric fields of the API electrodes and the RF carpet using the ion trajectory simulation program ITSIM [Plass 2001]. The determined values are then used as starting value for experimental optimization of the voltages.

An example of a simulated ion trajectory is shown in Figure 3.3.4. Once the ions leave the gas flow dominated areas, electrical fields dominate the ion movement and the system behaves according to the theory described in Section 3.3.1. The potential pushing ions toward the RF carpet allows variations of 30 V without decreasing transport efficiency drastically. The carpet transports all ions within 100 - 620 u toward its nozzle, regardless of where they enter its 50 cm^2 active surface.

The RF carpet transport has been simulated separately to determine the dependence of the transport efficiency on RF amplitude and frequency. The pushing electrical field onto the RF carpet of 20 V/cm and a DC drag field of 4 V/cm toward its center are kept

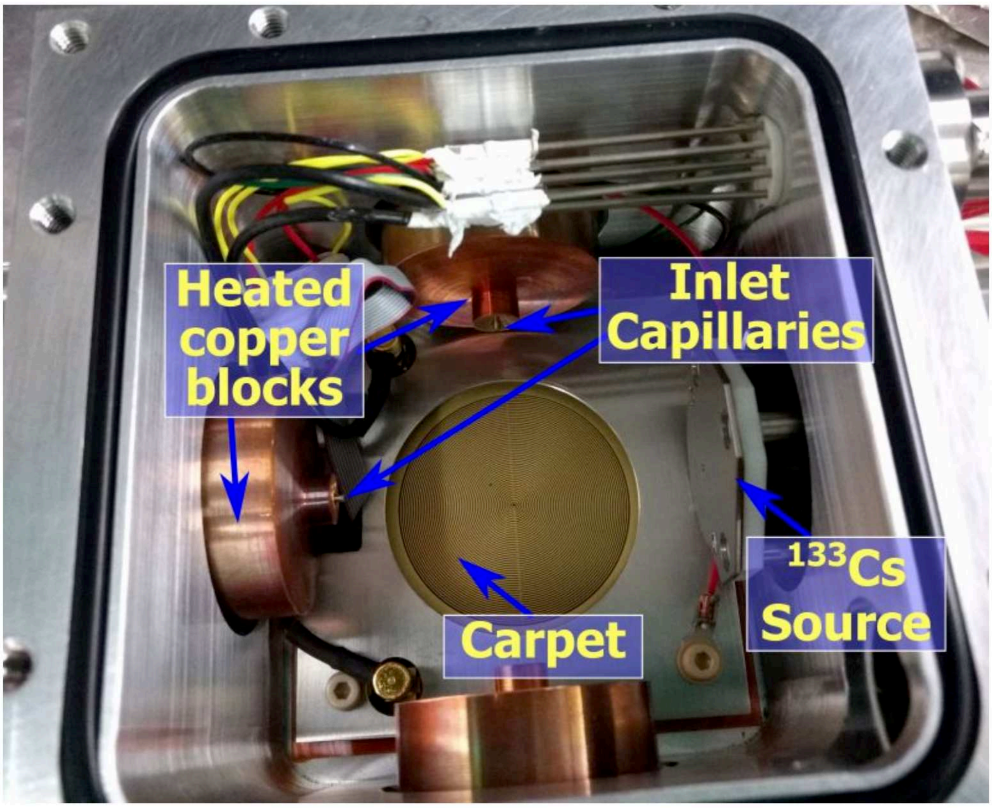

Figure 3.3.3: Photograph of the insides of the API from atop with top lid removed. Two heated inlet capillary modules are mounted from the left and the far side with the capillaries slightly protruding. From the right a ^{133}Cs ion source is mounted. The RF carpet at the bottom will move ions toward the nozzle at its center.

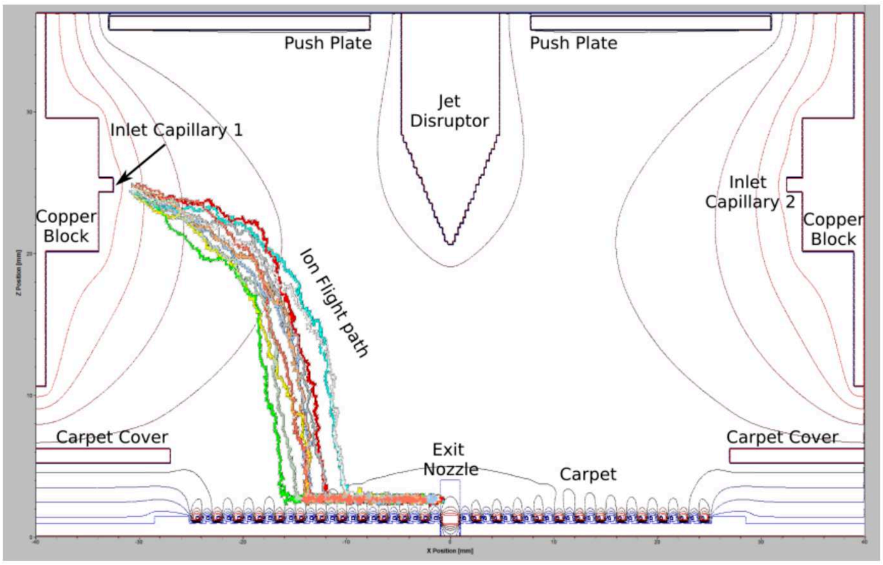

Figure 3.3.4: Simulated trajectories of different singly-charged ions of 322 u initialized with randomized position and velocity spread after entering through the inlet capillary 1. The gas jet from the ion inlet toward the jet disruptor was not taken into account.

constant, while the RF amplitude of 10 - 150 $\mathrm{V_{PP}}$ and its frequency of 0.5 - 20 MHz are varied. In addition, the influence of the electrode density has been investigated (1 - 4 electrodes/mm).

Figure 3.3.5 shows the transport efficiency for different electrode densities for singly-charged caffeine ions of 195 u. The electrode density refers to the ring electrode distance on the RF carpet. A frequency range between 1 - 4 MHz requires a constant, low RF amplitude for full transport efficiency. This frequency range is lower for lower electrode densities, while the required RF amplitude increases. Additionally, outside this frequency range the slope of the required amplitude with rising RF frequency becomes steeper, implying a less narrow acceptance regarding variation in mass, pressure, geometry, and ion optics. Since the range of transporting frequencies at low amplitudes and thus the range of transported mass-to-charge ratios is very narrow at 1 electrode/mm and only slowly increases above 2 electrode/mm, the latter configuration was chosen for the API.

Figure 3.3.6 compares the transport efficiency for ions of different masses (195 u and 100 u) at an electrode density of 3 electrodes/mm. The optimum transport frequency with the least required amplitude decreases by 500 kHz for higher masses in both cases, while the slope of required amplitude for transportation increases by 1 V/MHz. Thus, transporting a larger mass range with a slightly increased amplitude at a fixed frequency is feasable.

The RF carpet with 2 electrodes/mm was designed, commissioned, and implemented into the API. It is operated with an rectangular RF with a frequency of 2 MHz and an amplitude of 60 $\mathrm{V_{PP}}$. During operation, the carpet RF required a 40 $\mathrm{V_{PP}}$ higher amplitudes than simulated, probably due to the non-ideal RF shape and varying pressure regions due to the flexible amount of inlets. A 3 electrodes/mm carpet has been built in preparation to improve mass acceptance in the future.

3.4 Beam Preparation System

The *beam preparation system* as shown in Figure 3.4.1 is a series of RFQs operated in different pressure regions and is used to transport, filter, cool, bunch, and inject ions into the analyzer.

The RFQ rods are either made of stainless steel or resistive material in case a voltage gradient needs to be applied. While ideal RFQ rods, as described in Section 2.5.1, have a hyperbolic shape, the non-ideal electric field caused by the easier-to-manufacture cylindrical shape can be compensated by choosing the correct radius of and distance between rods. According to [Reuben et al. 1996], the ideal fraction to minimize deviations is $\eta = \frac{R}{r_0} \approx 1.14511$, where R is the rod radius and r_0 is the distance between the beam axis and the electrode surface. The RFQs in this device were chosen with $R = 4\,\mathrm{mm}$ and $r_0 = 3.5\,\mathrm{mm}$ resulting $\eta = 1.142\,86$. A DC gradient of 23 V is applied along the RFQs to transport ions toward the *trap* RFQ.

After exiting the carpet nozzle, ions enter the first section of the beam preparation system, the *transmission control* RFQ. This 20 cm long RFQ at $3 \cdot 10^{-3}$ mbar pressure collects ions from the carpet and controls their transmission toward the next chamber. Typical RFQ amplitudes are 60 - 130 $\mathrm{V_{PP}}$ at 1 MHz, corresponding to a pseudopotential depth of 3 V. Depending on the used ion source, the ion production rate can fluctuate, for example due to analyte inhomogenities or external influences. The radiofrequency voltage of the transmission control RFQ can be modulated to reduce ion transmission linearly, to keep the ion current in the trap consistent over time.

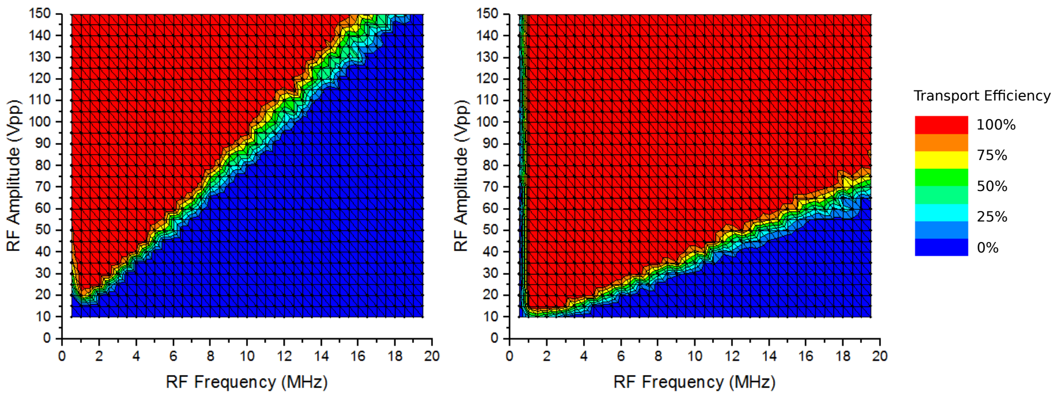

(a) 1 electrodes/mm **(b)** 2 electrodes/mm

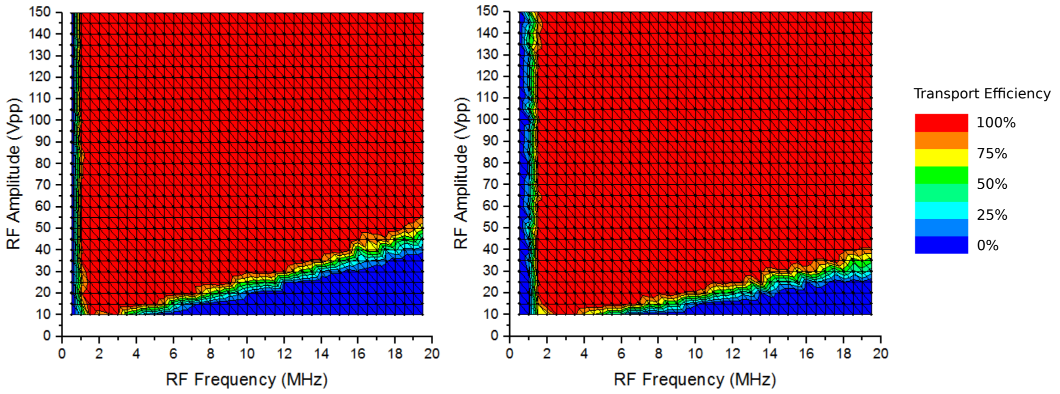

(c) 3 electrodes/mm **(d)** 4 electrodes/mm

Figure 3.3.5: Carpet transport efficiency simulation for singly-charged ions with a mass of 195 u. Comparison of different electrode densities. Red color indicates complete transmission and blue indicates no transmission.

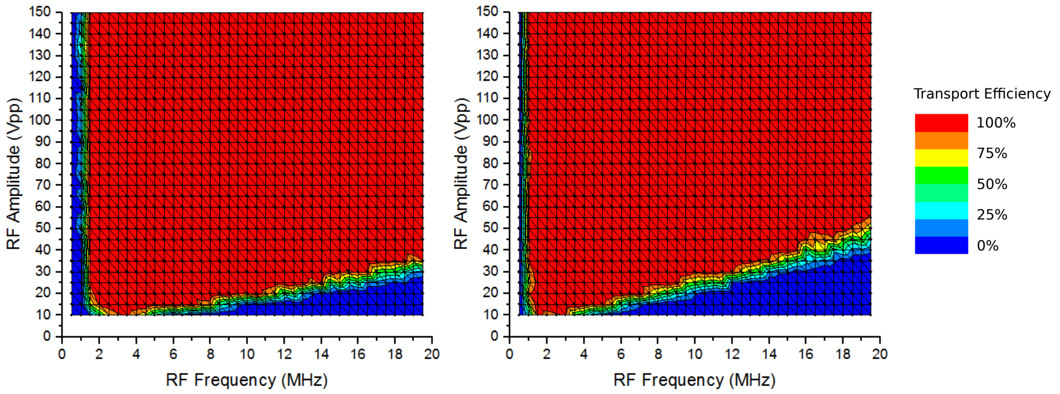

(a) 3 electrodes/mm, 100 u **(b)** 3 electrodes/mm, 195 u

Figure 3.3.6: Carpet transport efficiency simulation. Comparison of different ion mases. Red color indicates complete transmission and blue indicates no transmission.

A constant detection rate allows the device to avoid space charge, clustering, and dead time effects for high-intensity signals without permanently losing sensitivity. By switching off the RF voltage for a fraction of a measurement cycle, the ion rate can be precisely reduced. While the RF voltage is off, the ions hit the electrodes of the transmission control RFQ and are lost. This effect is primarily independent of mass-to-charge ratio and ion mobility. The shortest on-time of the RF, which still allows the ion to be transmitted, is defined by the drift time required to pass the transmission control RFQ. For 322 u, the minimum drift time is 300 µs corresponding to 0.75 % transmission at a repetition rate or 25 Hz.

The next chamber contains a *mass filter* RFQ. Its Mathieu parameters a_x and q_x can be set by adjusting the RF voltage amplitude and adding a transversal DC voltage (see Section 2.5.2). A typical working point for narrow filtering is $q_x = 0.7$, $a_x = 0.22$, resulting in RF amplitudes of 100 - 700 $\mathrm{V_{PP}}$ at 800 kHz (corresponding to 90 - 623 u), allowing to filter ions of different mass-to-charge ratios. Figure 3.4.2 shows the transmission measured for different mass filter settings for ^{133}Cs.

Behind the mass filter, ions are guided into the *cooler* RFQ. This RFQ guides the ions through an encapsulated chamber with a pressure-regulated gas inlet of N_2 buffer gas. The ions are cooled and collected at a pressure of $1 \cdot 10^{-2}$ mbar. The RF amplitude of the cooler RFQ with 1.1 MHz of 200 - 500 $\mathrm{V_{PP}}$ corresponds to a pseudopotential depth of 30 V for 100 - 650 u.

Ions then gather in front of a tailing segment of the cooler RFQ. While it shares the cooler RFQ RF voltage, its DC potential is switched between 50 V and 5 V. The higher potential prevents the ions from leaking into the trap during re-trapping operations, increasing the suppression power within tandem mass spectrometry. During injection into the trap RFQ the potential switches to 5 V.

The last section of the beam preparation system is the *trap* RFQ, which is formed by an RF segment surrounded by two apertures. The trap is operated with a DC offset of 0 V at 0.9 MHz with an RF amplitude of 160 - 400 $\mathrm{V_{PP}}$ for a pseudopotential depth of 30 V to ensure ion storage of 100 - 650 u. The apertures can be individually switched, as seen in Figure 3.4.1, to operate injection from the cooler-RFQ, extraction to the analyzer, or re-trapping (see Section 2.6.5). The apertures before/after the RFQ are set to 0 V/28 V for injection, 25 V/28 V for storing, 300 V/−300 V for extraction, and 1 - 20 V for re-trapping. Once the ions are extracted, they pass a steering quadrupole lens with an offset of −2500 V and enter the analyzer, where they have a kinetic energy of 1300 eV.

3.5 Analyzer

The MR-TOF-MS *mass analyzer* is the device's core component, in which the ions are separated with respect to their mass-to-charge ratio in time before detection. Figure 3.5.1 shows a schematic figure of the analyzer.

Ions first pass an *Einzel lens* to create a focal point in the center of the drift tube E5. Afterward, they enter the ring electrodes E1 to E9, which control the number of turns, apply the time focus shift toward the detector and focus the ion beam to ensure the ion-optical aberraton conditions

$$(x|x) = (T|xx) = (T|\delta) = (T|\delta\delta) = 0 \quad , \tag{3.5.1}$$

making the linear and second order aberration coefficients in position and energy vanish.

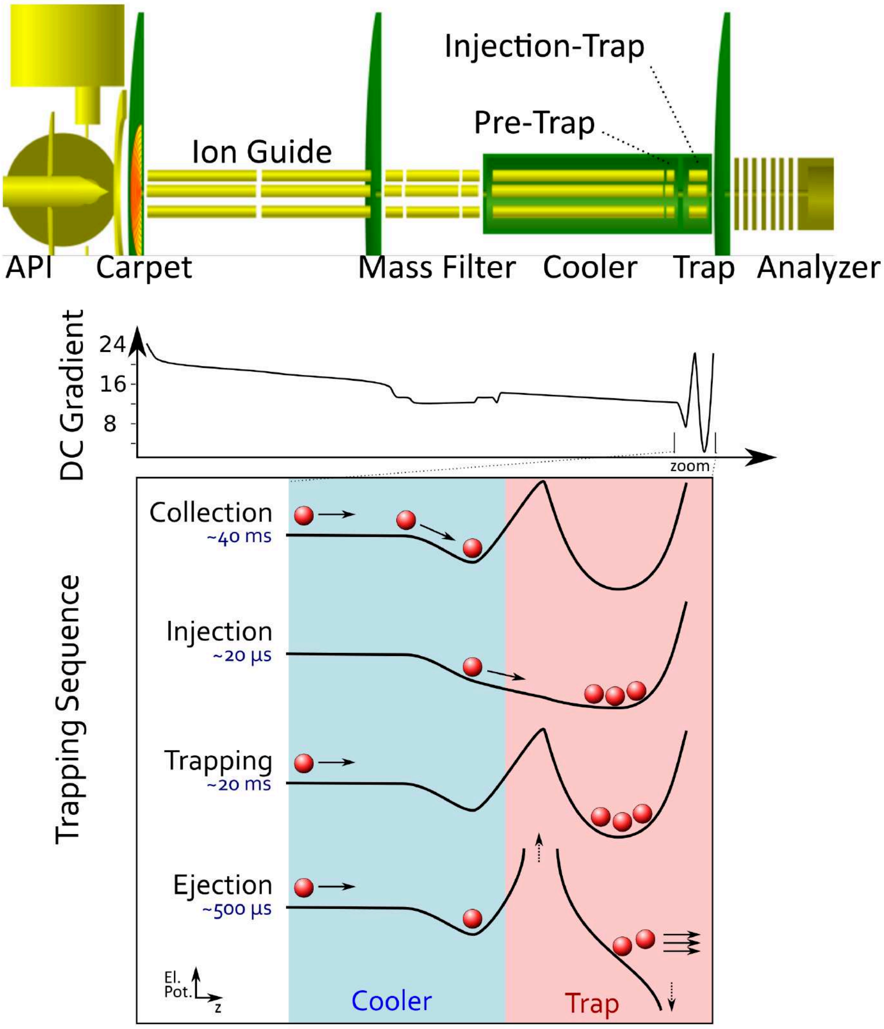

Figure 3.4.1: Schematic figure of the beam preparation system, potentials along the axis of the device, and the trapping and ejection time sequence.

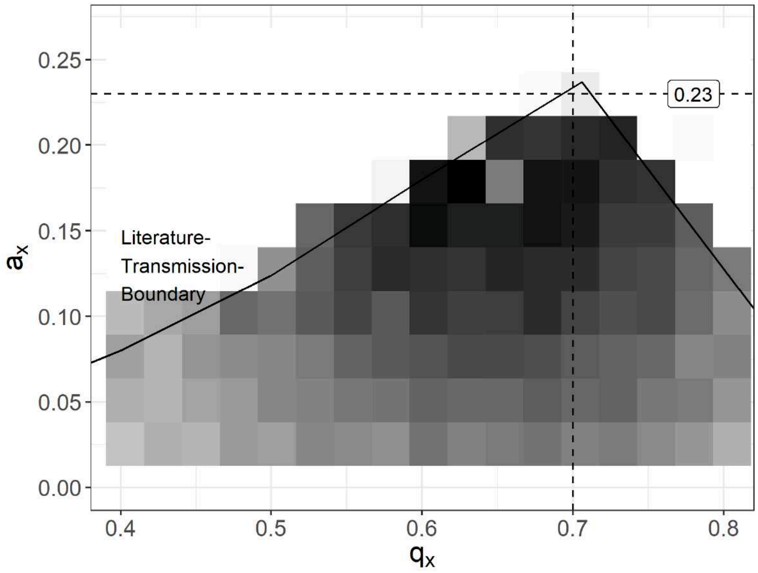

Figure 3.4.2: Transmission efficiency of ^{133}Cs through the mass filter RFQ at different sets of the Mathieu parameters a_x and q_x. Darker areas denote higher ion rates at the detector. The black line shows a section of the stability diagram.

The voltages applied to electrodes E1 to E4 and E6 to E9 are switched according to the scheme described in Section 2.6.3 according to a given timing sequence.

The *mass range selector* dipole in the center of the drift tube E5 has two purposes. When ions pass for the first time, it applies a dipole field to steer the flight path angle of the ions to align with the analyzer axis. Together with the action of the trap steerer, this corrects geometrical misalignments of the trap and analyzer in 2 dimensions regarding angle and offset. Typical steering voltages are $30\,\mathrm{V_{PP}}$ offset compared to the drift tube potential. Its second application offers the eponymous feature of selecting the transmitted mass range. A deflecting dipole field switched at the correct frequency and duration deflects undesired ions while letting ions of interest pass. The deflection voltage typically amounts to $140\,\mathrm{V_{PP}}$ with a mass-dependent frequency, as described in Section 2.6.4.

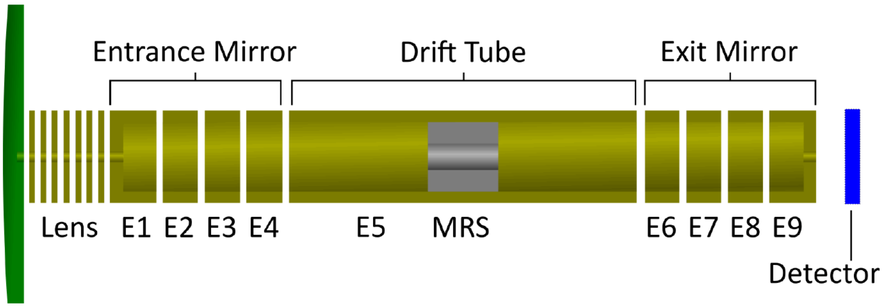

Figure 3.5.1: Schematic figure of the analyzer showing the Einzel-lense, entrance mirror electrodes E1, E2, E3, and E4, exit mirror electrodes E6, E7, E8, and E9, Drift tube electrode E5, the Mass Range Selector (MRS), and the detector.

3.5.1 Timing Sequences

Several potentials of the MR-TOF-MS must be changed periodically at high frequency and precision to control pulsed extraction, switch the analyzer potentials, and to supply the RF generators. An FPGA-based device called *trigger system* built in [Jesch 2016] generates the necessary TTL signals to control the voltage switches and RF amplifiers.

The timing sequence that controls the switching of all electrode potentials guarantees transmission and minimal influence of the switching fields on the ion's flight path. A visualization of the timings when potentials are switched is displayed in Figure 3.5.2.

The ions are continuously produced, travel through the API, transmission control, mass filter, and cooler RFQs up to the latter's last segment. Its higher potential blocks transmission while keeping ions in the cooler-RFQ to prevent leakage into the trap.

When injecting ions into the trap, the last cooler RFQ segment and its adjacent trap aperture switch their potential to allow transmission (*open*). The injection time scales with mass-to-charge ratio. After the ions arrive in trap, both aperture potentials are switched high to trap the ions in the RFQ (*close*) until the analyzer potentials are prepared and the ions are ejected toward the analyzer.

Once the ions enter the analyzer, the timing sequence described in Section 2.6.3 applies the time focus shift toward the detector and lets ions revolve for a given number of isochronous turns. The trigger system realizes the sequence for an arbitrary ion species by scaling known TOF values for ^{133}Cs as shown in Table 3.2 with $\sqrt{m/q}$. Once the ions have traveled the desired number of turns, the second mirror opens, and the ions impact on the detector.

Name	Injection	Analyzer Center	TFS Turn	IT	Center to Detector
Symbol	t_{inj}	t_{del}	t_{TFS}	t_{IT}	t_{det}
Time (µs)	7.5	7.9	25.275	22.6745	11.931

Table 3.2: TOF values for ^{133}Cs ions.These values can be used to scale the timing sequence for any other ion.

When re-trapping is performed, the entrance mirror is opened, and at a set re-trapping time, the trap apertures are switched to a re-trapping potential. The re-trapping time t_{ret} after trap ejection for N_{ret} turns and mass-to-charge ratio m/q is calculated using the TOF values from Table 3.2

$$t_{\mathrm{ret}} = (t_{\mathrm{del}} + t_{\mathrm{tfs}} + t_{\mathrm{IT}} \cdot (N_{\mathrm{ret}} - 1.25) + t_{\mathrm{det}}) \cdot \sqrt{\frac{m/q}{m(^{133}\mathrm{Cs})/1e}} + t_{\mathrm{adj}} \qquad (3.5.1.1)$$

with t_{adj} used to fine-adjust to the measured value. Once the ions have been cooled down after re-trapping, a frequency generator applies an RF voltage to induce ion excitation and thus CID. Afterwards, the ions are again ejected into the analyzer for mass measurement.

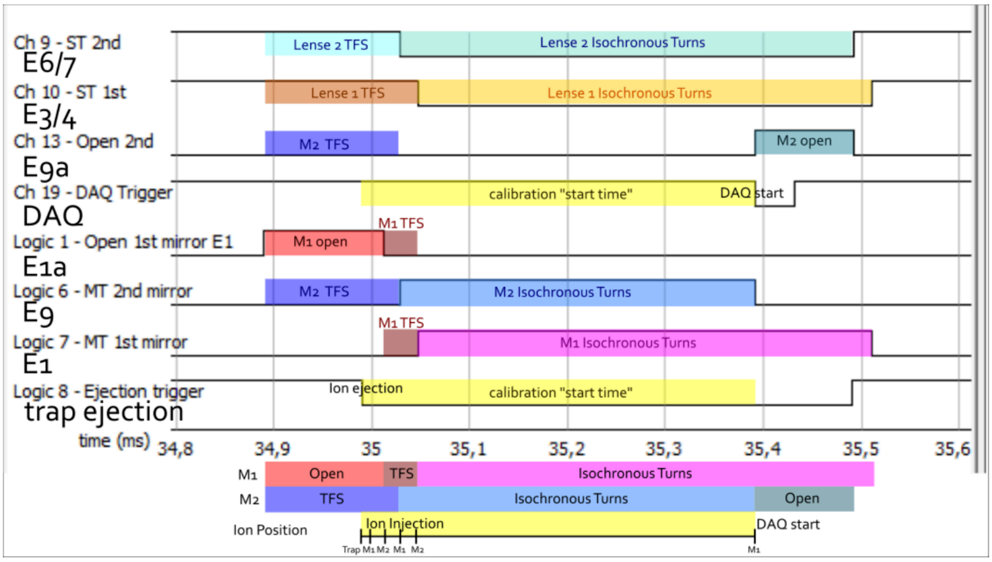

Figure 3.5.2: TTL preview of a normal measurement cycle. Relevant times are highlighted. M_1 and M_2 refer to the entrance and the exit mirror, respectively. The analyzer electrodes are labeled E1 (entrance mirror) to E9 (exit mirror). The TTL channels labeled *E1* to *E9* regulate when the corresponding electrode assumes the potential for isochronous turns (E1/2 and E8/9 high, E3/4 and E6/7 low) or for the time focus shift. The channels labeled *E1a* and *E9a* Open the electrostatic mirror electrodes E1 and E9 respectively when high.

3.6 Vacuum System

The setup is divided into several different vacuum chambers, which correspond to different pressure regions. The ions can pass from one chamber to the next through small apertures with diameters of 0.5 - 2 mm. Figure 3.6.1 depicts a schematic view of each chamber with connected pumps, gas inlet lines, and pressure gauges.

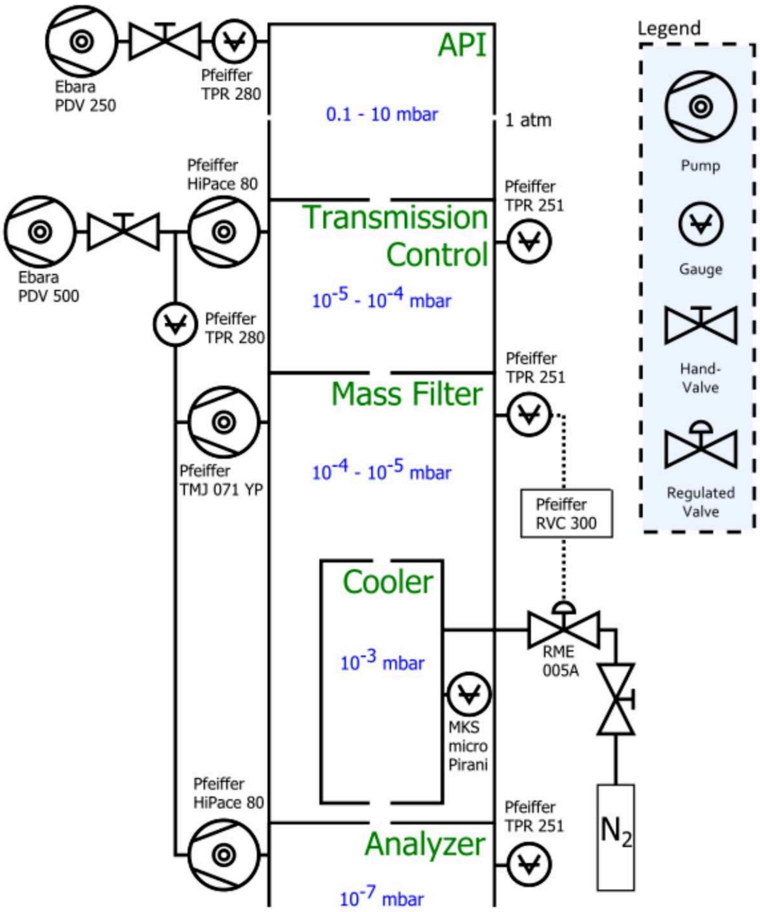

Figure 3.6.1: Schematic figure of the vacuum system of the MR-TOF-MS. Labels used as designators are marked in green. Typical pressure regions are printed blue.

The API chamber at the top is connected to an Ebara PDV 250 roughing pump and features two ion inlets toward atmospheric pressure. An Ebara PDV 500 roughing pump provides the backing pressure for the turbomolecular pumps of the lower chambers. The following vacuum chambers of the transmission control RFQ, mass filter RFQ, and analyzer are connected to the turbomolecular pumps Pfeiffer HiPace 80, Pfeiffer TMJ 071 YP, and Pfeiffer HiPace 80, respectively.

Pressure gauges are installed for surveillance at the roughing pumps (Pfeiffer TPR 280) as well as at the lower chambers of transmission control, mass filter, and analyzer (Pfeiffer TPR 251). The cooler RFQ vacuum chamber inside the mass filter RFQ vacuum chamber is also connected to a nitrogen buffer gas line, regulated by an electric valve (RME 005A) on the pressure value in the mass filter vacuum chamber. Mechanical valves are installed for maintenance near the roughing pumps and the nitrogen gas line.

3.7 Electronics

3.7.1 Radio Frequency Voltage Generation

The radio frequency voltage required by transmission control, mass filter, cooler, and trap RFQ is produced by using a low voltage switch controlled by the trigger system, amplified by resonant excitation in an LC circuit, and divided into two 180° phase-shifted signal by two toroidal inductor coils [Kondradi and S. Ayet n.d.].

By using an LC circuit, the input TTL signal of around 1 MHz can be amplified to a set of phase-shifted sinusoidal signals up to 1 kV in amplitude. The resonance frequency responds as $\omega = 1/\sqrt{LC}$. Here the capacitance is dominated by the SHV cables and feedthroughs. By controlling the driving frequency f by the trigger system and the input voltage by an ISEG crate module, the RF amplitude U_{RF} and thus the Mathieu parameter $q_x \propto U_{\mathrm{RF}}/((m/q) \cdot f)$ can be adjusted according to the ion of interest's mass.

Since the beam preparation system requires a DC gradient to push ions toward the trap, the produced RF signal is connected to an RF-DC mixing board. The two RF signals are coupled to the mixing board's output by capacities around 10 nF while coils around 1 mH couple the DC gradient of the two inputs. Figure 3.7.1 shows the mixing board of the transmission control RFQ.

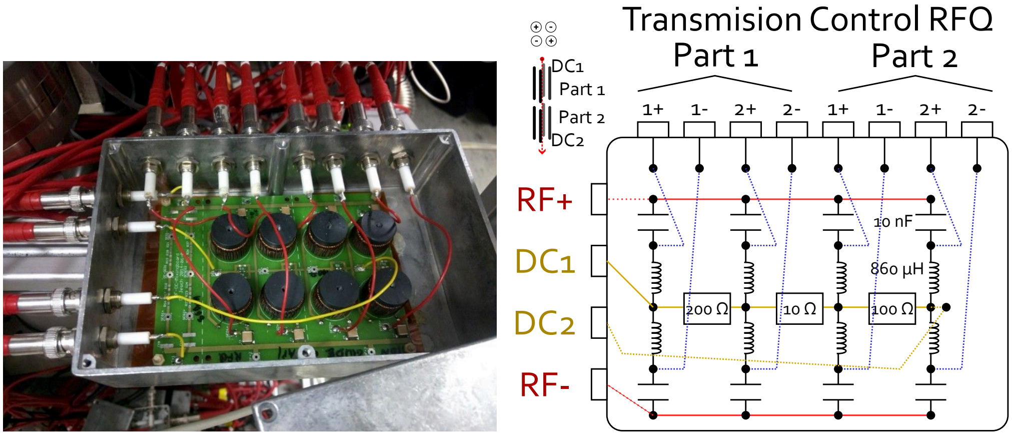

Figure 3.7.1: Left: Photograph of the RF-DC mixing board to the transmission control RFQ. RF+ and RF- refer to the two phase-shifted RF phases. IG1 and IG2 refer to the DC voltage between which a gradient is produced along the RFQ rods. Inputs are on the left side (yellow cables for DC "IG1" and "IG2", red cables for RF "RF+" and "RF-"). The eight outputs to the two-segmented transmission control RFQ are at the top.
Right: Schematic figure of the circuit. The connections to the box outputs are dotted blue.

In contrast to the other RF signals, the RF applied to the carpet has a rectangular pulse shape. The directly driven rectangular RF generator developed by [Jesch 2008] is used here and can provide 0 - 100 $\mathrm{V_{PP}}$ at frequency of 0.5 - 4 MHz.

3.7.2 High-Voltage Switches

Custom-made high-voltage switches use the TTL signals generated by the Triggerbox to apply the generated potential sequence described in Section 3.5.1 [S. Ayet n.d.]. They allow voltage changes of up to 2 kV at ramp times below 300 ns and can be used in series for complex sequences. Switches with lower voltage ratings control trap-injection, -extraction, re-trapping, and MRS operation. The high-voltage switches to operate the analyzer electrodes are additionally stabilized.

3.7.3 Passive Voltage Stabilization

Since ions experience the electric analyzer fields several hundred times, ion optics require highly stabilized voltages. Therefore a fourth-order low-pass filter, with four 1 µF capacitors and 160 kΩ resistors, is used to filter high-frequent electric noise. The cut-off frequency above which the output amplitude falls below 70 % of its input is $f_c = 1\,\mathrm{Hz}$.

The high voltage switches for the analyzer electrodes use a separate device with a fourth-order low-pass filter. E4 and E6 use a different first-order cut-off frequency of $f_c = 5.3\,\mathrm{Hz}$ to support voltages of up to $-5\,\mathrm{kV}$.

3.7.4 Trigger System FPGA

The FPGA-based *trigger system* board can output thirty-two independent TTL signals using LEMO connectors. Internally there are also thirty-two *channels* with fixed frequency and duty cycle on the 5 ns precision level whose output can be logically combined using up to sixteen AND, OR, XOR, and NOT gates, the *logic boxes*.

Each channel, logic box, and up to six input signals can be used as trigger or linked to one of the outputs. For diagnostic purposes, sixteen additional outputs can be sent directly toward a digital oscilloscope with a flat cable. The computer connects to the 12-volt-powered trigger system with a serial COM port.

3.8 Commonly used Parameters

This section lists common parameters of the setup. Only deviating setup parameters will be given in later chapters. The RFQ RF amplitude was adapted to result in the given pseudo potential. The double aperture DA1/DA2 is posititioned between the transmission control RFQ and the mass filter RFQ. The aperture MFCO is between the mass filter RFQ and the cooler RFQ. The Trap steerer quadrupole electrodes are labeled clockwise in beam-direction from B to E according to their connected feedthrough-label. A list of common parameters for operating the ion sources can be found in Table 3.1. Important potentials concerning the electrodes of the mass analyzer are listed in [Lippert 2016].

Section	Parameter	Value
API DC Potentials	Inlet Capillaries	20 V
	Push Plate	45 V
	Carpet Cover	30 V
	Carpet Outer Ring DC	28 V
	Carpet Inner Ring DC	26 V
	Carpet Nozzle	25.5 V
RF-Carpet	Frequency	2 MHz
	E_{pseudo}	20 V
Transmission Control RFQ	E_{pseudo}	2.5 V
	RF Frequency	1050 kHz
	Rod Radius	3.5 mm
Mass Filter RFQ	q_x-value	0.69
	RF Frequency	719 kHz
	Rod Radius	3.5 mm
Cooler RFQ	E_{pseudo}	30 V
	Frequency	1136 kHz
	Rod Radius	3.5 mm
Trap RFQ	E_{pseudo}	31 V
	Frequency	943 kHz
	Rod Radius	3.5 mm
Pressures	API (closed)	0.1 mbar

Continued on next page

Continued from last page

Section	Parameter	Value
	API (1 inlet)	3 mbar
	API (2 inlets)	5 mbar
	Transmission Control	$3 \cdot 10^{-4}$ mbar
	Mass Filter	$5 \cdot 10^{-5}$ mbar
	Cooler	$1.2 \cdot 10^{-2}$ mbar
	Analyzer	$1.3 \cdot 10^{-7}$ mbar

4 Developing a software suite for MR-TOF Mass Spectrometers

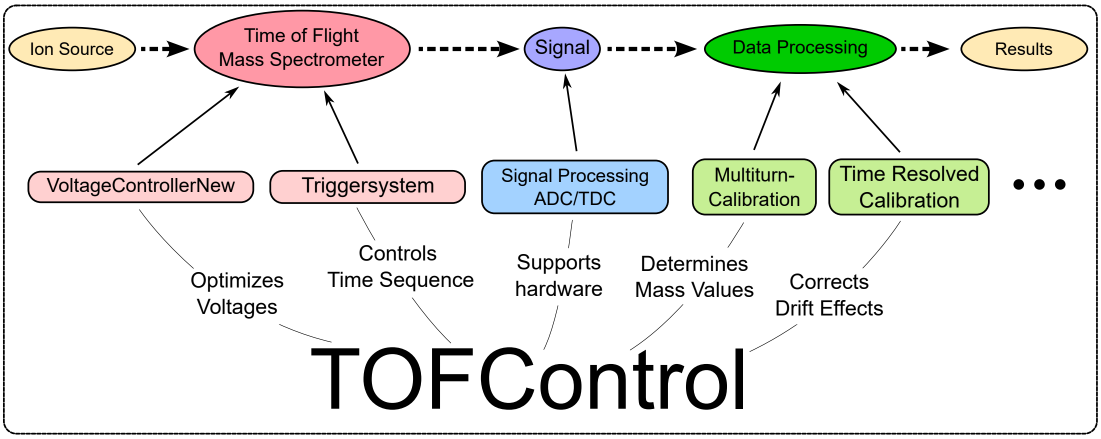

Figure 4.0.1: Fields of operation for the TOFControl software. The software controls essential parts throughout the measurement process, from optimizing voltages and controlling the timing sequence to acquiring data and assisting in analysis.

Custom-tailored software for hardware control, data acquisition, and analysis is essential to control a complex system such as the MR-TOF-MS of this work to its full capabilities. Continuing the work described in [BERGMANN 2015], a new software called *TOFControl* based on *Mass data Acquisition* by Alexander Pikhtelev is developed and fine-tuned to the specific features of multiple-reflection time-of-flight mass spectrometers.

The software offers assistance in controlling the used hardware, processes the detector signal from the digitizers, and analyses the acquired data. Figure 4.0.1 shows a schematic of the areas where the TOFControl software performs essential functions.

The hardware that TOFControl controls include devices that manage the applied voltages (power supply crate by W-IE-NE-R), control the timing sequence (custom-build FPGA, see Section 3.7.4), generate the RF (custom-build RF amplifiers, see Section 3.7.1), or digitize the detector signal (ADC, TDC, see Section 2.7.2).In addition, Sensors and external software can be connected to add synchronized data during a measurement (e.g., Labjack T7-Pro by the LabJack Corporation, Lakewood, USA).

During acquisition, the software offers various graphical tools to, for example, monitor rates of ion species, adapt setting parameters (like the mass range), or automate analysis in parameter scans (like turn number scans). It also offers logging of critical parameters that are automatically calculated and a feedback loop to control the connected hardware based on such parameters. In order to make efficient usage of available memory, two data storage types are supported. Depending on the digitizer used and detection rate, the user can switch between histogram- and event-based data storage during operation. Procedures for long-term acquisition and automated storage further relieve memory requirements.

Data analysis procedures include different calibration methods tailored for MR-TOF-MS, data corrections for voltage drifts, and various visualization techniques for mass measurements and parameter scans. The position of molecules in the mass spectrum can be estimated and visualized based on the NuBase2020 database. In reverse, peak identification procedures help to identify molecular compositions. With the setup data available and sophisticated calibration procedures, the software can deconvolute spectra with ions of different turn numbers and identify possible chemical compositions by analyzing the mass excess. TOFControl also offers a versatile formula parser that allows the time sequence control and automatic analysis components to be highly flexible.

The software is written in C++ in the Embarcadero C++ Builder framework and contains roughly 95 000 lines of code, excluding third-party libraries. A 50-page long manual has been written to explain its usage and algorithms [Bergmann 2023].

4.1 Data Visualization

Real-time visualization of raw and processed data is vital to the system's usability. TOFControl provides extended visualization techniques during acquisition or later at data analysis. By utilizing multithreading and parallelization, the displayed information is updated in real time during measurement and can inform the operator of the system status and data quality. Figure 4.1.1 shows the user interface with an assortment of visualizations.

4.2 Optimizer

A core part of the semi-automatic capabilities is realized using the *voltage optimizer* interface. While it can control most setup voltages, it can also access parameters of the timing sequence and other connected devices. It offers multidimensional scans and sophisticated optimizers such as the *simplex downhill* [Nelder et al. 1965] and the *evolutionary* [Back 1996] algorithms for free or dependent outputs. Automatic analysis is realized with a formula parser to allow access to all setup parameters, a peak detection algorithm, and Gaussian fit parameters. While automated analysis procedures and real-time visualization offer quick results, scans can be reevaluated and visualized afterward to conform to changed analysis parameters.

Typical applications include steerer dipole voltage scans for beam alignment, re-trapping time scans to optimize the re-trapping window, turn-number scans for characterizing the MRP, transmission diagrams of the RF carpet (RF amplitude vs. frequency), and mass range scans for spectrum patching (see Section 4.7).

4.3 Trigger System Software

A graphical user interface that simplifies communication with the device was developed and added to the TOFControl software to control the trigger system. It provides control at different levels of expertise, allowing experts to implement new features while offering beginners easy control of existing sequence setups (See Figure 4.3.1).

The constants section represents the low-expertise level of operation. Here operators can type in values such as the mass-to-charge ratio to measure, the number of turns, the mass range transmitted by the MRS, or the re-trap-time, from which the software automatically calculates the necessary timings.

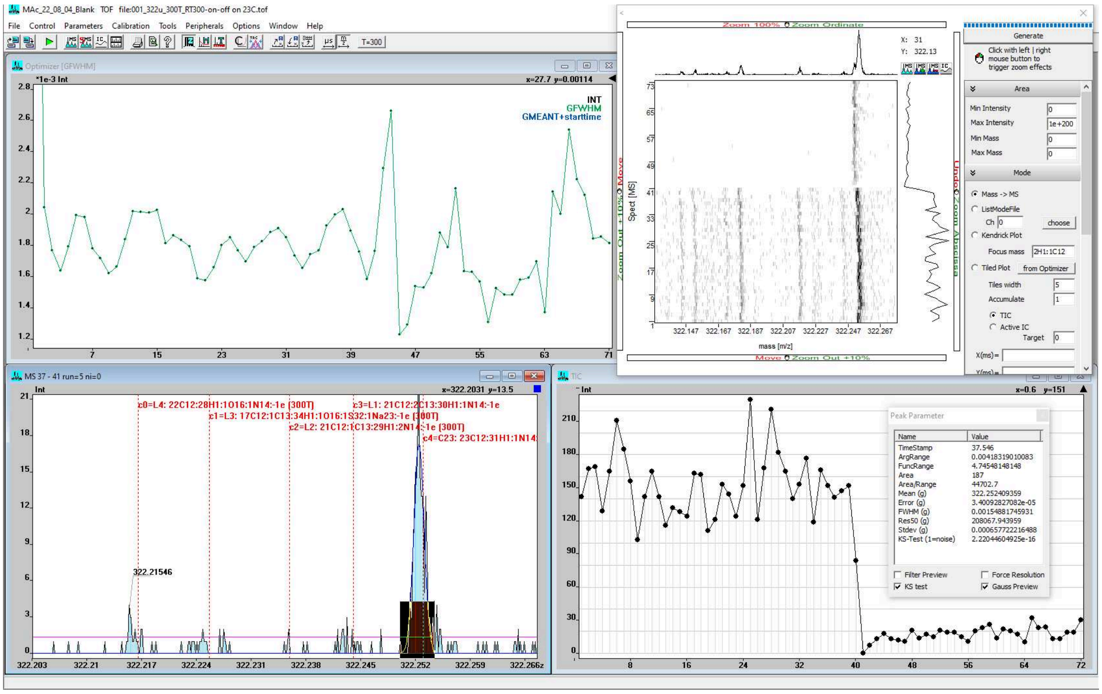

Min Intensity 0
Max Intensity 1e+200
Min Mass 0
Max Mass 0

● Mass -> MS
○ ListModeFile
Ch 0
○ Kendrick Plot
Focus mass 2H1:1C12
○ Tiled Plot
Tiles width 5
Accumulate 1
● TIC
○ Active IC
Target 0
X(ms)=

Name	Value
TimeStamp	37.546
ArgRange	0.00418319010083
FuncRange	4.74548148148
Area	187
Area/Range	44702.7
Mean (g)	322.252409359
Error (g)	3.40092827082e-05
FWHM (g)	0.00154881745931
Res50 (g)	208067.943959
Stdev (g)	0.000657722216488
KS-Test (1=noise)	2.22044604925e-16

☐ Filter Preview ☐ Force Resolution
☑ KS test ☑ Gauss Preview

Figure 4.1.1: The user interface of TOFControl with its most frequently used interfaces.
a) Main Interface to acquire and visualize data. A menu at the top gives access to most features, while a list of buttons below allows quick access to popular features. The blue window shows the total ion current over time (labeled TIC). The red window shows an accumulated mass spectrum (labeled MS) with markings for literature masses and a peak labeled with a mass-to-charge ratio value of 322.216 67 u/e labeled.
b) 2D of all spectra (abscissa) taken during the measurement (ordinate) with color representing signal rate. Projections to the plot's top and side represent the total sum spectrum and the total ion current, respectively.
c) Parameters of the area marked inside the mass spectrum, including range, sum, and Gaussian fit parameters.
d) Stability diagram and control interface for the used mass filter RFQ.
e) Acquisition parameter dialog to control mass region, accumulation time, bin-width, and digitizer-related parameters.

The four tabs represent the expert level to control the FPGA channels, logic boxes, and outputs. Each channel property (duration HIGH, duration LOW, frequency, and duty cycle) can be individually set or calculated using other channel properties or constants. The software also calculates the produced TTL, assuming the TTL logic and building upon an imaginary initial trigger. This setup can be exported into an XML file and is automatically saved with each measurement.

Aside from communication levels, integration of the trigger system controls in the data acquisition and analysis software TOFControl also offers advanced features. Examples are scanning parameter ranges, automated transport time measurements, and easy access to setup time settings for mass calibration.

4.4 Time-Resolved Calibration

TOF spectra generated from a closed-path analyzer arrangement require further data processing and calibration to be converted into meaningful m/q spectra. To provide a satisfying calibration, TOFControl utilizes peak detection algorithms to determine

c(1) IonOfInterest 322 F
c(5) MRSCenter 322 F
c(9) Cs1T 22.6659 F

Channel 22 ON F
MRS Cleaning Wind...
Single Shot
t_ON: 1.270085m
t_Delay: 67.545u
Trigger: LB 08: Ejec.
Edge: Falling
Inverted: Norm Out 22

Channel 23 ON F
MRS Cleaning Timin...
Cycle: Freq/Duty
Duty(%): 80.351573
Frequ.: 56.705415k
Trigger: CH 22: MR.
Edge: Rising
Inverted: Inv

Logic Box 0 (null)
CH 02: Cooling Normal XOR
CH 03: RT/MS Normal
False Normal
False Normal Normal

Figure 4.3.1: Screenshot of the TOFControl trigger system user interface.
(a): User interface and channel overview;
(b): zoom into settings for constants, channel, and logic boxes;
(c): calculated TTL output.

a calibrant's exact TOF, which are used to determine the calibration parameters in Equation (2.6.2.5).

If the number of calibrants exceeds the number of free parameters of the equation, a Simplex-Downhill algorithm (explained in [Nelder et al. 1965]) minimizes the square residual sum weighted with their statistical errors. The error of the optimizer is estimated by repeating this process for each input parameter changed within its statistical error. Thanks to self-initializing starting parameters and the robust optimizer algorithm, calibration, including error estimation, requires less than a second and can be executed during the measurement. With knowledge about the turn number and charge state, estimated by mass excess, simulations, and comparison with other measurements, exact mass-to-charge ratio values can be determined.

A problem of static calibration is posed by changing electric fields over time. The effect of changed flight paths can be represented in a change of calibration parameter b, which represents the ratio of flight path length per turn over the analyzer length (as shown in [Ayet San Andrés et al. 2019]). The *time-resolved calibration* uses a calibrant to create grid points of b over time, which are then linearly interpolated to create a b_i value for each acquired spectrum. In order to create a grid point of b, the data is divided into so-called blocks by a given measurement time interval. All spectra within a block are accumulated, and for a given mass range, the chosen fitting algorithm is used to determine the calibrant's TOF value. The grid point for this block b_{block} is then calculated by using Equation (2.6.2.5):

$$b_{\text{block}} = \left(\frac{t_{\text{block}} - t_0}{\sqrt{\frac{m_{\text{calibrant}}}{a}}} - 1 \right) \Big/ N \tag{4.4.1}$$

To create a summed-up, drift-corrected spectrum, individual spectra are first calibrated with a, t_0, and b_i (see Equation (2.6.2.5)), then re-binned to align the histograms to each other and finally accumulated using the original b. The procedure is demonstrated in Figure 4.4.1 for a 36 h long measurement of $^{143}\text{Ba}^{2+}$ with the MR-TOF-MS of the FRS Ion Catcher at GSI. The original data shows strong TOF drifts of 200 ns introduced by the temperature difference between day and night. The TRC correction lets the TOF drifts vanish, and an MRP of above 500 000 is reached, which allows resolving the smaller peaks of $^{157}\text{Sm}^{2+}$ and $157\,^{\text{P}}\text{m}^{2+}$. While this procedure is well suited for correcting TOF drifts in the analysis process, it does not prevent them and their consequences during acquisition, for example, leaving the observed mass range or changes in ion optical focusing.

4.5 Feedback Software Stabilizer

The combination of hardware control, data acquisition, and analysis in TOFControl makes a feedback control loop possible. This *Feedback Software Stabilizer* (FSS) controls connected hardware automatically and asynchronously depending on acquired data.

Multiple control loops of the form

$$Q_{\text{new}} = \left(a\frac{\Delta I_0}{I} + b\frac{\Delta I_n}{I} \right) \cdot (Q_{\text{old}} - e) + c \cdot \Delta I_0 + d \cdot \Delta I_n + Q_{\text{old}} \tag{4.5.1}$$

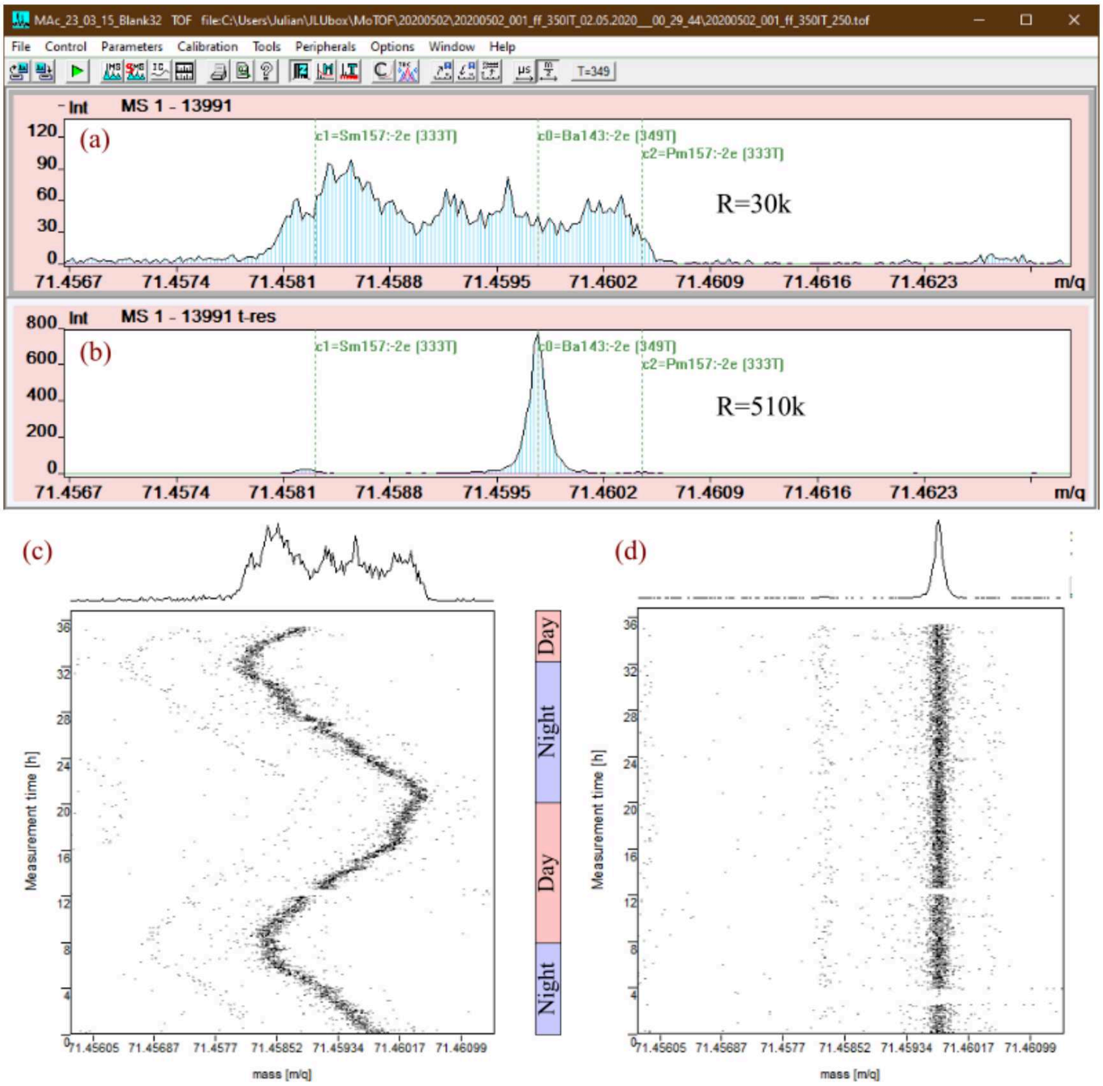

Figure 4.4.1: Screenshots of the applied time-resolved calibration in TOFControl. The measurement of $^{143}\mathrm{Ba}^{2+}$ was taken at the MR-TOF-MS of the FRS Ion Catcher at GSI for a duration of 36 h. Strong TOF drifts created by different temperatures during the day and night of up to 200 ns can be corrected using the TRC.
(a) shows a mass spectrum of the accumulated data without correction. **(b)** shows the TRC corrected mass spectrum. The mass lines can now be resolved, and an MRP above 500k is reached. **(c)** shows a heatmap of the uncorrected data of every spectrum (abscissa) during the measurement (ordinate) with a projection toward the TOF-axis at the top. **(d)** shows the same heatmap for the TRC corrected data with a reference for daytime (day=8:00-20:00, night=20:00-8:00).

can be set up to run in parallel. Here, Q is the adapted hardware parameter (e.g., voltage) with a resulting change from Q_{old} to Q_{new}. I is the observed variable (e.g., time-of-flight, which should be stabilized). ΔI_0 is the change compared to the fixed target variable I_0, and ΔI_n is the change within the most recent control loop iteration $(I_n - I_{n-1})$. The weights a, b, c, and d connect absolute and relative changes of I to Q. The parameter e allows for an offset for the weights for relative changes.

For most applications, most weights except those representing the relationship between Q and I are set to 0. a controls a relative change regarding a target value and thus is used to adapt voltages to stabilize the TOF. c controls an absolute change regarding a target value and can adapt the re-trapping time window to TOF shifts. b and d control reactions to shifts within the last control loop and thus can react to independent observables such as the temperature. Typically, slightly lower weights than the numerical solution are chosen to avoid oversteering at the cost of correction speed.

Possible hardware parameters Q include the time sequencing control, the applied voltages, and some digitizer settings. I is linked to an equation parser that can evaluate user-defined equations that may include the hardware parameters listed for Q as well as data-depending variables like signal rates, Gaussian fit parameters, moving averages, and other statistical algorithms.

4.5.1 Automatic Gain Control

The *Automatic gain control* (AGC) can stabilize the ion signal rate to avoid low statistics or space charge effects. By artificially reducing ion transmission within the beam preparation system in an adjustable manner, the ion rate after the AGC can be finely tuned to the requirements of the measurement [Stafford Jr et al. 1992]. The FSS realizes this feature by linking the detected signal rate to the transmission control RFQ RF modulation described in Section 3.4.

An example for the use of the AGC is shown in Figure 4.5.1. All weights in Equation (4.5.1) except $c = 0.0125\,\%/\text{counts/s}$ are set to zero. This weight relates to a change of the RFQ RF transmission gate per change of the ion detection rate relative to the target value of $I_0 = 50\,\text{counts/s}$.

The initial rate of 10 counts/s is automatically increased to match the target value by increasing transmission phase of the RF modulation by 2 %. After 200 s and 260 s, the rate is artificially doubled and then restored by the FSS. In both of these situations, the target rate is reached and stabilized within a minute.

4.5.2 Time-of-Flight Stabilizer

A second important application of the feedback loop is the stabilization of the ions' TOF. Despite large capacitors at the power supplies, fluctuations in electric fields can still occur, leading to a shifted TOF, further referred to as TOF drifts. While TOFControl has procedures to adapt its calibration to accommodate slow TOF shifts, they become critical for online, time-critical events like re-trapping.

Changing the analyzer electrode voltages to compensate for the TOF drifts is a simple approach to stabilize the TOF. The resulting change in the flight path leads to a well-defined relative shift in TOF depending on the relative shift in potential. Table 4.1 lists the relative TOF shifts and changes in the ion optical aberrations for a given change in each voltage for the eight analyzer electrodes, excluding the drift tube E5.

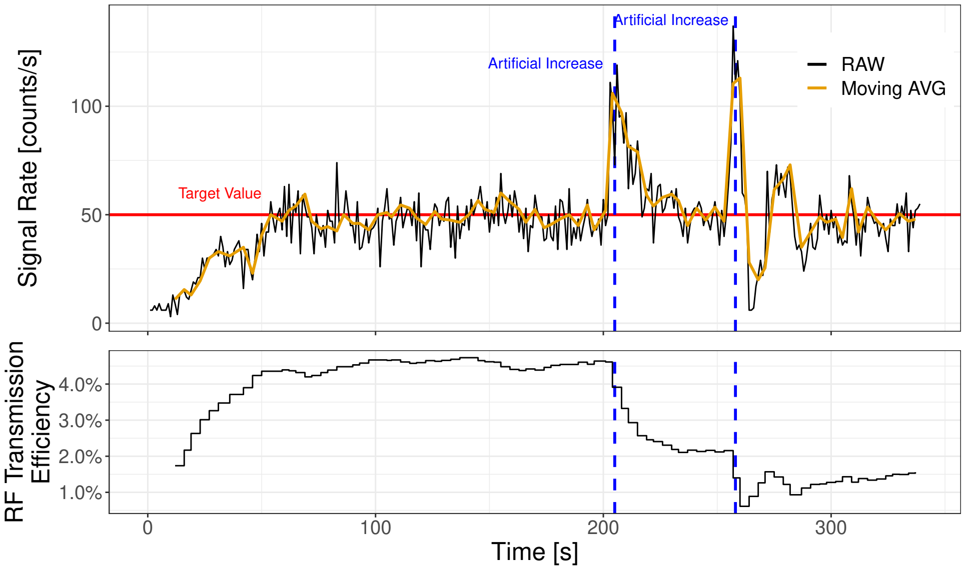

Figure 4.5.1: FSS regulation of signal rate by modifying the IG transmission gate (see Section 3.4). A calibrant ion at 322 u from the Agilent tuning mix is used in this measurement. Top: Raw data and the moving average used to compare with the target value of 50 counts/s. Bottom: Adjusted transmission efficiency of the transmission control RFQ RF.

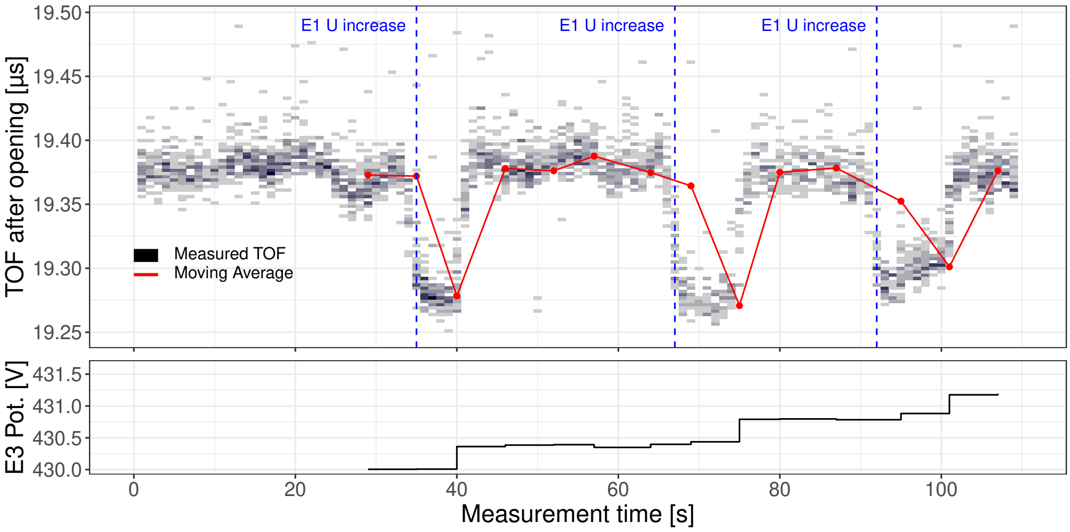

Figure 4.5.2: FSS correction of TOF by adapting the potential of electrode E3. E1 is artificially changed to create shifts that the FSS algorithm corrects automatically. The shown signal is a measurement of mass 322 u of the Agilent tuning mix.
Top: Raw data of peak position during the measurement are black. TOF refers to the opening of the analyzer. The red line is the moving average observables for the FSS. Blue marks indicate artificial E1 change.
Bottom: Potential of electrode E3 changed by the FSS.

Table 4.1: Relative values for 0.1 % simulated voltage change from [M. I. Yavor 2010]. $(\mathrm{T}|\delta)\delta$ and $(\mathrm{T}|\delta\delta)\delta^2$ refer to the first and second order of aberration in kinetic energy, $(\mathrm{T}|\mathrm{xx})\mathrm{x}^2$ to the second order in position.

Electrode		E1/9	E2/8	E3/7	E4/6
Rel. TOF shift		$-2.8 \cdot 10^{-4}$	$-1.6 \cdot 10^{-4}$	$1.3 \cdot 10^{-5}$	$-6.7 \cdot 10^{-5}$
$(\mathrm{T}\|\delta)\delta$	[ns]	$-1.8 \cdot 10^{-3}$	$1.7 \cdot 10^{-3}$	$2.6 \cdot 10^{-5}$	$5.1 \cdot 10^{-5}$
$(\mathrm{T}\|\mathrm{xx})\mathrm{x}^2$	[ns]	$1.2 \cdot 10^{-4}$	$-1.3 \cdot 10^{-4}$	$-3.0 \cdot 10^{-6}$	$-4.5 \cdot 10^{-5}$
$(\mathrm{T}\|\delta\delta)\delta^2$	[ns]	$-2.7 \cdot 10^{-5}$	$3.1 \cdot 10^{-5}$	$-5.1 \cdot 10^{-6}$	$2.0 \cdot 10^{-6}$

Figure 4.5.2 shows a proof-of-principle measurement where the FSS corrected a TOF shift artificially introduced by changing the analyzer E1 potential by 50 mV (0.003 %). In this example, the ion of 322 u from the Agilent tuning mix had a flight time of 10.645 ms. The introduced shift of 110 ns is corrected by adapting E3 by 0.4 V within 7 s. The stabilization Equation (4.5.1) used $a = -46.2681$ with $Q = U_{E_3}$ and I being the total TOF using a Gaussian fit to the mass peak in the spectrum.

Two electrodes with opposing aberration effects can be used to avoid introducing additional aberrations when correcting the TOF. The notation

$$(T|xx)_{\mathrm{E3}} = [(\partial^2 T(z)/\partial x_0^2)/2]_{\mathrm{E3}} \tag{4.5.2.1}$$

refers to the aberration expansion of T (time-of-flight deviation) regarding the second term of the Taylor series in terms of partial derivatives with respect to its position (x) for Electrode 3. The deviation of the ion's kinetic energy is referred to as δ (same notation as in [M. Yavor 2009]). By minimizing the quadratic sum of introduced aberrations of E3 and E4

$$\begin{aligned}\sigma_{\mathrm{E3,E4}} =& \left(a_{\mathrm{E3}} \cdot (T|\delta)\delta_{\mathrm{E3}}\right)^2 + \left(a_{\mathrm{E3}} \cdot (T|\delta\delta)\delta_{\mathrm{E3}}^2\right)^2 + \left(a_{\mathrm{E3}} \cdot (T|xx)x_{\mathrm{E3}}^2\right)^2 \\ &+ \left(a_{\mathrm{E4}} \cdot (T|\delta)\delta_{\mathrm{E4}}\right)^2 + \left(a_{\mathrm{E4}} \cdot (T|\delta\delta)\delta_{\mathrm{E4}}^2\right)^2 + \left(a_{\mathrm{E4}} \cdot (T|xx)x_{\mathrm{E4}}^2\right)^2\end{aligned} \tag{4.5.2.2}$$

regarding the relative change in TOF

$$((T|\delta)\delta)_{\mathrm{E3,E4}} = a_{\mathrm{E3}} \cdot ((T|\delta)\delta)_{\mathrm{E3}} + a_{\mathrm{E4}} \cdot ((T|\delta)\delta)_{\mathrm{E4}}, \tag{4.5.2.3}$$

one can find a fraction of the weights

$$c_{\mathrm{E3,E4}} = \frac{a_{\mathrm{E3}}}{a_{\mathrm{E4}}} \tag{4.5.2.4}$$

to correct the relative TOF shift Δt by

$$U_{\mathrm{E4,new}} = a_{\mathrm{E4}} \cdot \Delta t \cdot (U_{\mathrm{E4,old}} - e) + U_{\mathrm{E4,old}} \tag{4.5.2.5}$$

$$U_{\mathrm{E3,new}} = c \cdot \Delta t \cdot (U_{\mathrm{E3,old}} - e) + U_{\mathrm{E3,old}} \tag{4.5.2.6}$$

with U being the voltage applied to the corresponding electrode during isochronous turns.

Minimizing the square sum in Equation (4.5.2.2) with the values listed in Table 4.1 results in $c_{3,4} = 2.175$. This factor can be combined with the listed TOF influence to calculate $a_{\mathrm{E3}} = 39.22$ and $a_{\mathrm{E4}} = -18.03$. Aside from $e = 1300$ V due to the drift potential, all other weights in Equation (4.5.1) are set to zero.

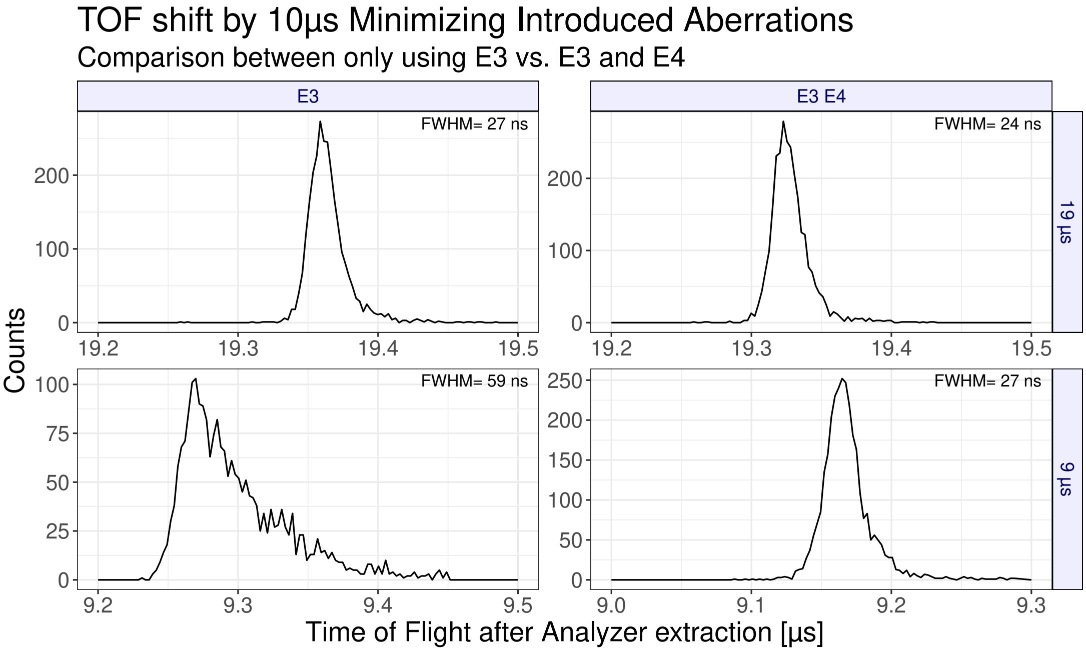

Figure 4.5.3: Comparison of different TOF stabilization methods using only E3 (left column) or E3 and E4 simultaneously (right column). The shown signal is a measurement of mass 322 u of the Agilent tuning mix. The original TOF (top row) is reduced by 10 µs corresponding to a change of 0.1 % (bottom row). The displayed TOF corresponds to the TOF after opening the analyzer. Both methods can shift the TOF by the expected difference. However, the stabilization using only electrode E3 increases the FWHM by 119 % due to introduced ion optical aberrations. Stabilizing the TOF using both electrodes introduced no significant increase in FWHM.

An artificial shift in TOF of mass 322 u of the Agilent tuning mix by 10 µs (0.1 %) was introduced to demonstrate the increase in ion optical aberrations in the plot shown in Figure 4.5.3. The plot compares realizing the shift with only the electrode E3 to using electrodes E3 and E4 with the previously mentioned weight fraction $c_{\mathrm{E3,E4}}$. Using only E3 leads to a strongly deformed signal shape and halves the acquired MRP. Correcting the TOF with both electrodes maintains most of its signal shape and FWHM.

The effect on realistic drift effects is demonstrated in Figure 4.5.4. The TOF of mass 322 u of the Agilent tuning mix is measured for a duration of 1000 s with different stabilization methods (No stabilization, only electrode E3, or both electrodes E3 and E4) at a total TOF of 10.645 ms. Both stabilization methods prevented more significant drift effects, while the stabilization using E3 and E4 proved to be more robust against short-time shifts due to technical reasons (for example, power supply precision and voltage ramp times). The plot also compares the signal shapes of the TRC correction, which is applied after acquisition and excels at correcting quick drift effects. While all stabilization techniques can not reach the MRP achieved by the TRC correction, its signal shape clarifies the increase in ion optical aberrations. The TRC-corrected MRP of the stabilization method using both electrodes is comparable to the TRC-corrected one. In contrast, the MRP of the stabilization using only electrode E3 is 26 % worse.

4.6 Peak Identification in TOFControl

The peak identification procedures in TOFControl aim to determine an ion's turn number and suggest its molecular composition based on its mass excess. The turn number can be ambiguous, especially in convoluted spectra with a broad mass range.

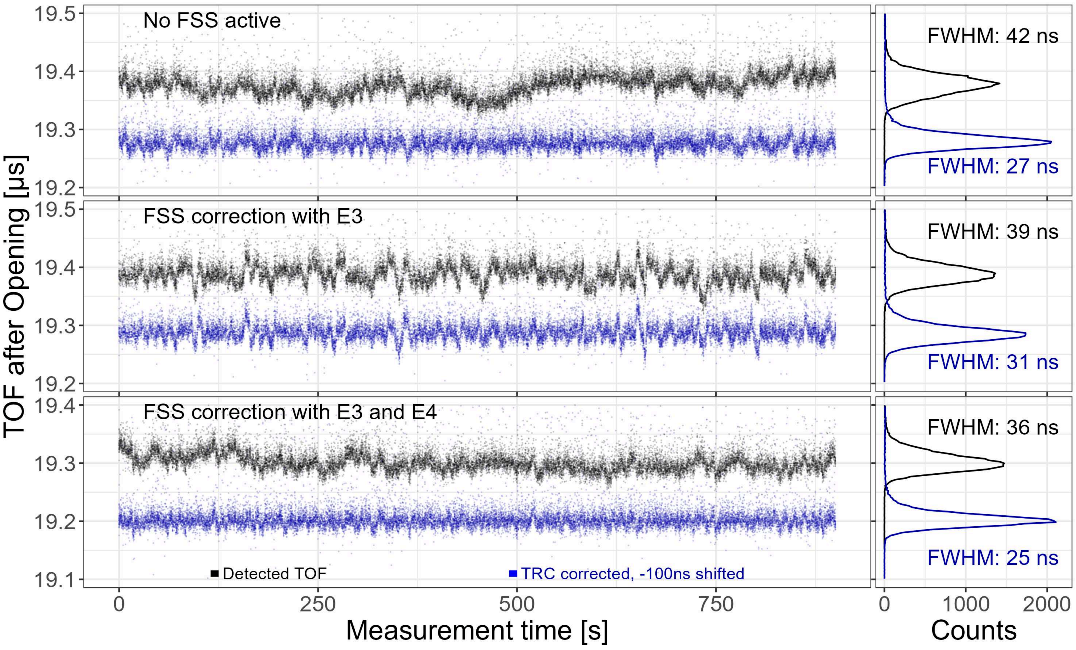

Figure 4.5.4: Comparison of different methods to stabilize the TOF during realistic conditions. A measurement of mass 322 u of the Agilent tuning mix is stabilized for a duration of 1000 s without artificial external influence. The left side shows a heatmap of the detected TOF signal while the right side shows a projection toward the TOF axis. Each row corresponds to a stabilization method. TRC corrected data is and projections are given colored in blue.
Top: No stabilization; Middle: Stabilized using only electrode E3; Bottom: Stabilized using electrode E3 and E4.
Both stabilization methods show a reduction in FWHM (7 - 14 %), but the TRC-corrected data reveals introduced ion optical aberrations when only using electrode E3. After TRC correction, the stabilization method using both electrodes achieves a slightly reduced FWHM as the unstabilized data.

The TOFControl software compares the estimated mass for each signal from Equation (2.6.2.5) for a range of possible turns with a list of candidates to identify the turn number. These candidates can be supplied directly or calculated by formula or by meeting molecular composition requirements like abundance, element, or half-life. Composition requirements also allow TOFControl to limit candidates to contain only fragments of a dissociated precursor molecule, given its elemental composition. Due to the sophisticated algorithm generating the list of candidates to compare against, execution typically requires only a few seconds. Once the mass difference between the candidate and a signal's mass at a particular turn falls below a given threshold, TOFControl marks a candidate as a *suggested molecule.*

Figure 4.6.1 shows the results of the peak identification algorithm. Information for each suggested molecule includes the natural abundance, detected intensity, turn number, deviation from literature mass, and a check of four of the seven *golden chemical rules* described in [Kind et al. 2007] indicating molecular stability. Additional features include an isotope pattern generator to estimate resolved isotopes, spectrum contamination with unexpected molecules, and import/export features to work with external software.

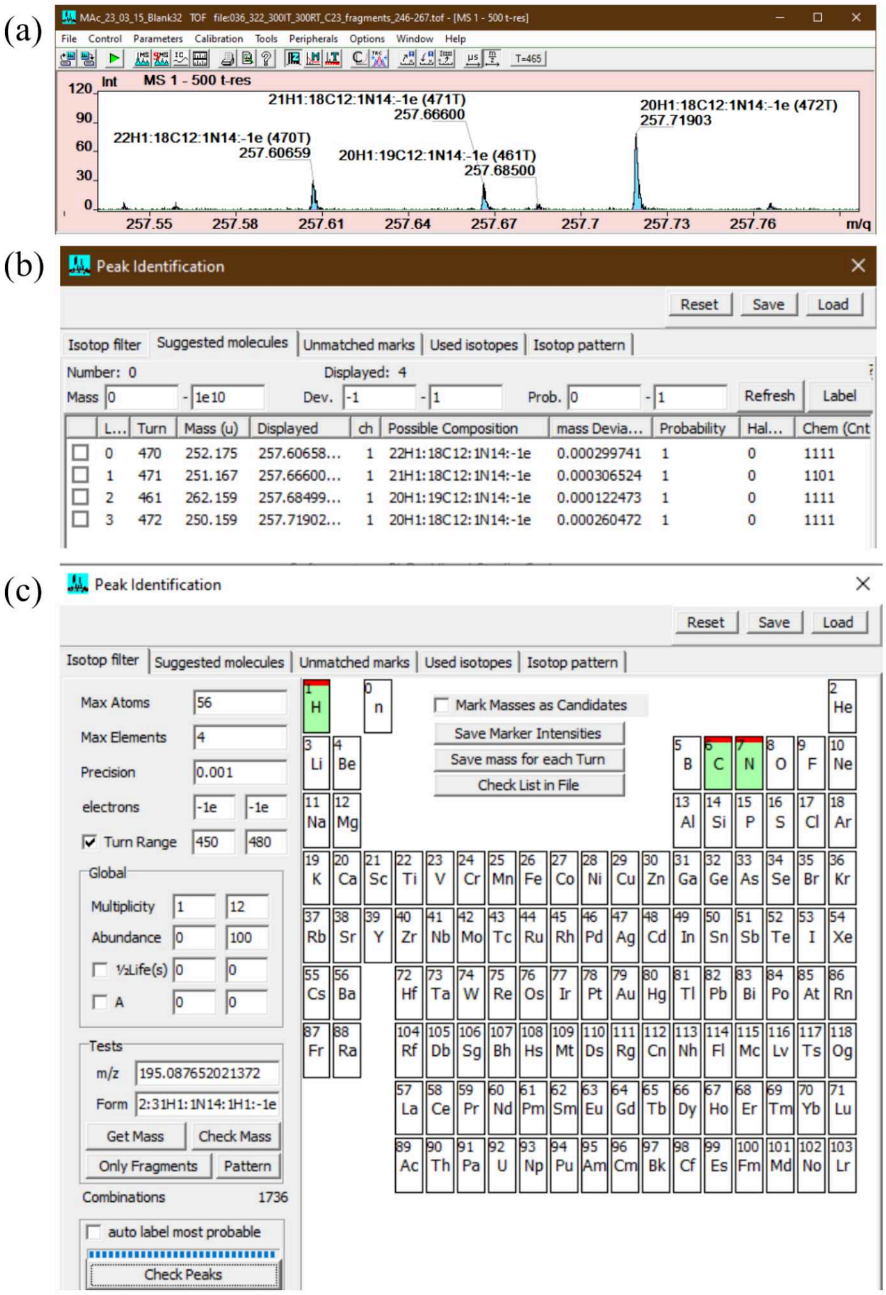

Number: 0
Displayed: 4
Mass 0 - 1e10
Dev. -1 - 1
Prob. 0 - 1

	L...	Turn	Mass (u)	Displayed	ch	Possible Composition	mass Devia...	Probability	Hal...	Chem (Cnt
☐	0	470	252.175	257.60658...	1	22H1:18C12:1N14:-1e	0.000299741	1	0	1111
☐	1	471	251.167	257.66600...	1	21H1:18C12:1N14:-1e	0.000306524	1	0	1101
☐	2	461	262.159	257.68499...	1	20H1:19C12:1N14:-1e	0.000122473	1	0	1111
☐	3	472	250.159	257.71902...	1	20H1:18C12:1N14:-1e	0.000260472	1	0	1111

Max Atoms 56
Max Elements 4
Precision 0.001
electrons -1e -1e
☑ Turn Range 450 480

Global
Multiplicity 1 12
Abundance 0 100
☐ ½Life(s) 0 0
☐ A 0 0

Tests
m/z 195.087652021372
Form 2:31H1:1N14:1H1:-1e

Combinations 1736

☐ auto label most probable

☐ Mark Masses as Candidates

Figure 4.6.1: Screenshot of TOFControl's peak identification feature.
(a) shows a calibrated mass spectrum with an ambiguous turn range. Four mass lines are labeled without prior knowledge of the turn number and, thus, the mass-to-charge ratio value. The peak identification later adds information about the turn number and the elemental composition.
(b) shows the suggested molecules of the peak identification for the labeled mass lines. Their position in the current spectrum mass axis, identified turn number, suggested elemental composition, mass deviation, isotopic ratio, and half-life are given in a table. The last column checks for the elemental composition's chemical consistency. Entries can be exported into a text file or marked inside the spectrum.
(c) depicts the user interface to operate the peak identification. Different filters like the range of turn number, a maximum for the number of atoms, a precursor molecule, and maximum mass deviation can be set on the left side. Additional filters for allowed elements, half-lives, and abundance ratios can be set on the right side. The feature also allows different automatic comparison and export features with the buttons at the top.

4.7 Spectrum Patching

Achieving high resolution and precise mass-to-charge ratio values with a time-of-flight mass spectrometer requires a long flight time and, thus, a higher number of turns (Equation (2.6.1.6)). However, lighter ions with the same kinetic energy fly faster, passing more turns than heavier ions when the exit mirror is opened. Since the TOF of a detected signal can be assigned to different turn numbers, the mass range of the resulting mass spectrum becomes ambiguous.

In order to avoid identification issues by ambiguous turn numbers and still measure with a high MRP, the mass range can be limited to ions belonging to a single turn number. In this *unambiguous mass range*, we can avoid misidentification and overlapping signals of ions with different turn numbers. While this approach is easy to set up and analyze, the *unambiguous mass range* shrinks as the number of turns increases to reach a higher MRP.

Spectrum patching scans a larger mass range in steps of the unambiguous mass range. While the resulting spectra can be exported and merged with simple data analysis tools, two significant problems arise from the technique's scanning nature. Since each set requires time to change settings and gather statistics, each iteration is prone to distortions due to changes in ion production rate or voltage drifts.

The ion production rate's fluctuations change the merged spectrum's composition. This fluctuation leads to a distortion in the patched spectrum that can change ion ratio compared to each other. This effect can be avoided by close supervision and adjustment of the ion source or compensated by scaling. *Scaling* refers to normalizing the detected count rate for each ion inside an iteration to a reference value. This value can be an overlapping mass region of the previous iteration or a section of a reference spectrum with a lower MRP but a larger unambiguous mass range.

Voltage fluctuations lead to a change in the TOF, which requires adjustments to the re-trapping time and spectrum calibration. While the re-trapping time needs to be adjusted online, calibration can be performed after the measurement. However, calibrants need to be added to the spectrum, periodically or permanently, and measurement settings adjusted to focus on the calibrants.

A script written in R, a free software environment for statistical computing and graphics, merges the spectra and applies the described scaling and re-calibration techniques. The spectra acquired by scanning the mass range in TOFControl are exported and used as input for the R script. The script then generates a plot and a histogram which can be imported into TOFControl for further analysis. This technique is applied in Section 6.2.2 to analyze data on the crude oil residue sample within 200 - 600 u.

4.8 Deconvoluting Broad-Band High-Resolution Spectra

With longer measurement times, the setup becomes more prone to fluctuations in the ion source production rate and supplied voltages, resulting in a loss in mass-to-charge ratio value precision. Attempts of rescaling mass range in overlapping areas and intermediate re-calibration, as described in Section 4.7, proved error-prone and complicated analysis. Instead, multiple unambiguous mass ranges can be recorded simultaneously to reduce measurement time to mitigate instability effects while ensuring high MRP. A three-stage procedure has been developed and implemented to acquire the final data of this work shown in Section 6.2.5.

In the first step, a low-resolution spectrum (MRP of $m/\Delta m = 3000$, precision of $\delta m/m = 50\,\text{ppm}$) with a wide unambiguous mass range is acquired to obtain an overview and to acquire the ratios between ion rates. This mass range is then divided into groups of 20 ion species.

The second step consists of unambiguous mass range measurements for each group at a higher turn number to increase the MRP. This step verifies the MRS setting and procures mass-to-charge ratio values with enough precision ($m/\Delta m = 10\,000$, $\delta m/m = 20\,\text{ppm}$) to prepare the final measurement. Preparation must ensure that ion signals of different turn numbers do not overlap and that no ion species is inside the exit mirror while it opens and thus lost to detection.

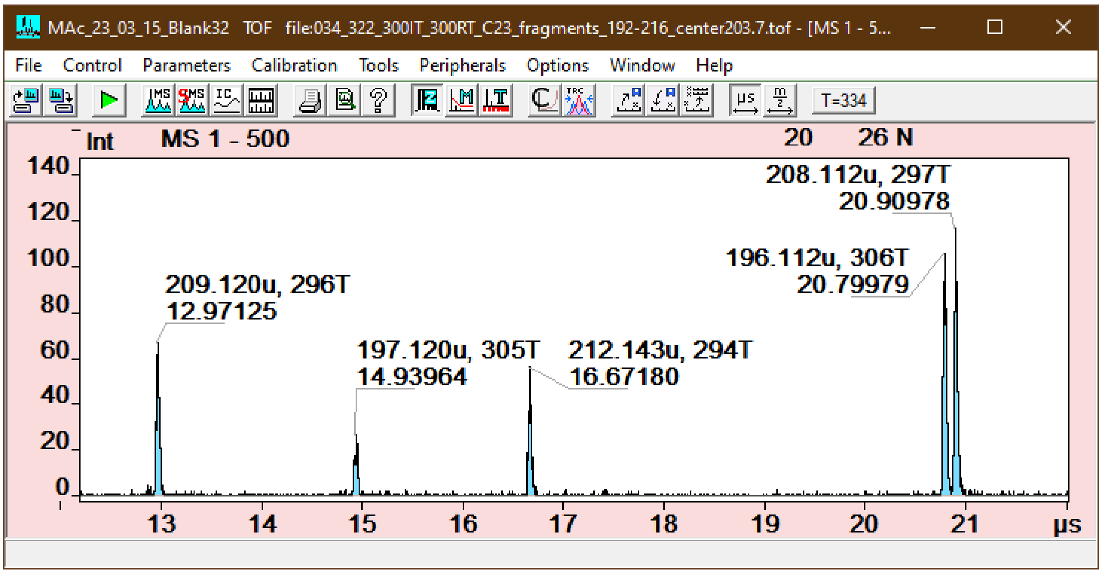

Figure 4.8.1: Section of a high-resolution spectrum taken in the third stage of the turn deconvolution procedure. The spectrum shows some of the CID fragments of $C_{23}H_{32}N^+$ in the mass range of 192 - 216 u. Each peak is labeled with its mass-to-charge ratio value, turn number, and measured TOF after the exit mirror was opened, which is also displayed on the abscissa.

The third step acquires a high resolution spectrum ($m/\Delta m = 170\,000$, $\delta m/m = 2\,\text{ppm}$) for each group. Typically the measured mass range comprises 10 - 20 unambiguous mass ranges, each with its turn number. Their TOF value is compared to estimations for the mass-to-charge ratio values acquired during the second stage to assign the correct turn number to each signal. Figure 4.8.1 shows an example of $C_{23}H_{32}N^+$ fragments between 192 - 216 u. Except for the precursor signal at 238 IT, turn numbers range between 294 - 307, and thus there are 14 unambiguous mass ranges.

An R script has been written to predict the spectrum compositions and estimate the best settings for a set of expected mass-to-charge ratio values. The script calculates the TOF to the detector for a given list of mass-to-charge ratio values and a range of timespans from injection into the analyzer to the opening of the exit mirror (*start time*). The plot lists the 20 best start time settings and the corresponding distributions in the time-of-flight spectrum. Settings that lead to ions being detected too close to each other to be resolved or ions being affected by the exit mirror opening are graded lower. In addition, the script offers information about each ion's number of turns and how to set the start time using the trigger system. Figure 4.8.2 shows an example of a list of 15 molecules within 177 - 195 u to be separated by at least 30 ns from each other for start times between 9.9 - 10.1 ms, reaching an MRP of around 200 000.

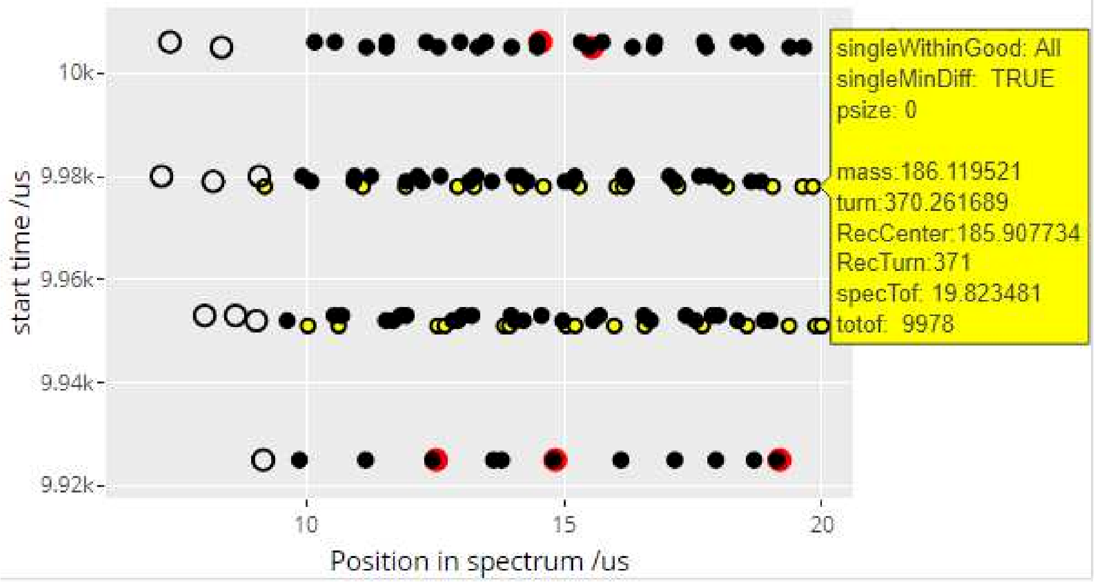

singleWithinGood: All
singleMinDiff: TRUE
psize: 0

mass:186.119521
turn:370.261689
RecCenter:185.907734
RecTurn:371
specTof: 19.823481
totof: 9978

Figure 4.8.2: Screenshot of the script output for predicting the position of 15 ion species for different analyzer closing durations. Each point corresponds to an ion's TOF. Points with the same start time correspond to the same timing sequence setting. Each row of points is thus comparable to a mass spectrum acquired using the same setting.
Red points mark the ion signals that are closer than 30 ns to the next ion signal. Empty points are inside the exit mirror while it opens and thus lost to detection or have a distorted TOF. Yellow points belong to settings where there are no issues.
The yellow box appears when moving the cursor over a point and shows information containing the mass-to-charge ratio value, turn number and parameter of the used timing sequence information. The currently selected point corresponds to a setting where the analyzer is closed for 9978 µs, which can be achieved by changing the setting to let a fictional ion with a mass-to-charge ratio value of 185.908 u fly for 371 turns.

While this procedure does not produce a single, deconvoluted spectrum, combining the results of the first and third stages gives a list of precise mass-to-charge ratio values and intensities that are easy to calibrate and resistant to fluctuations in ion source production rate.

4.9 Mass Range Selection

The mass range selector described in Section 2.6.4 can restrict the analyzer transmission to two selected mass ranges. Its deflection pulse number, phase, duration, and frequency can be directly controlled using the trigger system software (see Section 4.3). However, estimating these operating parameters' exact effects on mass transmission can be difficult. The R-based *MRS script* has been written to predict the effects of the MRS deflection and the switching of the analyzer electrode voltages. The MRS script serves three primary purposes that help operators set up a measurement with the TOFControl software and the MR-TOF-MS, as shown in Figure 4.9.1.

The first feature calculates and displays the MRS settings to allow the ions of up to two independent mass ranges to pass to the detector using the theory described in Section 2.6.4. The script can accurately determine the MRS deflection effects using reference TOF values of $^{133}\mathrm{Cs}^{+}$, like the time required to pass one turn. The graphical user interface visualizes the effective mass range and effects of fringe fields and the required settings. Resulting deflection pulse widths are calculated and displayed to

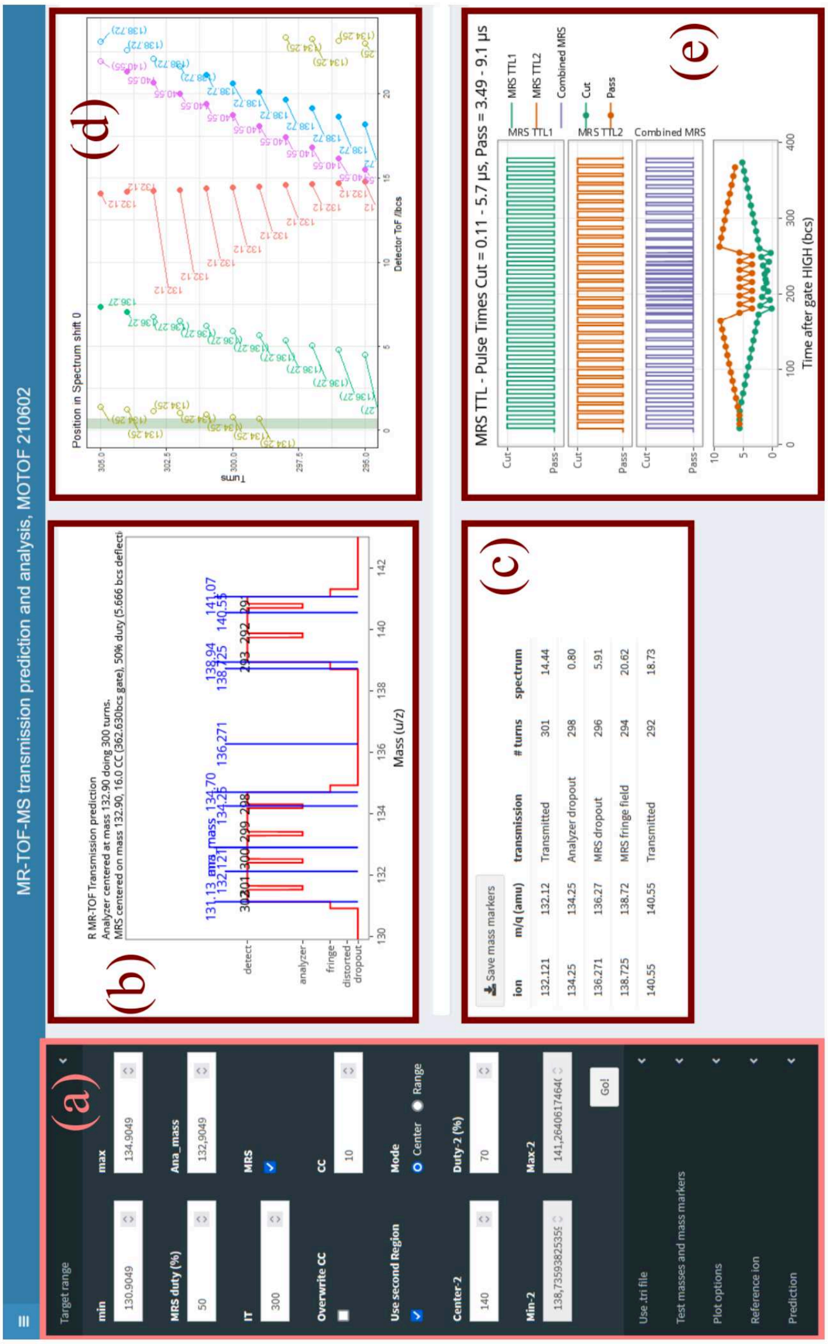

min: 130,9049
max: 134,9049
MRS duty (%): 50
Ana_mass: 132,9049
IT: 300
MRS: ☑
Overwrite CC: ☐
CC: 10
Use second Region: ☑
Mode: ● Center ○ Range
Center-2: 140
Duty-2 (%): 70
Min-2: 138,7359382535
Max-2: 141,26406174640

R MR-TOF Transmission prediction
Analyzer centered at mass 132.90 doing 300 turns.
MRS centered on mass 132.90, 16.0 CC (362.630bcs gate), 50% duty (5.666 bcs deflecti

ion	m/q (amu)	transmission	# turns	spectrum
132.121	132.12	Transmitted	301	14.44
134.25	134.25	Analyzer dropout	298	0.80
136.271	136.27	MRS dropout	296	5.91
138.725	138.72	MRS fringe field	294	20.62
140.55	140.55	Transmitted	292	18.73

Figure 4.9.1: Graphical User Interface (turned left) as shown in the web browser Firefox of the mass range selector R Script.
(a) marks a sidebar where user settings can be entered. **(b)** shows the influence of the MRS and analyzer on the mass range. A given list of ion species is plotted as blue lines. The height of the red line refers to the transmission state of the corresponding mass. The *detect* level indicates transmission, while the *dropout* level indicates a deflection by the MRS. The *analyzer* level marks ions inside the exit mirror while it is opened. The *fringe* level indicates that ions were affected but not completely deflected by the MRS in their last pass. The *distorted* level is assumed for ions inside a mirror while it switched from time focus shift to isochronous mode. **(c)** shows a table of expected turn numbers, spectrum positions, and transmission states for each ion species. **(d)** shows the expected position in the spectrum (abscissa) and several changed settings to find the desired setting. **(e)**shows the applied dipole pulses for each mass range, the combined signal applied to the electrode, and a plot of pulse widths for diagnostics.

ensure the setting is feasible concerning hardware limitations.

The script first populates an array, where each bin represents the checked mass range in steps of 1 mu, with a value representing a transmission state. For each turn in which the MRS deflects, the relative position in the analyzer for each mass bin is calculated in fractional turns (e.g., after 9.7 turns, the relative position is 0.7). The relative turn position is compared to the relative transmission phase of the MRS. For example, with 12 µs deflecting and 14 µs transmitting, the relative transmission phase is 54 % centered around an ion that requires 26 µs for half a turn. If the relative turn position is outside the transmission phase, the array at the corresponding bin position is set to a value representing a state of being deflected.

The second main feature of the script calculates the mass ranges lost to detection due to opening the exit mirror. When the exit mirror is opened, any ion close to the exit mirror experiences the switching field and does not reach the detector. The region affected by the exit mirror spans around 15 % of the flight path ions take for one turn. The script calculates the relative turn position for each mass bin in the previously mentioned array for the last turn and compares it to the region affected by the exit mirror. The bin-value of masses inside this region is then set to a value representing being lost due to the exit mirror.

Spectrum population prediction is the third main feature of the script. The relative turn number for a given list of mass-to-charge ratio values is calculated when the analyzer is opened. Their position in the spectrum can be calculated by scaling the reference values of $^{133}\text{Cs}^{+}$ for the TOF per turn and the TOF from the analyzer's center to the detector. The script can repeat this calculation for various turn numbers to let the user determine the best setting for measuring all masses in the given list.

An operator can specify one or two desired mass ranges, the deflection duration, and the analyzer setting or supply a setting file from the trigger system software (Figure 4.9.1). A list of *test masses* can also be provided, by mass-to-charge ratio value, elemental composition, or a text file from the TOFControl software, to check for transmission or to predict optimal transmission settings. Script execution results in a table indicating the test mass transmission, a plot showing the calculated MRS settings and effects on a given mass range, a plot regarding spectrum prediction, and a plot of the TTL pulse widths. This R script can be accessed locally or remotely in all common web browsers, and operating does not require any programming knowledge.

4.9.1 Mass Selection Sequence

The mass range selector uses a precisely timed deflection field at the analyzer's center to isolate a desired mass range, as outlined in Section 2.6.4.

The trigger system allows the operator to choose the center of the transmitted mass range, the duration per turn, and the number of turns, during which the MRS is active. Up to two mass regions can be defined this way, and the trigger system accordingly applies the overlayed on-off pattern to the MRS.

The periodic deflection pulse signal is generated with a fixed duty cycle and frequency for each region and gated with a given phase and duration. The chosen phase and frequency are determined by the ion of interest's mass-to-charge ratio to deflect ions only when the IOI ions are close to the entrance or exit mirror. The duty cycle and duration determine the transmitted mass range surrounding the IOI. Higher duty cycles reduce the mass range per deflection pulse more and, thus, can compensate for lower gate durations at the cost of precision.

A separate trigger system channel controls a separate high-voltage switch to correct the beam alignment, preceding the deflection while the IOI passes the MRS electrodes.

Figure 4.9.2 shows an example where the MRS is set up for ten turns with deflections for a singly-charged ion of mass 622 u, which revolves in the analyzer with 49 µs at 49 % deflection duty cycle. This setting produces a transmitted mass range of 609 - 636 u.

The switching electronics and the power supply stability restrict the maximum number and duty cycle of deflections. After these parameters exceed a specific value, the voltage levels of deflection and transmission converge for the tailing deflection pulses. The changed voltage levels have reduced deflection capabilities and tend to cause TOF shifts.

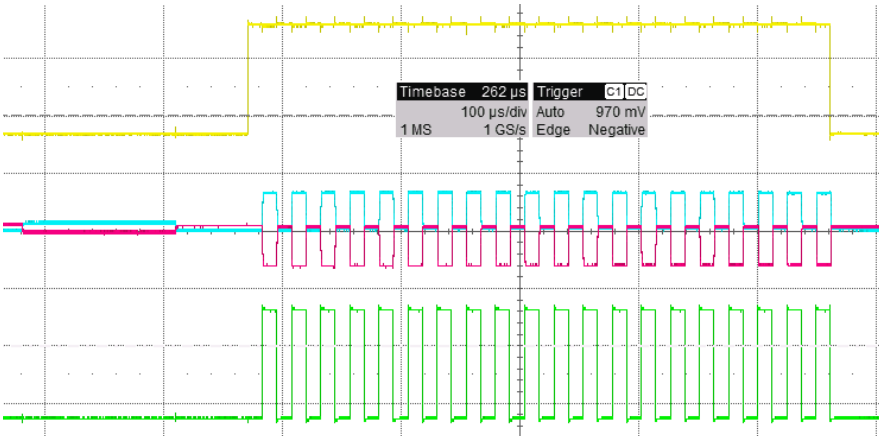

Timebase 262 µs
100 µs/div
1 MS 1 GS/s
Trigger C1 DC
Auto 970 mV
Edge Negative

Figure 4.9.2: Oscilloscope screenshot of the MRS deflection gate (yellow), the high-voltage switch inputs (green), and voltage applied to the dipole-electrodes (blue and red). A steering pulse for beam alignment precedes deflection pulses.

5 Performance Improvements

5.1 API Transmission

In addition to its ion source compatibility, the new API offers a high transmission efficiency for charged molecules while filtering out neutral molecules and light solvent ions.

A current meter with a negative bias of −70 V was connected to various electrodes inside the API to determine the ion current distribution inside the chamber. All other API electrodes were operated with their default voltages. The transmission efficiency is then determined by the ratio of the detected ion current at a fixed ion production rate.

The micro-ESI source described in Section 3.2.3 was operated at 2.6 kV with the Agilent tuning mix (G1969-85000), which consists of 90 % acetonitrile and includes isolated analytes listed in Table 5.1.

Mass	Formula
118.0863	$C_5H_{12}O_2N$
322.0481	$C_6H_{19}O_6N_3P_3$
622.0290	$C_{12}H_{19}O_6N_3F_{12}P_3$
922.0098	$C_{18}H_{19}O_6N_3F_{24}P_3$
1221.9906	$C_{24}H_{19}O_6N_3F_{36}P_3$

Table 5.1: Relevant molecules contained in Agilent tuning mix G1969-85000.

The detected ion current shown in Figure 5.1.1 represents the transmission efficiency of the ions through the new API. The gas flow carries 1.1 % of the ions through the inlet capillary compared to the current of ions impacting onto the surface on the outside. Once inside the chamber, 85 % of the ion current reaches the carpet surface, while 64 % is detected at the exit nozzle. Connecting all four transmission control RFQ rods to the electrometer, the transmission efficiency through the nozzle is measured as 10 %. The efficiency is likely reduced due to space charge effects and the dominance of charged solvent and buffer gas ions, which are less likely transported by the RF carpet. However, the measured current of 140 pA translated to $9 \cdot 10^9$ charged particles per second. In order to avoid space charge effects and digitizer dead time, it is intentionally decreased to typically 1 - 10 % by using the transmission control RFQ.

The transmission dependence on RF frequency and amplitude of the API carpet is shown in Figure 5.1.2 for $C_{23}H_{32}N^+$ at 322 u and caffeine at 195 u. The measured minimum RF amplitudes to transport the ions at 2 MHz RF frequency are listed with their mass-to-charge ratio values and reduced ion mobility in Table 5.2.

From Equation (2.5.4.8), the effective pushing field E_{eff} is proportional to the squared RF amplitude U_{RF}, the squared reduced ion mobility κ_0, and the mass-to-charge ratio value m:

$$E_{\text{eff}} \propto U_{\text{RF}}^2 \cdot \kappa_0^2 \cdot m \tag{5.1.1}$$

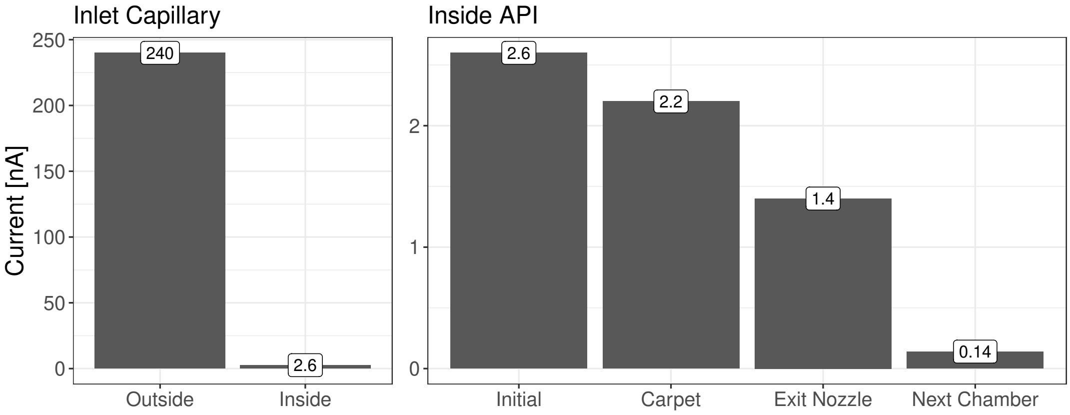

Figure 5.1.1: Transmission efficiency of the API. The current measured at various electrodes of the API is given in nA. The Agilent tuning mix was used with the micro-ESI source operated with a flow rate of 0.05 ml/h and an ionization potential of 2.8 kV. Each current measurement uses an attractive bias voltage of −70 V compared to the API electrode voltages. Left: Transmission efficiency from outside the chamber, measured on the outside surface, through the inlet capillary, measured at the API pushing plate.
Right: Transmission within the chamber and through the carpet exit nozzle. The initial current is measured at the pushing plate. The current at the RF carpet surface is measured by connecting all RF carpet rings to the current meter. Ions in the next chamber are measured at the transmission control RFQ.

Molecule	Mass	Solvent	Reduced ion Mobility	RF Amplitude Full Transmission
$C_{23}H_{32}N^+$	322.0 u	acetonitrile	1.33	45 V
Caffeine	195.1 u	MeOH+H_2O	1.59	50 V
Simulation	195.1 u	-	1.85	15 V

Table 5.2: Comparison of required RF amplitude at the RF carpet for full transport at 2 MHz for different ions. Measured values are extracted from the measurement shown in Figure 5.1.2. The simulated transmission of caffeine is shown in Figure 3.3.5. Mobility values are taken from [Jafari et al. 2011] (caffeine) or estimated from their travel time through the transmission control RFQ.

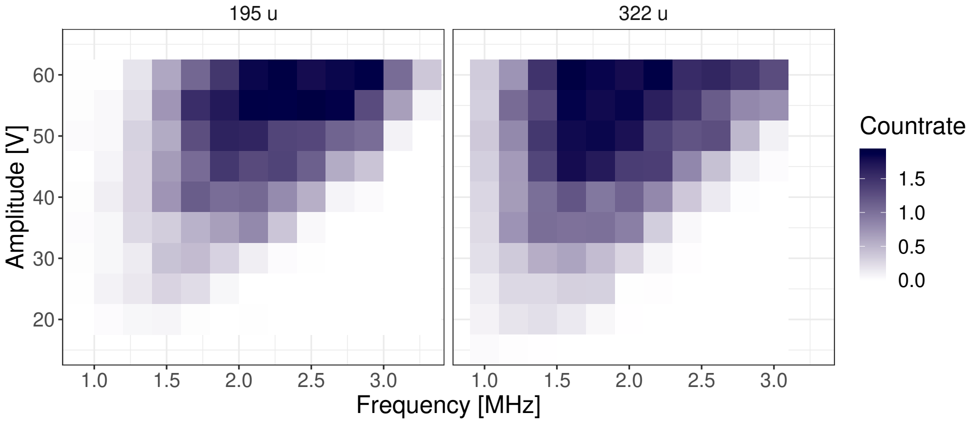

Figure 5.1.2: Measured transmission efficiency of singly charged ions of 195 u (caffeine) and 322 u (from Agilent tuning mix) for different RF frequency and amplitude settings of the RF carpet. Darker areas mean higher transmission efficiency to the detector. The Caffeine was solved in methanol and water at $10 \cdot 10^{-5}$ mole/l.

The experimentally found required RF amplitude for full transmission of caffeine molecules of 50 V translates to an RF amplitude of 46 V for the molecule at 322 u, which agrees with the measurement.

However, the measured RF amplitude differs for caffeine molecules from the simulation shown in Section 3.3.2, where an RF amplitude of 15 V is sufficient. This discrepancy is likely caused by a non-ideal signal shape of the used RF generator, disregarded buffer gas turbulences in the API chamber, and space-charge effects of charged solvent and buffer-gas ions that were neglected in the simulation.

5.2 Dual-Emitter Usage

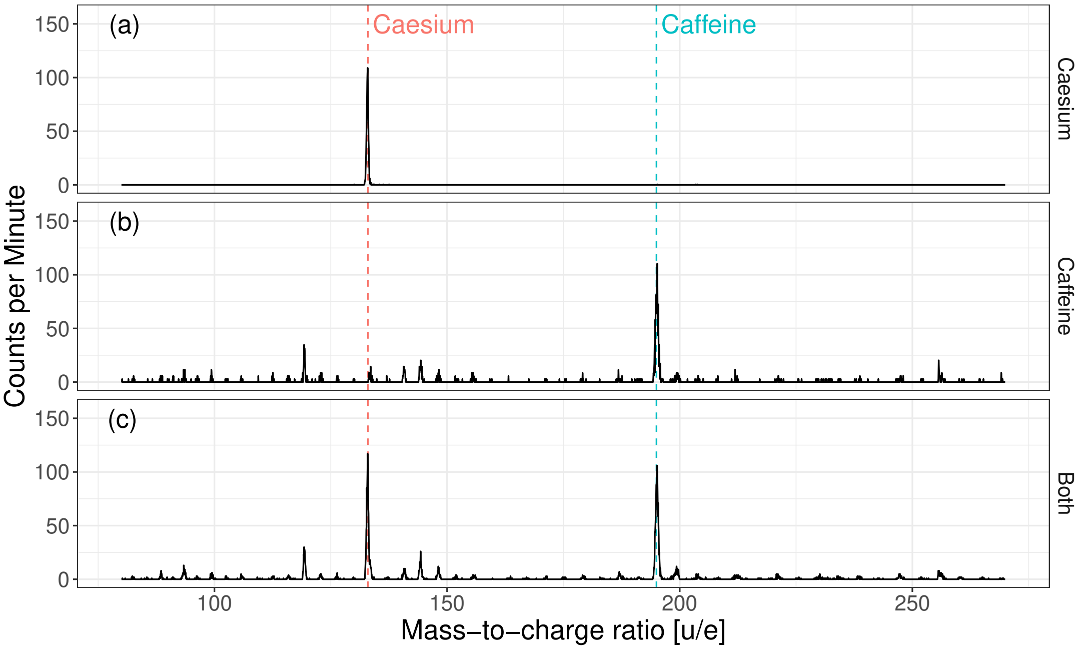

Figure 5.2.1: Comparison of two separately operated ion sources with the API. Each ion source was measured independently before being used in parallel. No interference between the sources regarding transmission suppression or chemical reactions was observed.
(a): Mass spectrum of thermal ^{133}Cs-source
(b): Mass spectrum of nano-ESI using Caffeine in MeOH and H_2O
(c): Mass spectrum obtained with both ion sources active.

The API features two inlet capillaries and a thermal ^{133}Cs source, which are operable in parallel for diagnostics or calibration purposes. To demonstrate this dual usage, a nano-ESI emitter was used with Caffeine (195.088 u) dissolved in Methanol and water with a concentration of $1 \cdot 10^{-4}$ mol/l. The emitter voltage and thermal heating were adapted such that both ion sources produce similar ion rates. The mass spectra shown in Figure 5.2.1 display the independent usage of the two ion sources. The comparison of the mass spectrum obtained with both ion sources (c) with the spectra recorded using only one source (a) and (b) shows no interference between the sources regarding transmission suppression or chemical reactions.

Since the device's application area in this work revolves around crude oil residues, contamination and cleanliness of the system are of significant concern. Figure 5.2.2 shows the cross-contamination behavior of the crude oil residue sample (meadium heavy crude oil, 250 ppm in MeOH + Toluene 1:1) with the Agilent tuning mix. Each solvent was introduced in a separate inlet and switched on and off consecutively.

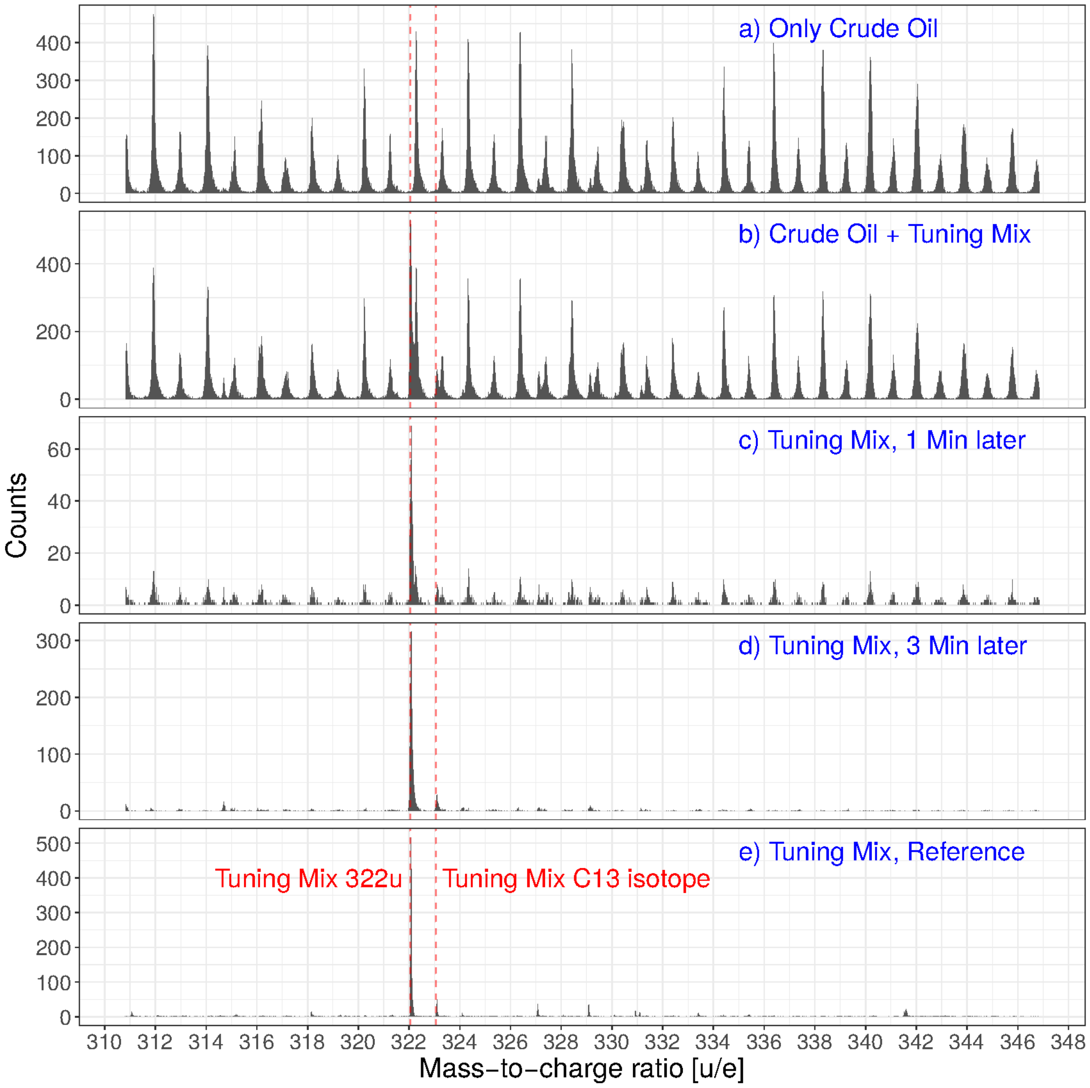

Figure 5.2.2: Parallel use of 2 inlets with two nano-ESI sources, one filled with Agilent tuning mix, the other with dissolved crude oil residue. The spectra shown from (a)-(d) follow chronological order. Reference ions of the Agilent tuning mix are marked in red. The spectrum of tuning mix is free of contaminants three minutes after the emitter with the crude oil sample is switched off.
(a): Only the emitter with the crude oil sample is switched on.
(b): The emitter with the Agilent tuning mix is switched on in addition.
(c): The emitter with the crude oil sample is switched off for one minute.
(d): The emitter with the crude oil sample is switched off for three minutes.
(e): Reference spectrum of the tuning mix, which was taken three hours prior to the other measurements.

The ion sources are operated as shown in Table 3.1. The first mass spectrum, labeled (a) in Figure 5.2.2, shows a spectrum of only the crude oil sample. Then the emitter with the Agilet tuning mix was switched on for two minutes in the spectrum (b). The emitter with the crude oil sample was switched off, and the contamination was observed after one minute (c) and three minutes (d). Spectrum (e) shows a reference spectrum of the Agilent tuning mix measured a few hours earlier. Remnants of the crude oil sample can still be observed in the spectrum (c). However, after three minutes, the spectrum composition is close to that of the reference spectrum, which proves the system's high resistance against short-term contamination effects.

While the system is resistant to short-term contamination, a memory effect proved to be an issue, where contaminants are accumulated over time. After a six-months-long period of regularly measuring crude oil samples (270 hours of exposure) using the nano-ESI source with settings according to Table 3.1, the mass spectrum of the Agilent tuning mix showed strong contamination effects (Figure 5.2.3(a)).

The chamber was disassembled for cleaning, and brown residues could be seen on the inlet capillary and jet disruptor (Figure 5.2.4(b)). The copper block was coated in a black layer of copper oxide, and cable isolation was partly melted because the cable had touched the heated copper block in Figure 5.2.4(a). Surfaces were wiped clean with isopropanol-drenched tissues, and the inlet capillary was cleaned using an ultrasonic bath filled with isopropanol. Including deconstruction and reassembling, the cleaning process required less than two hours. Afterward, a clean spectrum (Figure 5.2.3(b)) could be acquired again.

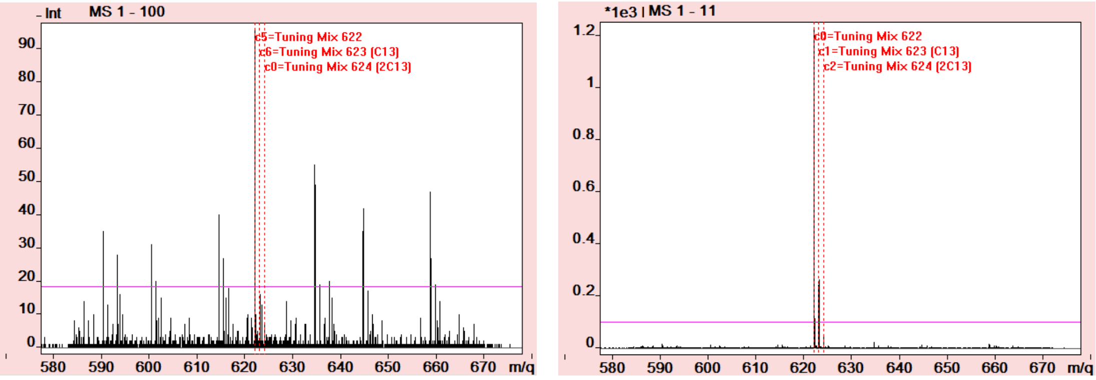

(a) Contamination with crude oil molecules

(b) After cleaning the API

Figure 5.2.3: Mass spectrum of Agilent tuning mix within the mass range of 580 - 670 u/e. Over six months, Long-term contamination effects from exposure to the crude oil sample were observed. The contamination vanishes after cleaning the API.

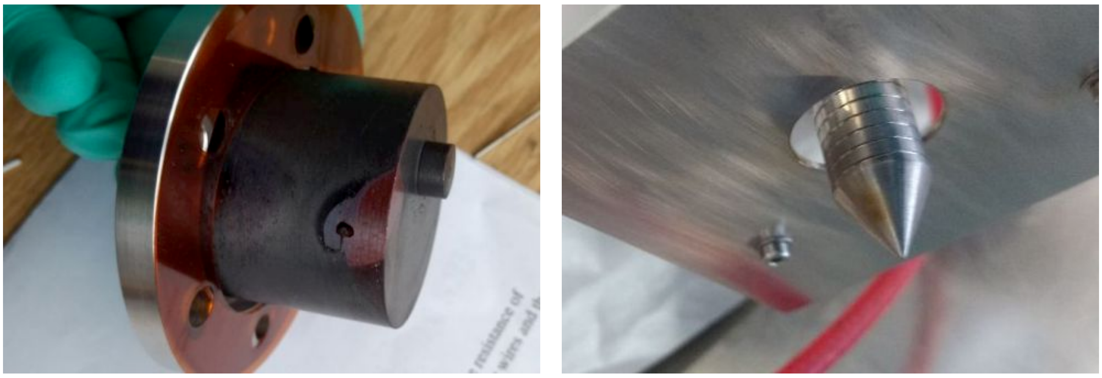

(a) Residue of burned cable isolation on the heated copper block inside API.

(b) Residue of crude oil sample on the Jet disruptor electrode inside API.

Figure 5.2.4: Visible API contaminations due to exposure to the crude oil sample solution over six months.

5.3 Detection Delay

The *detection delay* describes the time an ion travels from the ion source to the TOF detector. It can be subdivided into the *extraction time* required for the ion to travel through the API and the *transmission time* needed to pass through the beam preparation system and the analyzer. While the timing sequence dominates the transmission time, the extraction time is a property of the API and depends on electric field strength, gas flow, and ion mobility.

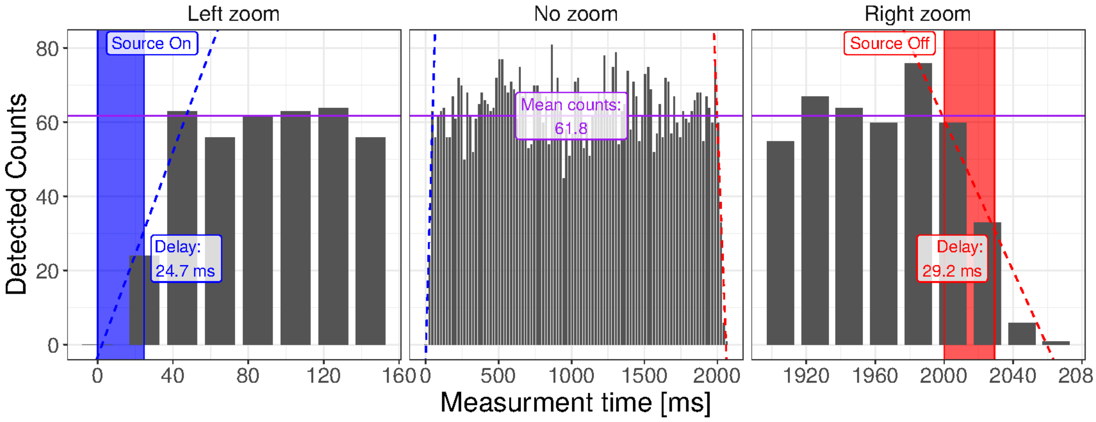

Figure 5.3.1: Output of the R script for the detection delay measurement with the thermal ^{133}Cs-source at a repetition rate of 50 Hz. The source was switched on for 2 s while a signal indicating the source state was given to a separate channel of the Digitizer. The abscissa shows the time after the source was switched on, while the ordinate depicts the number of detected ions. After a delay, the ion rate rises until a plateau is reached. A linear fit of the number of detected ions in this region yields the detection delay time of 24.7 ms, where half the plateau value is reached. At the end of the 2 s long spill of ions, the same method is used to obtain the time that ions are still extracted after the source is switched off (29.2 ms).

The detection delay was measured by operating the ion source in a pulsed fashion. Ion bunches were produced by switching the acceleration potential of the thermal ^{133}Cs source between blocking and transmitting using the trigger system. The TTL signal was then shared with the digitizer to obtain the time difference between the start of ion production and ion detection. The ^{133}Cs source was switched on for 2 s to obtain ion spills, as shown in Figure 5.3.1, where multiple spills were accumulated. It can be observed that after a delay, the number of detected ions quickly rises until a plateau is reached. A linear fit of the rising ion detection numbers at the start of the spill yields the value for the detection delay of 24.7 ms, where the detected counts reach half of the plateau. The same procedures can be used at the end of the spill to obtain the time ions are still seen after the source is switched off, which in this case is 29.2 ms. The low extraction and storage time proves the system's quick reaction time to changes in the ion sources.

The time required by the API to extract and transfer ions is measured in Figure 5.3.2. The thermal ^{133}Cs ion source and the RF carpet nozzle are operated so that the ions get only transported for 50 ms at a frequency of 10 Hz. The phase shift between both transmission windows is then varied, and the resulting rate of ^{133}Cs ions on the detector is observed. If the phase shift equals the time ions require to travel from the ion source to the nozzle, all ions within the 50 ms long production time should pass, resulting in a maximum detection rate. A Gaussian fit of the detected ion rate against the set phase shift yields a transmission time of the API of 0.5 ms, which agrees with ion trajectory

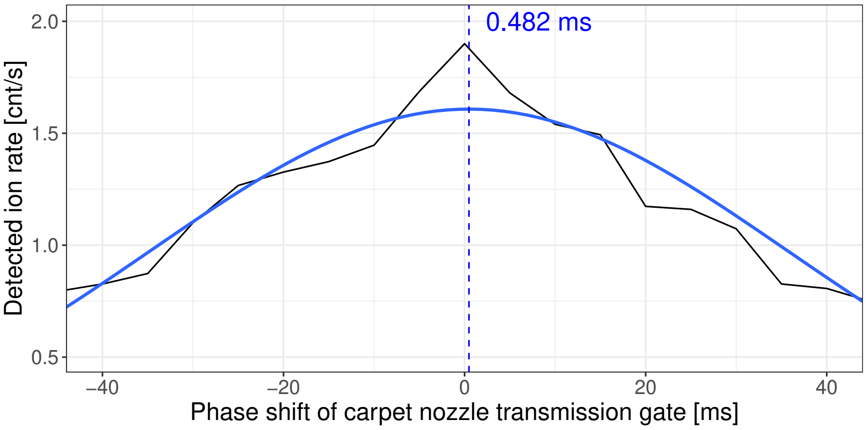

Figure 5.3.2: Measurement for transmission time inside the API. The thermal ^{133}Cs source and the RF carpet nozzle are set to transmit ions only for a duration of 50 ms at 10 Hz. The plot shows the dependence of the detected ion rate on the phase shift of the nozzle transmission window. At a phase shift below 1 ms, all ions of the source pass the nozzle transmission window and reach the detector.

simulations. This result proves the API extraction to be very fast and even suitable for time-critical reaction measurements.

5.4 Characterisation

The system features characteristics that are outstanding in their combination. As mentioned in [Lippert 2016], the device features an MRP of up to 300 000 at mass 322 u, a detection limit down to $1 \cdot 10^{-9}$ mol/l, a linear dynamic range of 5 orders of magnitude, and a mass accuracy of 0.3 ppm. This chapter presents further details on the device behavior in a broader field of application.

5.4.1 Mass Resolving Power

Following Section 2.6.1, the device's mass resolving power (MRP) is limited by the initial turn-around time, the introduced aberrations, and the flight path length, which is proportional to the turn number. While there is no theoretical limit on the turn number, the repetition cycle dictates a technical limitation for the TOF. This maximum TOF results in a mass-dependent limitation of the turn number, which is inversely proportional to $\sqrt{m/q}$.

The measured dependence of the MRP and transmission efficiency through the analyzer on mass and turn number is shown in Figure 5.4.1. In this work, the device is typically operated at a 25 Hz repetition rate, limiting the total TOF to 20 ms.

With an increasing number of turns, the MRP increases, as demonstrated by the following measurements of molecules from the Agilent tuning mix. The device quickly reaches an MRP of 200 000 for ions of 118 u after 200 IT, reaching up to 270 000 after 600 IT on average. The MRP is mass-independent for a given turn number, i.e., path length. However, an ion of 922 u can only reach a turn number high enough for an MRP of 150 000 in 20 ms. The transmission efficiency through the analyzer follows an exponential decay. Still, it stays above 50 % for the molecules of 118.322 u and above 30 % for the molecules of 622.922 u after a TOF of 20 ms.

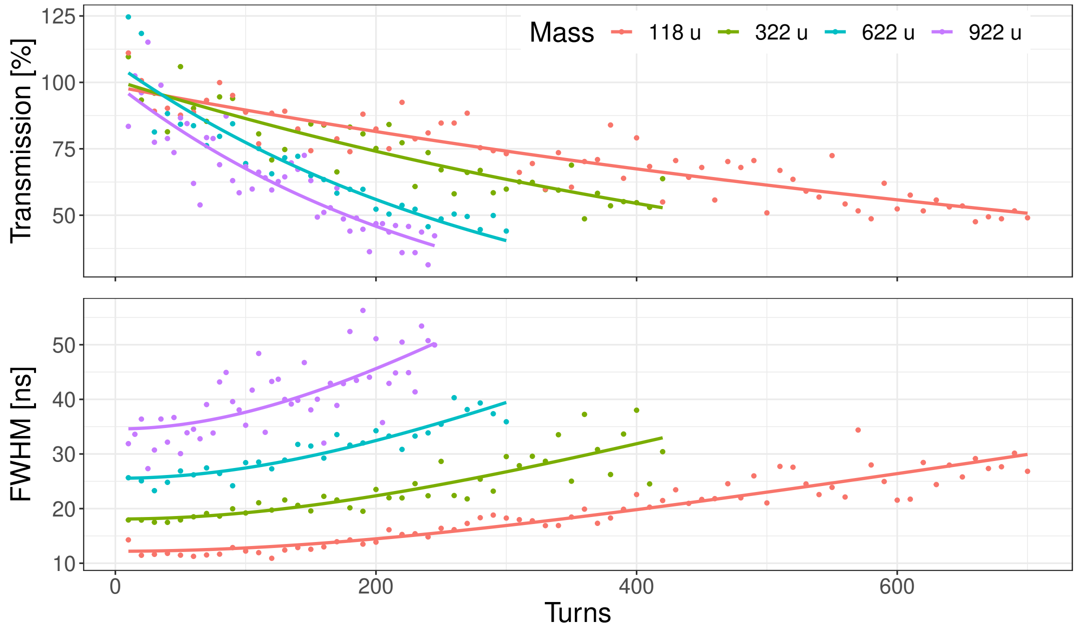

Figure 5.4.1: FWHM, transmission efficiency through the analyzer, and MRP dependent on the number of turns and the mass. Each series stops at the maximum mass-dependent turn number due to the TOF limitation of 20 ms. The measured molecules belong to the Agilent tuning mix. Continuous lines show fits to the acquired data. Transmission efficiency was fitted based on the exponential decrease. The FWHM was fitted according to Equation (5.4.1.1), which describes the acquired data well.

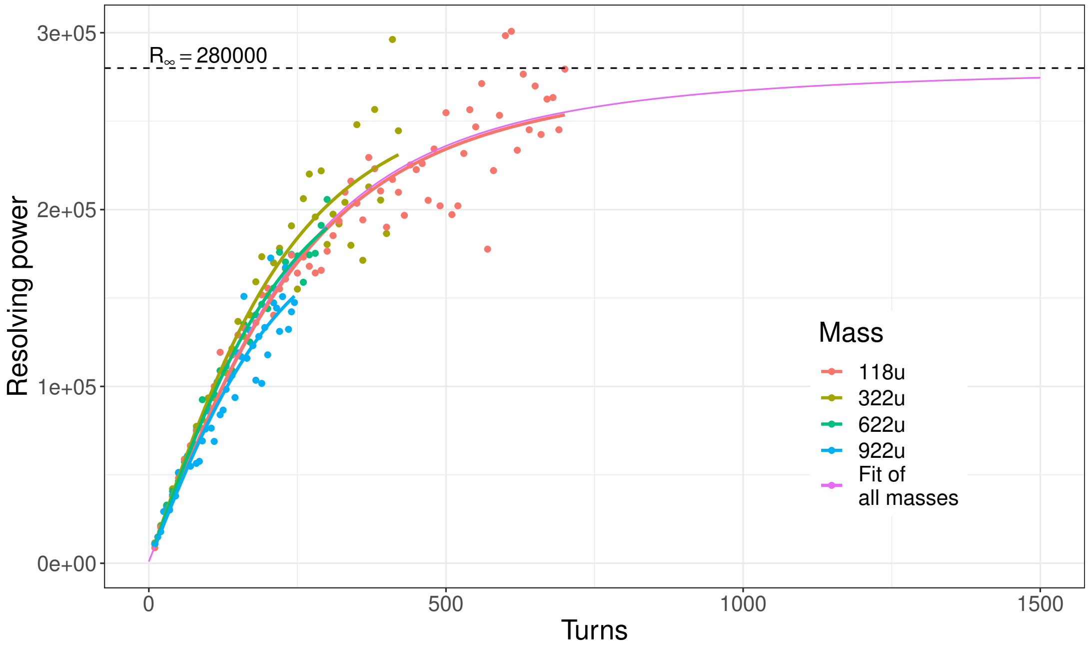

Figure 5.4.2: Measured MRP of molecules of 118 u, 322 u, 622 u, and 922 u from the Agilent tuning mix up to a total flight time of 20 ms. Continuous lines show a fit of Equation (5.4.1.1) to the acquired data for each ion species. A fit considering all ion species reaches a theoretical maximum for the MRP of 280 000 with $\Delta t_{\mathrm{TFS}} = 12.34$ ns and $\Delta t_{1\mathrm{IT}} = 38.03$ ps. The increasing dispersion within the rising turn number is likely caused by electric field fluctuations over time caused by the power supplies.

The acquired data can be used to fit a model for the MRP [Ayet San Andrés et al. 2019], which describes the dependence of the FWHM on time spread during the time focus shift and the isochronous turns:

$$\frac{m}{\Delta m} = \frac{t_{\mathrm{TFS}} + N \cdot t_{1\mathrm{IT}}}{2\sqrt{\Delta t_{\mathrm{TFS}}^2 + N^2 \Delta t_{1\mathrm{IT}}^2}} \tag{5.4.1.1}$$

The parameter t_{TFS} is the TOF from trap extraction to the detector without isochronous turns, $t_{1\mathrm{IT}}$ is the TOF needed to pass one isochronous turn, and N is the turn number. The parameters $\Delta t_{\mathrm{TFS}} = 12.34\,\mathrm{ns}$, which is the time-spread during the TFS turn, and $\Delta t_{1\mathrm{IT}} = 38.03\,\mathrm{ps}$, which is the time-spread after every isochronous turn, are adapted to fit the model to the measured data. Figure 5.4.2 shows the match of the acquired data to the theory and a hypothetical maximum MRP of 280 000.

5.4.2 Mass Accuracy

The mass accuracy estimation in [Lippert 2016] of 0.3 ppm is tested for ions with known masses within the mass range 150 - 320 u. During the measurement of CID fragment ions of $C_{23}H_{32}N^+$ (Section 6.2.5), mass-to-charge ratio values of 79 fragment ions were measured. Since their precursor molecule was cleanly isolated and composed of atoms of only a few elements, their elemental composition is mostly unambiguous. Figure 5.4.3 shows the relative deviation of their measured mass-to-charge ratio values from the literature masses as calculated from their elemental compositions. A Gaussian fit of the deviations representing the device's mass accuracy is calculated as $\sigma = 0.3\,\mathrm{ppm}$.

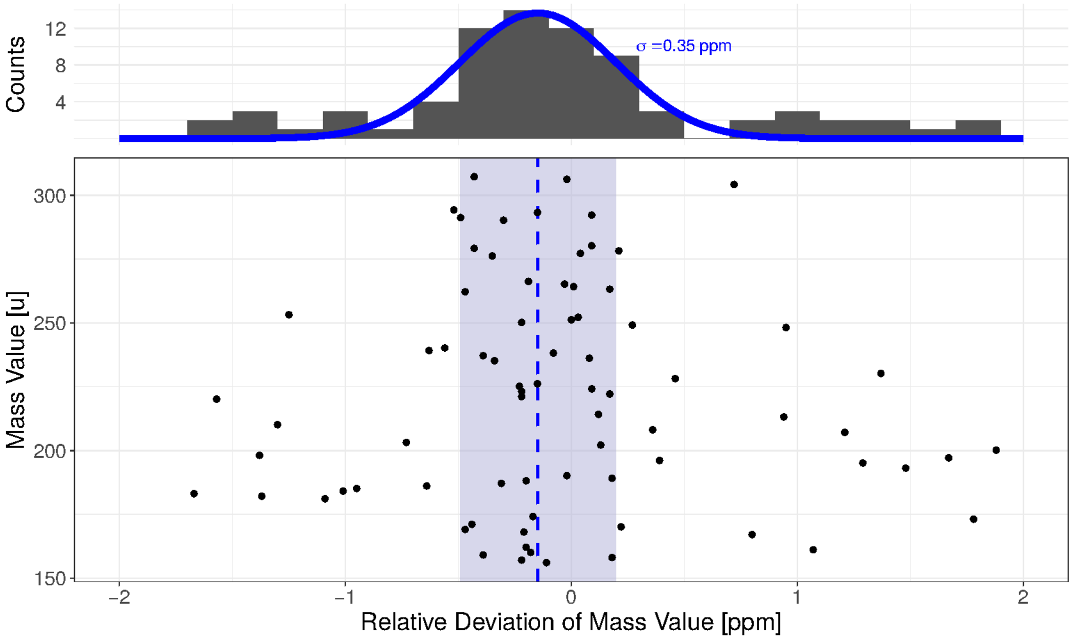

Figure 5.4.3: Relative deviation from literature mass for measured CID fragment ions of $C_{23}H_{32}N^+$. Each point represents the measured mass-to-charge ratio value (ordinate) and its relative deviation from the corresponding literature mass (abscissa). The dashed blue line indicates the mean value, while the blue area marks the standard deviation area. A projection to the abscissa is shown on top with a Gaussian distribution with the same mean and standard deviation shown with a blue line.

5.4.3 Dynamic Range

The dynamic range describes the range of signal rates that can be measured proportional to their analyte concentration. By utilizing the transmission control RFQ in combination with the MRS, the dynamic range can be virtually extended by adjusting the device's sensitivity without exchanging the analyte or source type. The adjusted sensitivity prevents space charge effects and TDC dead time while guaranteeing sufficient statistics for analysis.

To demonstrate this approach, Figure 5.4.4 shows a series of measurements of $C_{12}H_{19}O_6N_3F_{12}P_3$ and its isotope pattern, which is dominated by molecules with different amounts of ^{13}C. Between the one-minute-long measurements, the transmission efficiency is adapted to the rate of the desired ions, and the MRS is used to deflect oversaturated signals. While this lowers noise and prevents space charge effects, fringe fields close to the deflection cause a slight TOF shift. The relative abundances of the different isotopes of ^{13}C extracted from this measurement are compared to their theoretical counterparts in Table 5.3. The measured values agree with the theoretical prediction for the relative abundances, showing that the device can virtually extend its sensitivity by multiple orders of magnitude.

	$^{13}C_0$	$^{13}C_1$	$^{13}C_2$	$^{13}C_3$	$^{13}C_4$	$^{13}C_5$
Literature	0.855	0.120	0.0185	0.00179	0.000160	0.000011
Measured	0.831	0.143	0.0230	0.00157	0.000131	0.000014

Table 5.3: Comparison of the measured ^{13}C abundance ratios of the $C_{12}H_{19}O_6N_3F_{12}P_3$ isotope pattern to the theoretical values derived from the natural abundance of isotopes. The measured values agree with the theoretical values within their uncertainties.

5.5 Re-Trapping Characteristics

Re-trapping is integral in the tandem mass spectrometry experiment presented Section 6.2.5. In order to demonstrate the device's capabilities for mass separation power and re-trapping efficiency, a measurement with the molecule of 118 u of the Agilent tuning mix is presented in Figure 5.5.1. The molecule travels for 600 turns, equaling a TOF of 12.8 ms, in the analyzer before it is isolated and reinjected for a single turn until it hits the detector. A scan of the re-trapping time reveals a timespan within which the molecule of 118 u is still isolated. This timespan, regarded as the isolation window, is used to calculate the mass separation power in Figure 5.5.2. The re-trapping efficiency describes the rate of detected ions after re-trapping compared to the detection rate of ions that hit the detector after 600 turns without re-trapping. The measurement is repeated for different re-trapping potentials to investigate the agreement with the theoretical predictions.

Since re-trapping also relies on separation in space, it shows the same dependence on turn numbers as the MRP shown in Figure 5.4.1. Due to the maximum re-trapping time of 20 ms per repetition cycle and fixed kinetic energy, higher masses are limited to lower turn numbers. With $m \propto t^2$, this limitation results in a reduced maximum separation R_{sep} power depending on the mass

$$R_{\mathrm{sep}}(m) \propto \sqrt{\frac{q}{m}} \quad . \tag{5.5.1}$$

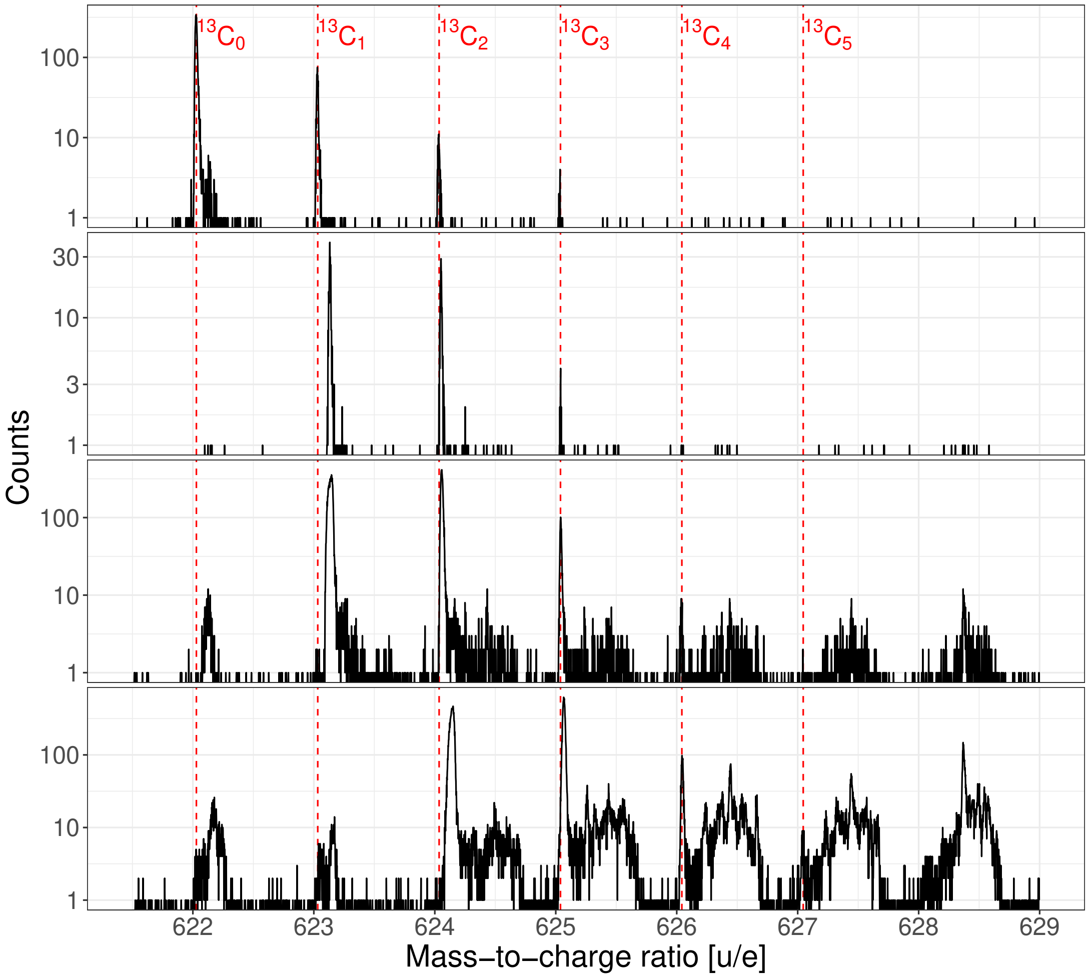

Figure 5.4.4: Dynamic range adaptation using the transmission control RFQ and MRS. Panels show accumulated raw data (black) from the TDC in logarithmic ordinate. The first peak can be assigned to the molecule $C_{12}H_{19}O_6N_3F_{12}P_3$ of the Agilent tuning mix with 12 ^{12}C isotopes and no ^{13}C isotopes. For each mass marker, the number N of the ^{13}C isotopes in the molecule is denoted as $^{13}C_N$.

First panel: $C_{12}H_{19}O_6N_3F_{12}P_3$ and molecules with $^{13}C_1$ to $^{13}C_3$.
Second panel: MRS cut on the main molecule, isotopes from $^{13}C_1$ to $^{13}C_4$. TOF shifts of $^{13}C_1$ are due to MRS fringe fields.
Third panel: MRS cut on the second molecule, isotopes from $^{13}C_2$ to $^{13}C_5$. The signals detected on the right side of the described molecules are likely impurities in the tuning mix solution.
Fourth panel: MRS cut near the third molecule, isotopes from $^{13}C_3$ to $^{13}C_5$ with higher rates. The concentration of $^{13}C_6$ is too low to stand out from the background caused by the solution.

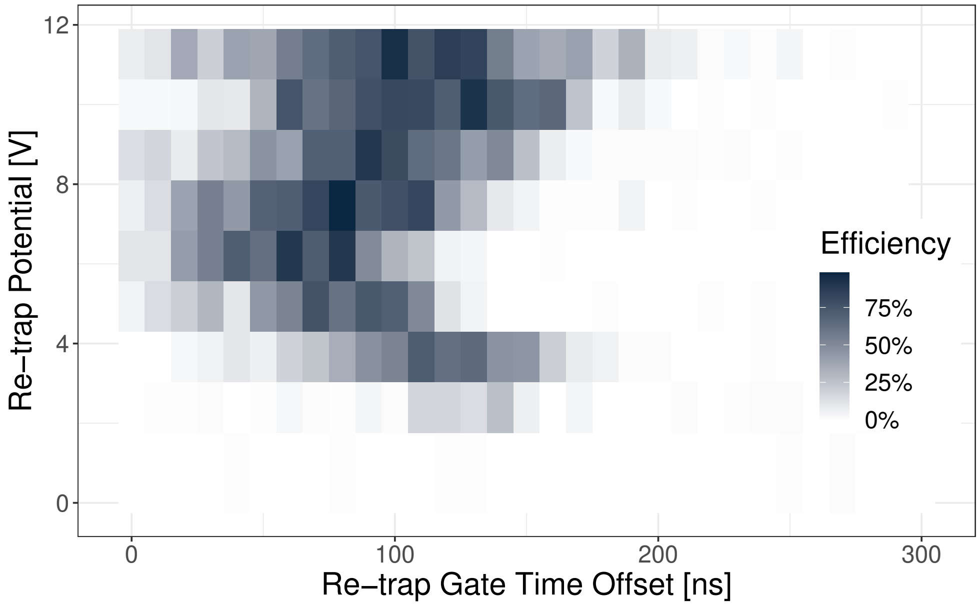

Figure 5.5.1: Re-trapping characteristics for the molecule of 118 u from the Agilent tuning solution. The ion was isolated using re-trapping after 600 turns, equaling a TOF of 12.8 ms. The re-trapping time (abscissa) and re-trapping potential (ordinate) were varied, and the detected count rate on the detector was plotted as color. The rate was normalized to the ion rate detected after 600 turns without re-trapping. Darker colors represent higher re-trap efficiency. The time offset span at which the molecule of 118 u is still visible is inversely proportional to the mass separation power. A drift effect in the re-trapping time, likely due to voltage fluctuations, of 50 ns can be observed.

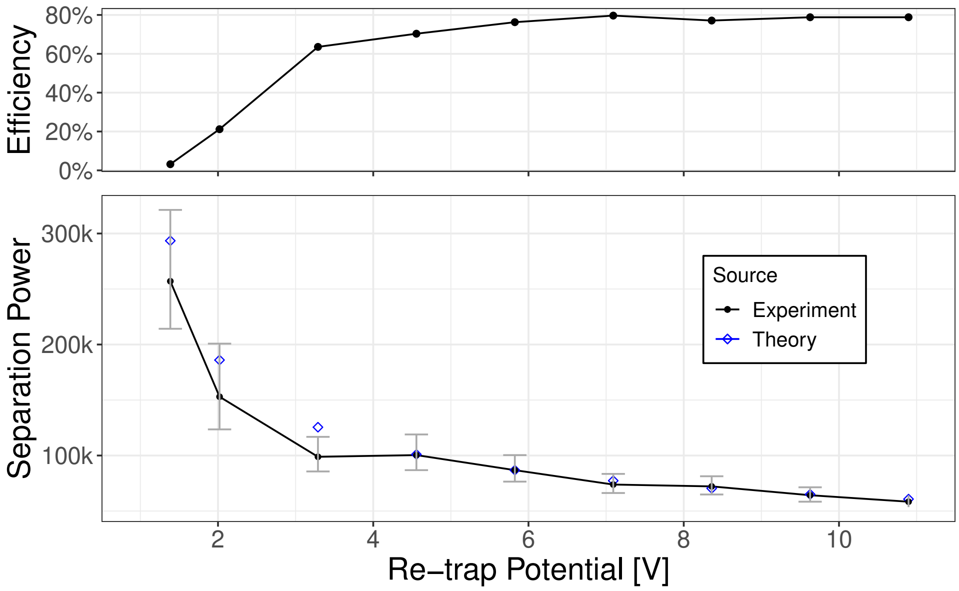

Figure 5.5.2: Re-trapping efficiency and mass separation power for the molecule of 118 u from the Agilent tuning solution. This plot visualizes the data shown in Figure 5.5.1 differently. The theoretical values are derived from Equation (5.5.2). A mass separation power of 100k can still be achieved with a re-trapping efficiency of 70 %. Higher mass separation powers can be reached (up to 260k) but suffer from sharply decreased efficiencies of 10 %. The measurement mostly agrees with the theoretical predictions within its error margin.

At the same time, the theoretical values are derived from [Timo Dickel et al. 2017] as

$$R = \frac{t_f}{2\sqrt{\Delta t^2 + \frac{2m}{q}\frac{U_r}{Er^2}}} \quad , \tag{5.5.2}$$

with t_f the TOF from trap extraction to re-trapping, Δt the FWHM of the MRP, m/q the ion's mass-to-charge ratio, U_r the depth of the axial potential well of the trap and E_r the retarding electrostatic field strength.

A mass separation power of 100 000 was achieved with a 70 % or better re-trapping efficiency and in agreement with theoretical values. Even higher mass separation powers of up to 260 000 were reached but had sharply decreased re-trapping efficiencies of below 20 %. A TOF drift effect can be observed in Figure 5.5.1 when following the center of the isolation window from bottom to top. This oscillating TOF shift of up to 50 ns is likely caused by voltage fluctuations of the analyzer electrodes during the 30-minute-long measurement.

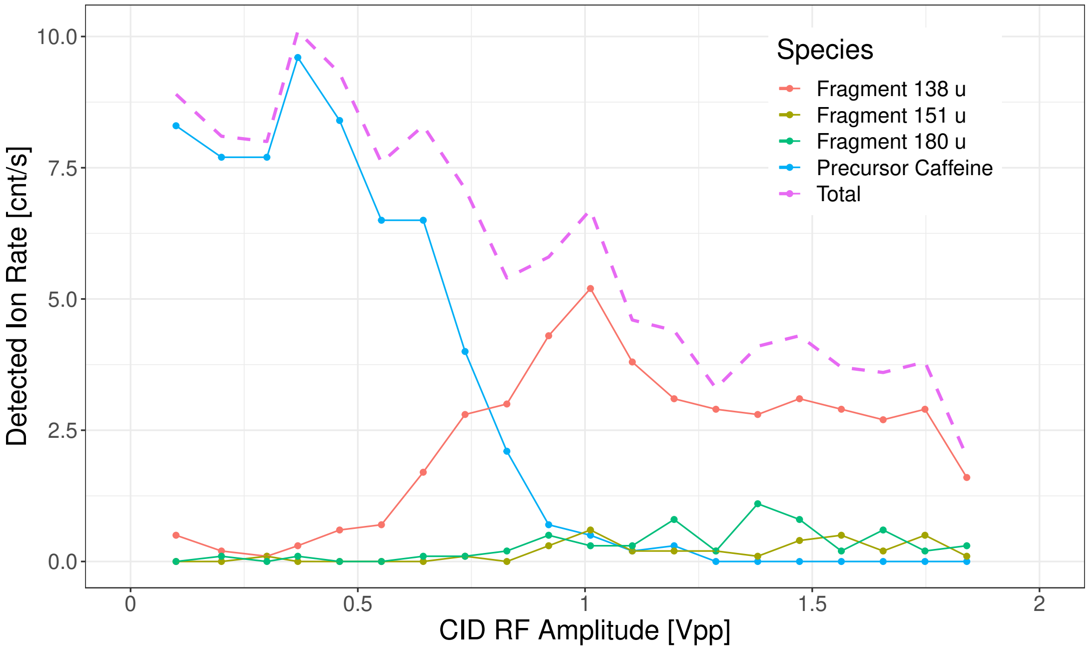

Figure 5.5.3: Effect of CID on the mass spectrum composition of caffeine molecules ($C_{22}H_{28}ON^+$, 195 u). After re-trapping, a CID signal with a frequency of 110 kHz is applied for 2 ms to fragment the caffeine molecules. With rising CID RF amplitude, molecules with mass-to-charge ratio values of 138 u/e, 151 u/e, and 180 u/e are detected at an increasing rate while the detection rate of the molecule decreases.

A demonstration of CID during tandem mass spectrometry is shown in Figure 5.5.3, where the molecular ion of caffeine (195 u, $C_{22}H_{28}ON^+$) is dissociated with different CID energies. The precursor rate declines with increasing CID energy, while three fragments start to appear, of which 138 u is dominant. With enough CID energy, the fragment rates also start declining due to their fragmentation. The total loss in ion rate is caused by fragments not being contained in the RFQ-trap set to contain caffeine.

5.6 MS^4 Tandem Mass Spectrometry

Higher-order tandem mass spectrometry can identify fragments produced by dissociation in previous stages. Fragments with ambiguous structures often form from precursor molecules of complex structures like biomolecules or when the precursor signal consists of many isomers. An additional stage can isolate a fragment of interest and clarify its structural formula. To the author's knowledge, this device is the first MR-TOF-MS capable of higher-order tandem mass spectrometry (MS^3 and MS^4).

The closed-path analyzer type this device's analyzer utilizes allows for the re-trapping described in Section 2.6.5 to be applied multiple times with the previously presented characteristics available in each stage. In practice, a limited amount of timing sequence channels, CID signal generators, and re-trapping efficiency limit the amount of tandem mass spectrometry stages.

By synchronizing a second trigger system FPGA as described in Section 4.3 and extending the control software, the device became capable of tandem mass spectrometry of third and fourth order (MS^3 and MS^4). In this process, the precursor molecule is injected into the analyzer, isolated using re-trapping, dissociated using CID, and re-injected into the analyzer in each but the final stage, where ions impact onto the detector.

The measurement in Figure 5.6.1 shows the application of MS^4 using re-trapping for isolation-in-time and CID after each stage. A subsequent measurement visualizes each stage after a single turn in the analyzer to measure a broad mass range of 190 - 330 u. All fragments are assumed to originate from the dominating molecule $H_{19}C_6N_3O_6P_3$ with a mass of 322.048 u. Its structural formula, shown at the top of Figure 5.6.1, suggests a strong bond of nitrogen and phosphor with a preference for losing carbon, hydrogen, and oxygen, which was considered for identifying the fragments. CID was applied using an additional sinusoidal component to one of the trap RFQ segments with customizable amplitude and frequency for 300 periods, translating to between 4.7 - 6.2 ms for the frequencies used in this measurement.

The first stage (MS^2) isolates a naturally occurring fragment of 322 u, with the elemental composition $H_{17}C_5N_3O_6P_3$ and a mass value of 308 u with a re-trapping efficiency of 87 %. Its fragmentation at a resonant frequency of 49 kHz with 6.4 V amplitude produces two main fragments with mass values of 276 u ($H_{13}C_4N_3O_5P_3$) and 294 u ($H_{19}C_5N_3O_5P_3$).

In the second stage (MS^3), the molecule with a mass of 276 u is isolated. However, the fragment of 294 u is also formed during isolation. Considering only the molecule at 276 u, a re-trapping efficiency of 65 % was reached. Using the MRS in the second stage to block masses above 280 u revealed that the molecule is produced after re-trapping. This origin is also confirmed by the second peak vanishing after applying CID of 61 kHz at 5 V amplitude to dissociate the molecule with a mass of 276 u. In the resulting fragments, a similar reaction takes place for one of its fragments ($H_{15}C_4N_3O_4P_3$, 262 u) to produce a heavier fragment than the precursor molecule with a mass of 280 u ($H_{17}C_4N_3O_5P_3$). This reaction with the H_2O molecules residue in the buffer gas is likely due to the strong hygroscopic nature of the formed fragment molecules that the presumed fragmentation process depicted in Figure 5.6.2 predicts.

For the third stage (MS^4), the fragment with a mass of 264 u is isolated and dissociated at 64 kHz and 6 V amplitude. A re-trapping efficiency of 62 % was reached. The final spectrum shows a dominant fragment with a mass of 232 u ($H_{13}C_3N_3O_3P_3$), reacting again with H_2O to $H_{15}C_3N_3O_4P_3$ (250 u).

The measurement showed that the device is capable of isolating and dissociating for tandem mass spectrometry up to the fourth order while maintaining a high isolation efficiency and mass separation power.

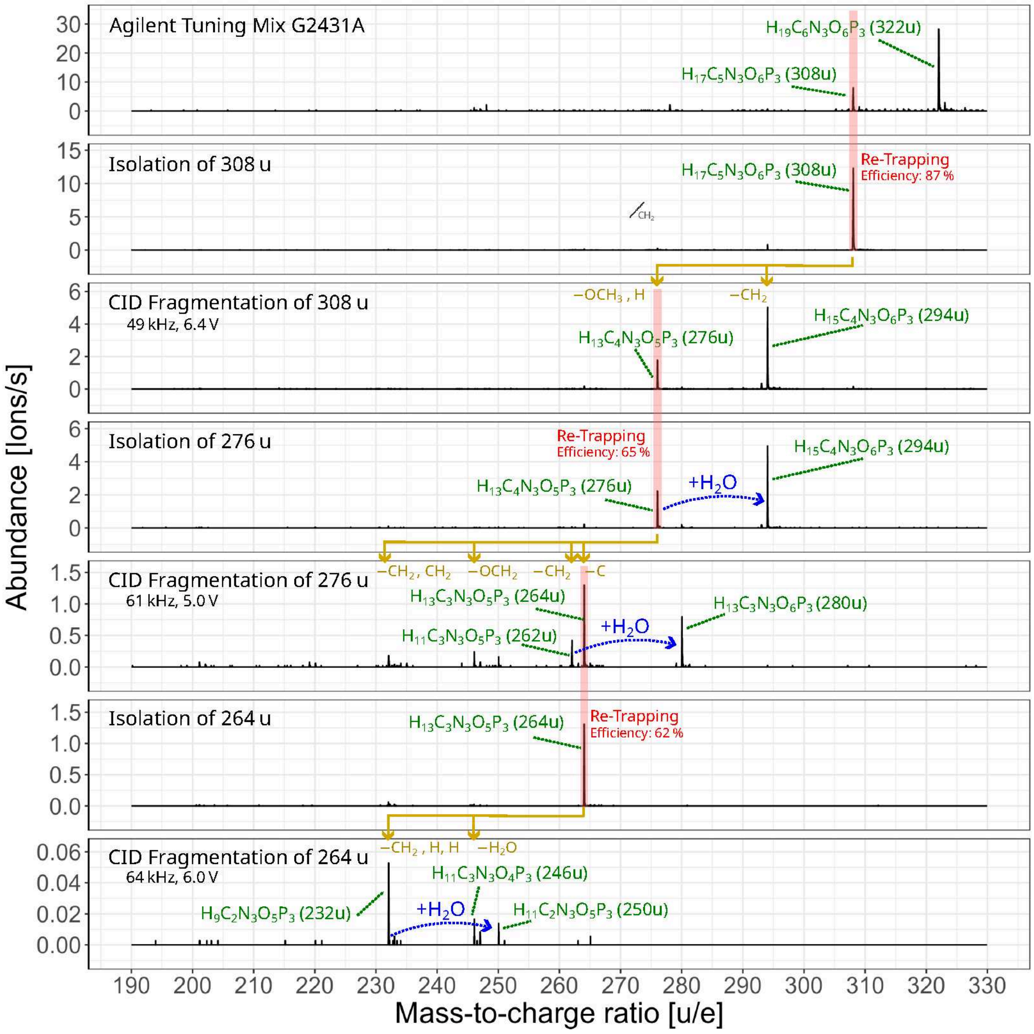

Figure 5.6.1: Four-stage tandem mass spectrometry(MS^4) of a precursor molecule at 308 u from the Agilent tuning mix.
From top to bottom, the process through the different stages is shown. The stages are followed by injecting ions into the analyzer for one turn before measuring with the detector.
Isolation stages using re-trapping have a red frame for their target area. CID applications are marked in yellow, pointing from their target peak to the produced fragments. The structural formula for 322 u is given at the top. Signals are labeled with assumed elemental compositions in green.
The naturally occurring fragment of 322 u at 308 u is isolated (MS^2) and dissociated (CID). Of the product ions, 276 u is isolated (MS^3), and a second peak at 294 u is formed after re-trapping by a reaction with H_2O. The spectrum produced by dissociation of 276 u also includes a mass at 280 u produced by a reaction with H_2O of a lighter fragment. In the fourth stage, 264 u is isolated (MS^4) and fragmented using CID.

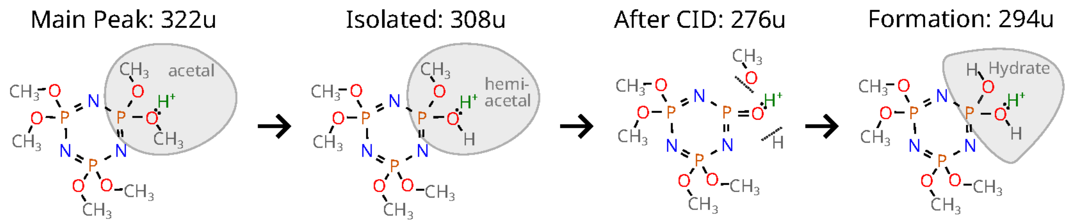

Figure 5.6.2: Assumed formation the H_2O adducts after applying CID to the Agilent tuning mix. From a spectrum surrounding $M_{322} = H_{19}C_6N_3O_6P_3$ with a mass value of 322 u, a naturally occurring fragment $M_{308} = H_{17}C_5N_3O_6P_3$ at 308 u is isolated. The latter molecule is fragmented using CID and produces a fragment $M_{276} = H_{13}C_4N_3O_5P_3$ at 276 u and a fragment $M_{294} = H_{15}C_4N_3O_6P_3$ at 294 u. After M_{276} is isolated in the second stage, M_{294} is still observed in the spectrum. The depicted assumed fragmentation process suggests that $M_2 76$ is highly hygroscopic and reacts in the RFQ trap with the residue water from the humidity of the air entering the system through the API.

5.7 Mass Range: Measurement of Proteins

The measurement of proteins can be difficult due to their high molecular mass in the order of thousands of atomic mass units and their tendency to fragment in the presence. In order to show that the device can be used to measure proteins in the future, a mass measurement of human insulin was recorded.

The human insulin (5809.7 u) is dissolved with a concentration of 10 ppm in a solution of MeOH and water mixed at the ratio of 1:1. To support ionization, 0.02 % formic acid is added. The micro-ESI source with the inlet heated to 150 °C is operated at 3.25 kV generating a stable ion rate.

The human insulin's isotope pattern with sodium (+23 u) and potassium (+39 u) adducts was measured and identified in different charge states. Ions charged 4 to 8 times ($m/q = 1452.42 - 726.21$ u/e) could be seen without adapting RFQ RF frequencies or further hardware modifications. Figure 5.7.1 shows a measurement of the isotope pattern of 6+ charged insulin with its adducts sodium and potassium.

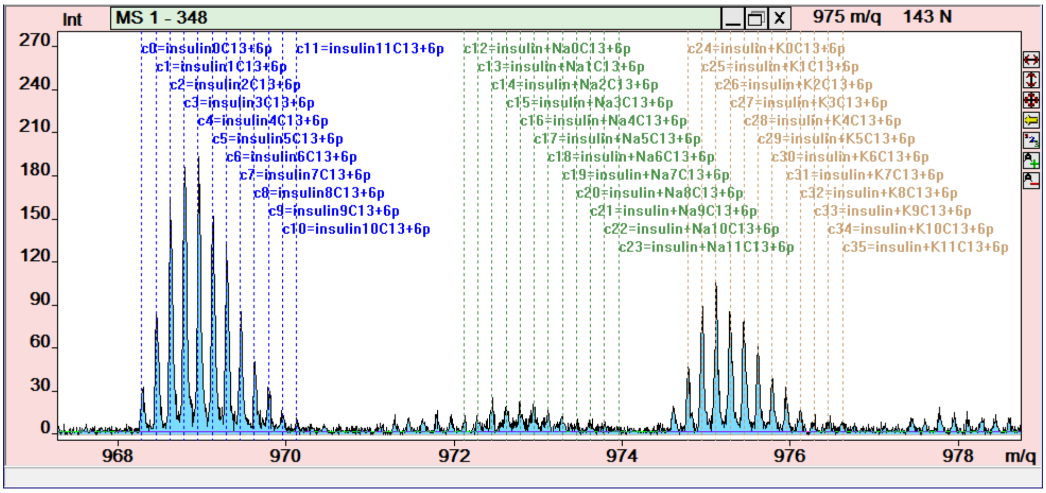

Figure 5.7.1: Mass spectrum of 6 times charged human insulin. The mass signals were identified by comparison with the isotope pattern, while mass filter and MRS guarantee the unambiguous mass range and, thus, identify the charge state. The adduct-free insulin isotope pattern dominated by different amounts of ^{13}C is marked in blue, sodium adducts in green, and potassium adducts in brown. Assistance in the identification of insulin and its adducts was kindly provided by the workgroup of Dr. Spengler at the JLU Gießen.

6 High-Resolution Tandem Mass Spectrometry of Crude Oil Residue

6.1 Structural Analysis of Crude Oil Samples

To demonstrate the presented device's capabilities in a realistic application, we investigate the structural information of molecules in a medium-heavy crude oil residue sample. This sample stands out for its complex, dense, and highly populated composition of isobars while being well-suited for ionization with electrospray methods. The dense population of isobaric molecules allows the device to demonstrate its outstanding mass separation power and isolation efficiency. The chosen precursor molecules also require low enough dissociation energies, such that they can be dissociated using CID within the RF trap. The crude oil sample and the final analysis of the structural information of the acquired data were provided in collaboration with the workgroup *Mass Spectrometry* lead by Prof. Dr. Wolfgang Schrader of the *Max Planck Institut für Kohleforschung* in Mülheim an der Ruhr (further referred to as *WG Schrader*).

Despite advancements in renewable energy, a significant portion of energy consumption still depends on crude oil. As light crude oil reserves diminish, there is a need to refine overlooked heavier or sulfur-rich oils [Vetere et al. 2018]. Furthermore, Understanding the structure of crude oils aids, for example, in creating chemical responses to oceanic oil spills [Zhu et al. 2022] and optimizing biofuel production [Ketabchi et al. 2019].

A common approach of structural elucidation utilizes the fragmentation of isolated precursor molecules in tandem mass spectrometry (Section 2.3). The fragmentation patterns in the resulting mass spectra are then compared to known fragmentation processes to reconstruct the precursor molecule's structure. Commercially available solutions (see Table 6.1) with a high mass resolving power can often only isolate up to half a mass unit, resulting in overlaying fragmentation spectra of many precursor isobars.

Structural analysis of organic compounds by tandem mass spectrometry still poses a challenge due to their complexity and dense population of isobaric molecules, requiring a high mass separation power for proper isolation [Panda et al. 2007]. This is demonstrated in Table 6.2, where the mass splits for common molecular adducts in organic molecules are listed. For example, a molecule that contains a NH_2-compound instead of CH_4 only differs by 12.6 mu and would require a separation power of at least 52 000 for mass values at 322 u to be properly isolated. Unless the precursors are properly isolated before dissociation, the resulting mass spectrum will be too convoluted by the fragment patterns of all the precursor molecules to be properly analyzed.

Synthesized and less densely populated samples can be used to compensate for a lower mass separation power in tandem mass spectrometry. Their fragmentation

Analyzer type	Resolving power		Mass accuracy		Measurement time[a]
	MS-1	MS-2	MS-1	MS-2	(seconds)
Magnetic (B) sector	Medium	Medium	ppt	ppt	10^{-5}
Electric (E) sector	na[b]	Low	na[b]	ppt	10^{-5}
Electric and magnetic sector[c]	High	Medium	ppm	ppt	10^{-5}
Time-of-flight (TOF)	Low	Medium[d]	ppm	ppm	10^{-5}
Quadrupole mass filter (Q)	Low	Low	ppt	ppt	10^{-4}
Quadrupole ion trap (QIT)	Low	Low	ppt	ppt	10^{-2}
FTICR	High	High	ppm	ppm	10^{-1}
Orbitrap	na[b]	High	na[b]	ppm	10^{-1}

[a] The time, after activation, for the ions to react prior to the second stage of analysis.

[b] na: not applicable; this analyzer has not been used for the first stage of an MS/MS experiment. There is currently no mode of operation in which a parent ion can be mass selected for a subsequent stage of analysis.

[c] When electric and magnetic sectors are used as a double focusing mass spectrometer for one stage of analysis, either prior to (MS-1) the reaction, or subsequent to (MS-2) the reaction.

[d] The resolving power is medium if the TOF ion axis is orthogonal to the first stage of MS; if the axes are coaxial, the resolving power is Iow.

Table 6.1: Different mass analyzers for tandem MS with their performance attributes. *Low* refers to a mass resolving power below 1000, *Medium* to 1000 - 10 000 and *High* to above 10 000. The table was copied from [Glish et al. 2008].

Elemental Compositions	Mass Values [u]	Mass Split [mu]	Required R_{sep} at 322 u
O - CH_4	15.9949 - 16.0313	36.3	19 800
NH_2 - CH_4	16.0187 - 16.0313	12.6	52 000
S - O	31.9721 - 31.9898	17.8	36 000
N_2H - O	32.0374 - 31.9898	47.6	13 600
SH_4 -C_3	36.0034 - 36.0	3.3	196 000
$^{13}CH_3S$ - C_4	47.9999 - 48.0	1.1	580 000

Table 6.2: Important mass splits for organic compounds. The list depicts four groups of molecular adducts with similar mass values which require a high mass separation power R_{sep} to be resolved. The required separation power for molecules is calculated with $2 \cdot 322\,\mathrm{u}/m_{\mathrm{split}}$, estimating that at least two times the FWHM is required as a distance between the signals to separate the ions.

spectra are easier to analyze but bear a risk of oversimplification since only compounds presumed to be present are included [Vetere et al. 2018]. A different approach couples different spectrometry techniques, for example, separating samples with normal phase liquid chromatography (LC) beforehand. While Ultra-high-performance liquid chromatography can reach chromatographic resolutions up to a few hundred thousand, the actual separation depends on the interaction of the sample with the mobile and the stationary phases and how close to each other the molecules elute. In addition, since individual components often exist only in minute amounts, co-adding enough transients to satisfy sensitivity requirements lowers the chromatographic resolution drastically [Schrader 2013].

The MR-TOF-MS presented in this work provides not only a high ion transmission efficiency and mass accuracy but also a very high mass separation power. A clean isolation helps at identifying elemental composition to fragments, because the set of available atoms and fragmentation processes is limitted by the precursor, which in this case can be clearly assigned.

6.2 Workflow

6.2.1 Sample Preparation and Ionization

The undiluted crude oil sample (Figure 6.2.1) was provided by the WG Schrader and diluted at 250 ppm with MeOH and toluene according to Table 3.1.

Figure 6.2.1: Photograph of the pure medium-heavy crude oil residue sample sent by the WG Schrader. The sample is brownish-black, viscous, and has a slight smell.

The nano-ESI ion source was utilized to create a spectrum of a broad mass range. The hollow glass emitters with the metal-coated needle tip were filled with the solution using a syringe made from glass and metal to avoid contamination with plastic components. The emitter was then clamped into its holder and aligned to the heated inlet module of the API.

The fragmentation spectra for structural analysis were acquired using the micro-ESI ion source. The solution was filled into a syringe connected to a metal capillary aligned to the heated inlet module of the API. The syringe was operated automatically with a motor at a set speed to allow for a constant production rate of ions.

6.2.2 Broadband Spectra of Crude Oil Sample

Before selecting a specific molecular species for structural analysis, the molecular composition of the crude oil sample was investigated in a broadband scan covering the mass range 290 - 590 u. To this end, the *spectrum patching* technique (see Section 4.7) was applied.

The mass range was intersected into smaller, mass-dependent sections that each fit into one unambiguous mass range with the desired MRP. For example, mass-to-charge ratios at 322 u/e with an MRP of 200 000 require a turn number of 300, which results in an unambiguous mass range of 1.7 u. The TOFControl software adjusts hardware parameters automatically to the target mass range, including the timing sequence and RFQ RF amplitudes, while acquiring the data.

The scaling technique mentioned in Section 4.7 scales the measured abundances according to a reference spectrum to avoid distortions. Ten reference spectra that span over the total mass-to-charge ratio range of 290 - 550 u/e were acquired at a turn number of 10 IT, reaching an MRP of 15 000, as shown in Figure 6.2.2. While merging the measurement sections, their abundance was scaled to correlate to the corresponding range within the reference section.

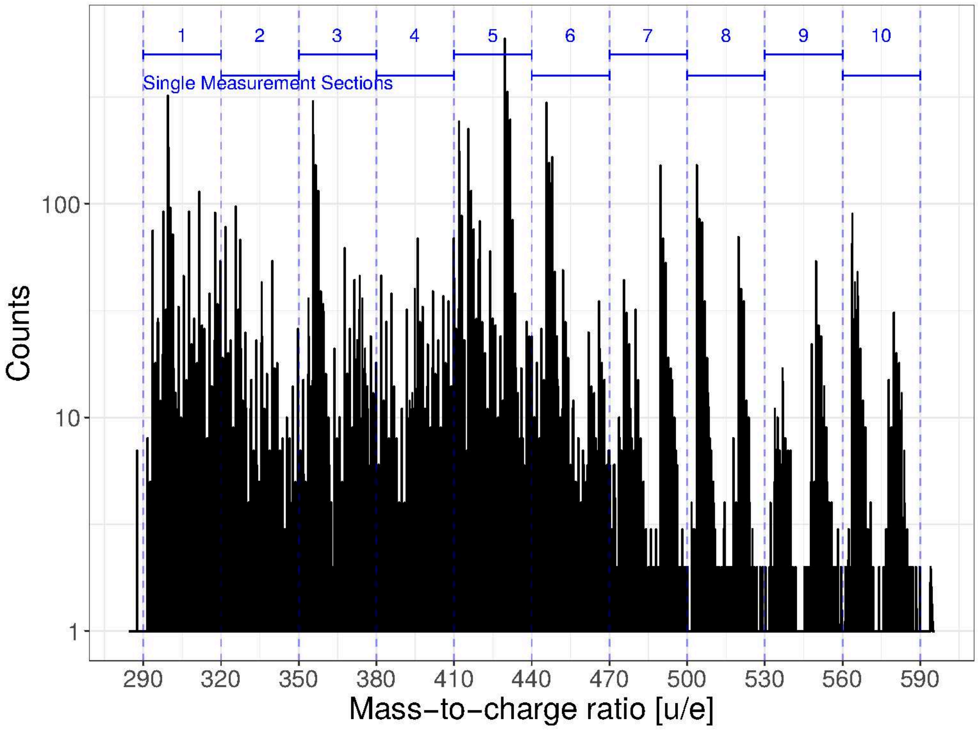

Figure 6.2.2: Broadband spectrum of the medium heavy crude oil sample consisting of ten measurements with intermediate resolution, each acquired after 10 IT, corresponding to a TOF of 0.4 ms. The MRP in this stage is 15 000. This mass spectrum is used as a reference for the scaling process for patching the spectra acquired with high resolution. The ordinate is depicted with logarithmic scale.

Next, a high-resolution spectrum at an MRP of 230 000 was obtained by performing 151 individual measurements with a mass-to-charge ratio of 1 - 2 u/e each, shown in Figure 6.2.3. The measurement took around 5 hours while in comparison, the reference spectrum were acquired within 10 minutes each. The patched spectrum consists of more than 2600 separated ion signals, mostly structured in isobaric clusters of 5 - 30 ions per isobar. While most lighter mass numbers have at least one isobaric cluster, the isobaric population of ions heavier than 480 u/e is less dense.

The main problem with spectrum patching arises from TOF drift effects during the measurement that cause calibration distortions and deteriorate mass accuracy. Three calibrants of the Agilent tuning mix (see Table 5.1) at 118 u, 322 u, and 622 u were measured periodically every hour to correct the calibration during the 5 hours of measurement.

The dual emitter capability of the new API allows the parallel use of different nano-ESI emitters to be quick and efficient. Two nano-ESI emitters, one with a sample of the medium-heavy crude oil residue and one filled with the Agilent tuning mix, were used in this measurement with settings according to Table 3.1. To correct for faster distortions, TOFControl was used to measure each mass section five times and apply a time-resolved calibration (TRC, see Section 4.4) within each section, further referred to as *soft TRC*. Neglecting these TOF shifts would have introduced a change of 200 ns, corresponding to a mass shift of 15 mu, and reduced the MRP by 40 %.

However, due to the vast mass difference between the calibrants at 118 u/e, 322 u/e, and 622 u/e, the mass accuracy is reduced for mass values far between them. Mass

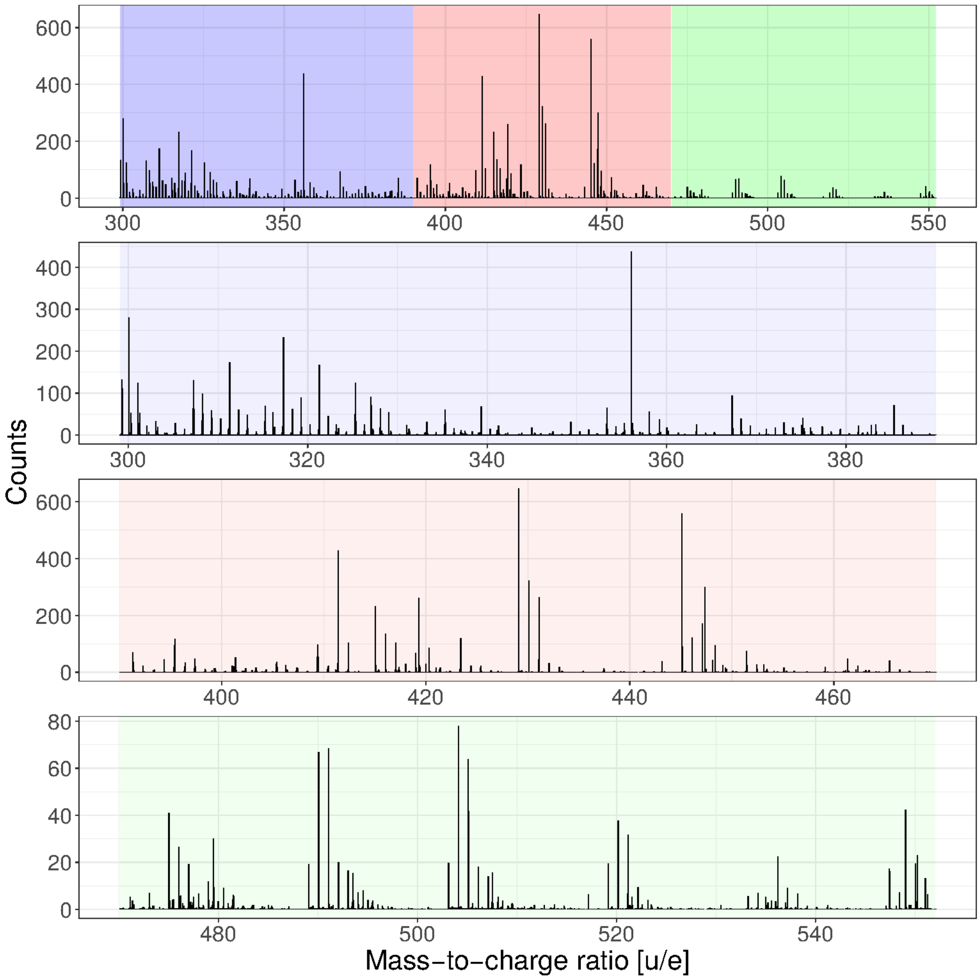

Figure 6.2.3: Mass spectrum of the medium-heavy crude oil sample, which was acquired by using the spectrum patching technique after ionization using micro-ESI. The top segment shows an overview of the mass range 300 - 550 u/e, while the three segments below, colored in blue, red and green, show the colored areas from the overview, respectively, to better visualize the achieved resolution. Each section was acquired with 300 turns, corresponding to a TOF of 10.6 ms, and achieved an MRP of up to 230 000.

accuracy tests on identified samples revealed a deviation of up to 50 ppm. This value can be improved by using closer-lying calibrants more frequently, ideally for smaller measurement sections. However, the results were sufficient to gain an overview of the content of the crude oil sample and for choosing precursor molecules. Due to the mentioned problems and highly complex analysis procedure, the following measurements used the faster and more reliable turn deconvolution technique.

6.2.3 Precursor Isolation

The first step of detailed structural elucidation by using CID is the isolation of the precursor ion. In a complex spectrum of the medium-heavy crude oil residue, like the one shown in Figure 6.2.3, often hundreds of signals are present within a 1 u/e broad mass window. Here, the extremely high mass separation power of this device enables proper isolation of single precursor molecule signals with enough abundance left for structural elucidation.

The spectrum of medium-heavy crude oil residue shown in Figure 6.2.4 shows an

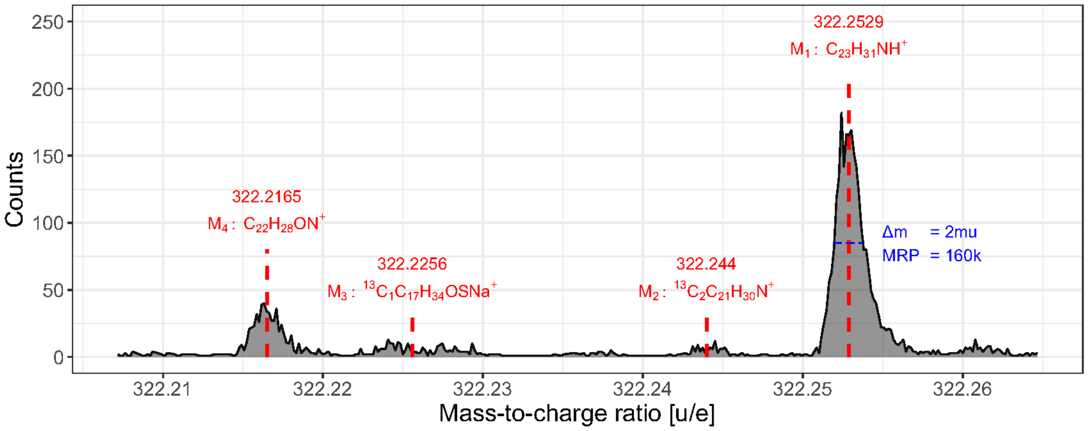

Figure 6.2.4: A mass spectrum of molecules at 322.2 u in the medium-heavy crude oil residue sample, which were chosen as precursor molecules for MS^2. The red marks refer to the precursor molecule's label, elemental composition, and literature mass value. This spectrum was acquired after a TOF of 11 ms (300 turns) with an MRP of 160 000.

isobaric group of molecules within the mass range of 322.21 - 322.26 u/e, which were chosen as precursor candidates. Their assumed elemental composition and theoretical mass value are listed in Table 6.3 and further references to each molecule will make use of the listed label M_1 to M_4.

Elemental Composition	Label	Literature Mass
$C_{22}H_{28}ON^+$	M_4	322.2165 u
$C_{17}{}^{13}CH_{34}OSNa^+$	M_3	322.2256 u
$C_{21}{}^{13}C_2H_{30}N^+$	M_2	322.244 u
$C_{23}H_{32}N^+$	M_1	322.2529 u

Table 6.3: Crude oil residue precursor molecule information.

The re-trapping procedure described in Section 2.6.5 was applied to isolate the ions M_1, M_2, M_3, and M_4. The mass spectra before isolation and after isolating each precursor molecule are shown in Figure 6.2.5.

A re-trapping trap depth of 8 V with a trapping RF amplitude of 296 V ($q_x = 0.42$) at a frequency of 935 kHz was chosen to isolate the precursor molecules efficiently with a mass separation power R_{sep} of 32 000. Since the mass separation power was not high enough to completely isolate neighboring precursor molecules with a mass distance of 10 mu, the suppression power of the neighboring signal becomes important. By isolating M_2, the initial ratio of abundances for M_2 to M_1 of 1:25 was increased to 8:1, resulting in a suppression factor of 200 for M_1.

Ion transmission toward the trap had to be reduced to 10 % to prevent space charge effects. In order to ensure that voltage drifts would not make the precursor molecule's TOF shift out of the 100 ns wide re-trapping window, the re-trapping time was adjusted periodically during the measurements. Especially, ions with low abundance and with abundant neighbors, like M_2 and M_3, required diligent correction of the re-trapping time by hand using the TOFControl software's time sequence control. The re-trapping time here was chosen with a slight bias of the re-trapping window away from the abundant peak to enhance the suppression of the neighboring abundant species. Despite these difficulties, the isolation spectra in Figure 6.2.5 demonstrate the device's excellent

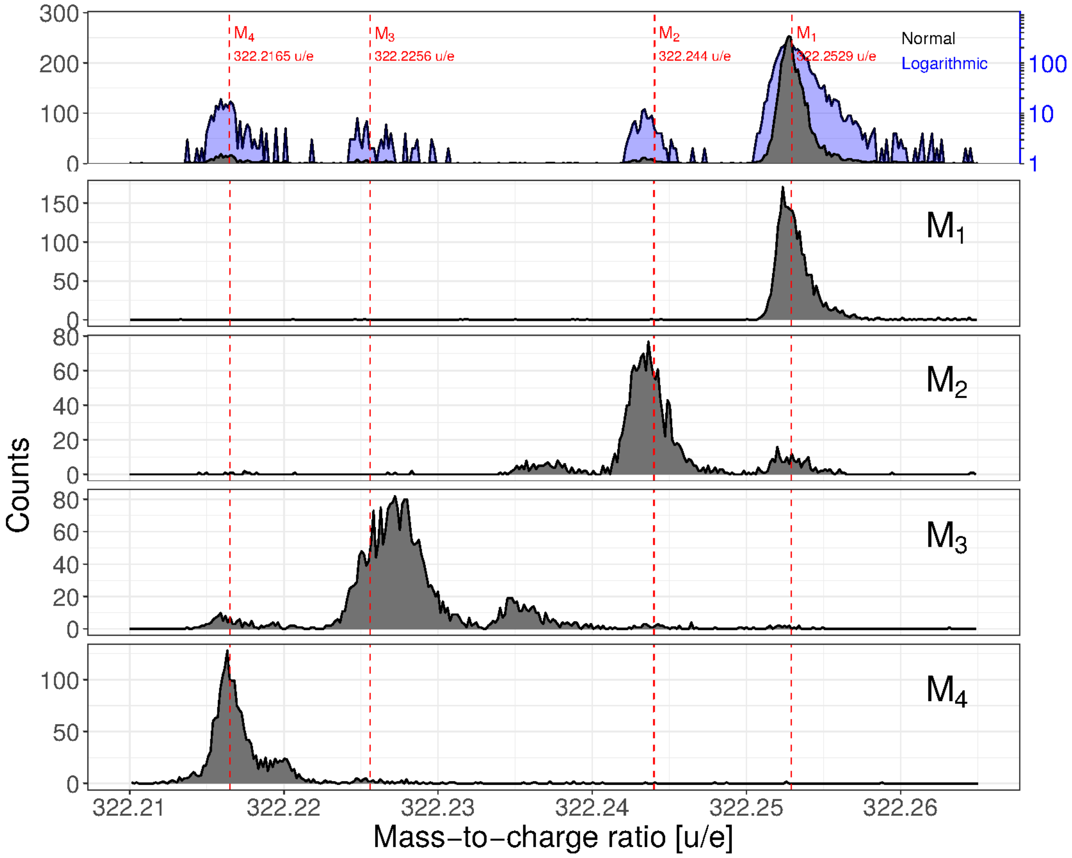

Figure 6.2.5: The top panel shows the spectrum composition of the crude oil sample without isolation. For visibility reasons, the data is depicted twice, once black in linear scale and once blue with a logarithmically scaled ordinate. The other panels show the spectra of the isolated precursor molecules M_1, M_2, M_3 and M_4 from top to bottom, respectively. Each spectrum was acquired with 300 turns, corresponding to a total TOF of 10.6 ms and an MRP of 160 000 and a FWHM of 2 mu/e.

separation capabilities.

6.2.4 Structural Elucidation using CID

After the re-trapping, the isolated molecules were exposed to resonant excitation (CID) inside the RFQ trap as described in Section 2.5.3. The setup supports CID with a wide range of settings where an additional RF voltage with a frequency of 1 Hz to 20 MHz and an amplitude of 1 - 20 V_{PP} for a duration of 1 - 15 ms can be applied to one of the trap RFQ electrodes to induce monopolar excitation. In this case, low-energy CID was applied to slowly add energy to the molecules by collisions with the N_2 buffer gas at a pressure of $1 \cdot 10^{-2}$ mbar over time, which accumulates in the form of rotation and vibration until molecular bonds dissociate.

An excitation RF frequency of 40 kHz with an amplitude of 6.5 V_{PP} applied for 10 ms provided the highest yield of detected fragments for the precursor molecules listed in Table 6.3. Simulations suggest that, in this scenario, the precursor molecules experienced about 3000 collisions with the N_2-buffer gas molecules with an average energy transfer of 0.37 eV per collision, leading to an effective temperature of about 3000 K. For the precursor molecule M_1, the rate of detected fragment ions within 150 - 320 u/e equaled half of the detected rate of the precursor ions before applying CID,

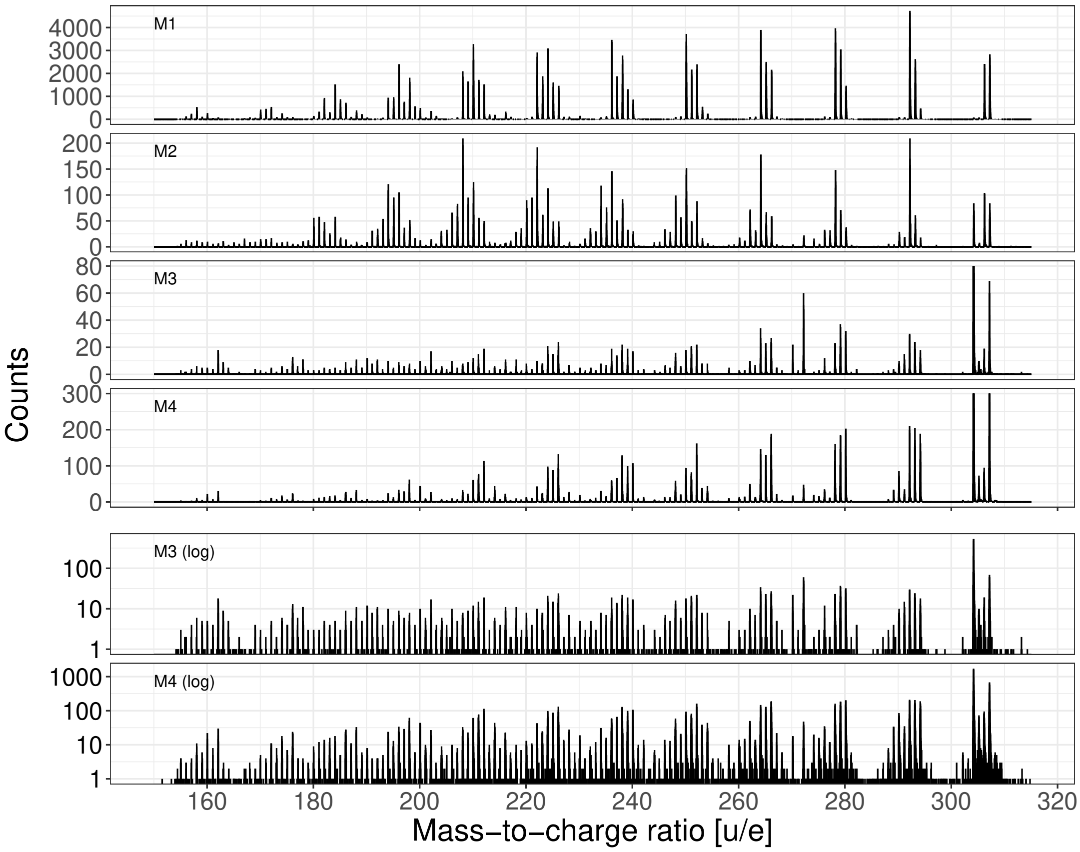

Figure 6.2.6: The mass spectra show an overview of the fragments of each precursor molecule listed in Table 6.3 after CID was applied in MS^2. The spectra were acquired with a low MRP of 3000 after a single turn, corresponding to a TOF of 78 µs. The data of M_3 and M_4 is each shown once in logarithmic scale and once in linear scale with the intense signal at 304 u/e cropped to improve visibility of the less abundant lighter clusters.

suggesting a highly efficient CID process.

Once the produced fragments were cooled enough again for 10 µs, they were re-injected into the analyzer to acquire their spectrum at the detector after they traveled another given number of turns. The fragment spectra recorded after a single turn with a medium MRP of 3000, but a wide unambiguous mass range of 150 - 320 u/e, are shown in Figure 6.2.6.

6.2.5 High-resolution Tandem MS via Turn Deconvolution

Analyzing the presented precursor molecules' tandem MS CID fragment spectra in Table 6.3 requires a high MRP and mass accuracy for a wide mass-to-charge range. To avoid voltage drift effects and to speed up the process compared to *spectrum patching* (see Section 6.2.2), the technique of *turn deconvolution*, as described in Section 4.8, was applied. With this technique, the four fragment spectra of 150 - 325 u were acquired with an MRP of 250 000 and a mass accuracy better than 1 ppm.

The application of the three stages of the turn deconvolution technique described in Section 4.8 is visualized in Figure 6.2.7 for the M_1 precursor molecule. A low-resolution mass spectrum is acquired first and divided into groups. In the second stage, each group is isolated and measured at an intermediate resolution to determine the best setting for the third stage so that no signal will be distorted or overlap. The third stage yields a single, high-resolution mass spectrum featuring all fragments observed in the second stage, but at a much higher turn number. The corresponding mass ranges for each of the up to 20 different turn numbers overlap. A mass line's mass-to-charge ratio can then only be determined with the correct turn number, devised from the estimations of the second stage.

The overview spectrum of the first stage was acquired within 3 minutes and had an MRP of 3000 with a mass accuracy of 60 ppm. While the mass accuracy was too poor to identify molecules, it showed the general composition of fragment ions. The mass range of this spectrum was divided into seven sections, each of which included a group of ion clusters. Each section had 4 - 12 ion species and its mass-to-charge range was chosen to minimize ion populations close to their border areas.

The second stage featured a measurement for each group, isolated by the MRS, after 10 turns. Each of these measurements was calibrated with assigned M_1 fragments. The intermediate MRP of 10 000 and mass accuracy of 10 ppm allows the script described in Section 4.8 to predict their position in a spectrum after a given number of turns. In reverse, the script proposes a setting for the third stage, in which no signal overlaps or is close to fringe fields in the analyzer. The measurements required for the second stage took around 15 minutes per precursor signal.

The measurements of the third stage are typically acquired at a turn number between 300 - 500, depending on the script's suggestion. All mass lines within a group appear within the same spectrum, but with up to 20 different turn numbers. Using identified fragments of M_1 to calibrate during a measurement yields an MRP of over 250 000 and a mass accuracy of better than 1 ppm. However, since the number of passed turns is ambiguous, each possible turn number produces a candidate with its mass-to-charge ratio. Only by comparison with the second stage measurement, using the script for predicting a given molecule's position in the spectrum, and the TOFControl software's peak identification (see Section 4.6), can the turn number and the mass-to-charge ratio be determined. Depending on the precursor molecule's abundance, acquiring enough statistics for the third stage required 20 - 40 minutes per group, resulting in a total measurement time of 2 - 5 hours per precursor signal.

6.2.6 Data Analysis

After acquiring accurate mass-to-charge values, the TOFControl software was utilized to identify and assign elemental compositions. Only signals that could be assigned to elemental compositions with a deviation of less than 1 ppm were considered identified and further analyzed. Compositions with unlikely cleavages for this level of CID, like a nitrogen cleavage, or a loss of multiple carbon atoms without losing hydrogens were also discarded. The analysis of the structural information was performed by the WG Schrader after sending them the list of identified elemental compositions, mass-to-charge values, and detected abundances of the precursor signals labeled M_1, M_2, M_3, and M_4.

The analysis focused on fragments with high abundance and used their elemental composition and DBE value as a basis for possible fragmentation pathways. Theoretical structural formulas were devised from measured elemental compositions and assumed to result from known fragmentation processes as described in Section 2.10. Then their intermediate precursor molecules were determined, and the resulting fragmentation pattern was compared to the measured mass spectrum of the fragments.

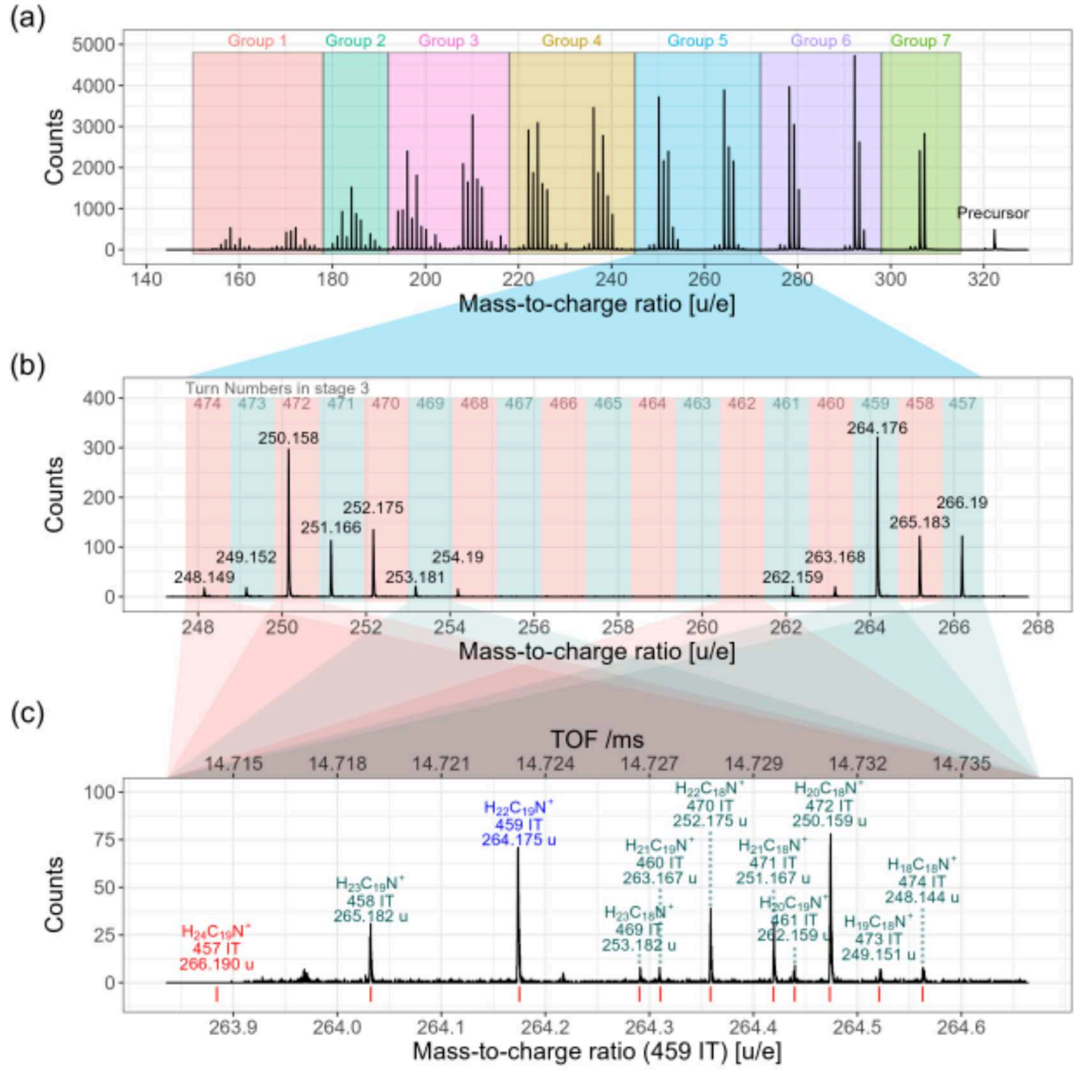

Figure 6.2.7: Three stages of the turn deconvolution procedure for the fragments of the M_1 precursor molecule.
(a) First stage: An overview spectrum is acquired after a single IT (TOF=78 µs) with an MRP of 3000 and thus low mass accuracy of 60 ppm. The spectrum is segmented into seven groups (indicated by color), for each of which the second stage is executed.
(b) Second stage: A mass spectrum of the chosen segment is acquired again at a higher turn number of 10 IT (TOF=0.4 ms), an MRP of 10 000 and a mass accuracy of 10 ppm. This is the highest achievable MRP for this group of ions while keeping the mass range unambiguous. Mass resolving power and mass accuracy are now high enough to calculate the TOF of each fragment in the third stage. Each colored section refers to a mass range, which overlaps in the mass spectrum of the third stage with the listed turn number on top.
(c) Third stage: The mass spectrum with high MRP (250 000) and mass accuracy (better than 1 ppm). The spectrum is composed of the 18 mass ranges shown in the second stage spanning from 474 - 457 IT with a TOF of 14.7 ms (shown in the upper abscissa). The displayed abscissa refers to the turn number of 459 IT. Labels show a signal's identified elemental composition, turn number, and measured mass. The molecule's literature mass is marked below in red. Ions with a TOF below 14.717 ms, like the red labeled on at 266.19 u/e, were inside the analyzer mirror during the potential switch for ejection and required a second measurement with adjusted parameters to be observed.

It was possible to gain the following structural information only thanks to the unprecedented mass separation power of the MR-TOF-MS in this work. Not only did this prevent the fragmentation patterns from overlapping, but also allowed the identification of each fragment's constituent atoms by its mass-to-charge ratio.

6.3 Fragmentation Spectra

Figure 6.3.1 shows the reconstructed mass spectra for the fragments of M_1, M_2, M_3, and M_4 of the over 500 fragment data gained from turn deconvolution. Each entry in this plot corresponds to an identified elemental composition, which was determined from the mass-to-charge ratio measured with the turn deconvolution procedure. Compared to Figure 6.2.6 where the raw acquired data without identification is shown, most of the prominent signals were identified.

In the following, the acquired results from Section 6.2.5 are shown in Kendrick mass defect plots (see Section 2.8) to depict the double bond equivalent (DBE) against the carbon atom number, which indicates reoccurring fragmentation processes (see Section 2.9). Both plots depict the data with point radii proportional to detected abundance and colors chosen according to functional groups.

Fragments of M_1 ($C_{23}H_{32}N$)

Figure 6.3.2 shows a KMD plot of the fragments of the M_1 labeled molecule ($C_{23}H_{32}N$). The precursor molecule's composition of only hydrogen, carbon, and nitrogen atoms creates a clear pattern that indicates a frequent severing of CH_2 and hydrogen, while all fragments contain nitrogen. The most abundant fragments form a pattern of missing alkyl groups $(CH_2)_n$+CH_3 of different lengths n down to the molecule $C_{12}H_9N$ with a mass value of 167 u. However, the wide range of amounts of hydrogen atoms in the most abundant mass lines implies more complex structures.

The DBE plot in Figure 6.3.3 shows that the most abundant fragments lie within a DBE region of 8.5 to 10. Since the precursor molecule has a DBE value of 9, mostly fragmentation processes with a DBE change of -0.5 to 1.5 will be considered.

6.3.1 Fragments of M_4 ($C_{22}H_{28}ON^+$)

The KMD plot of fragments of the molecule M_4 ($C_{22}H_{28}ON^+$) in Figure 6.3.4 and DBE plot in Figure 6.3.5 show patterns that can be divided into two equally large groups of fragment ions, one of which contains one oxygen atom and the other of which does not contain oxygen.

The pattern for fragments that do contain oxygen continues until C_{12}, while the pattern for oxygen-free fragments continues to C_{11}, suggesting molecule structures of isomers in the precursor molecule with the oxygen contained in a severable sidearm. The fragment $C_{22}H_{26}N$ with a mass value of 304 u dominates the detected ion abundance, indicating the oxygen is prone to get severed. The DBE plot in Figure 6.3.5 suggests fragmentation processes that change the DBE value from 9.5 of the precursor molecule mostly by 1 for isomers with the oxygen atom in a sidearm and by -1 to 1 for isomers, where CID does not sever the oxygen.

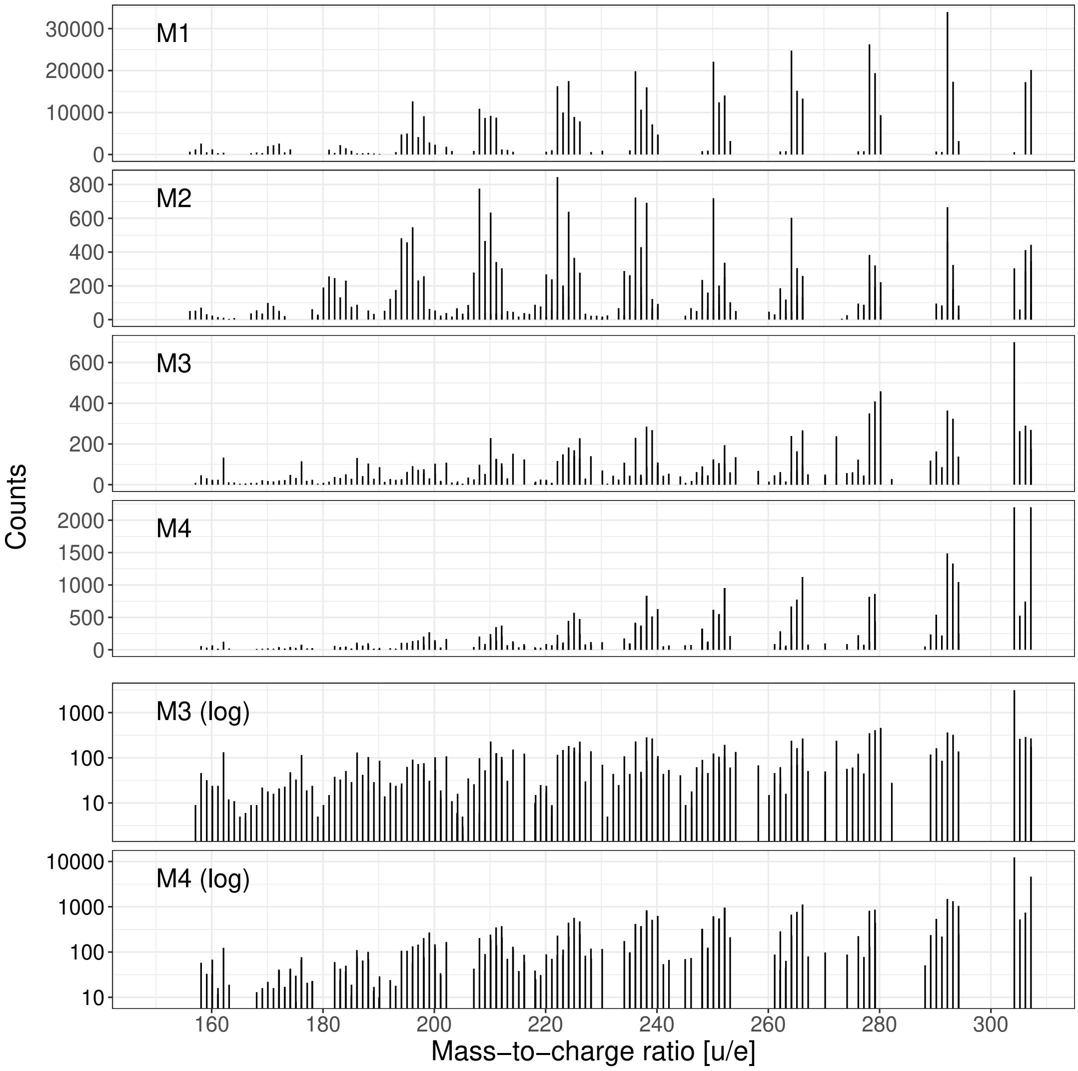

Figure 6.3.1: Resulting mass spectrum of the turn deconvolution procedure for the fragments of the precursor molecules listed in Table 6.3. Most mass spectra of the third stage were acquired after a TOF of 17 ms and turn numbers within 300 - 500 IT. An MRP of 200 000 with a mass accuracy of 1 ppm was achieved. The data of M_3 and M_4 is each shown once in logarithmic scale and once in linear scale with the intense signal at 304 u/e cropped to improve visibility of the less abundant lighter clusters.

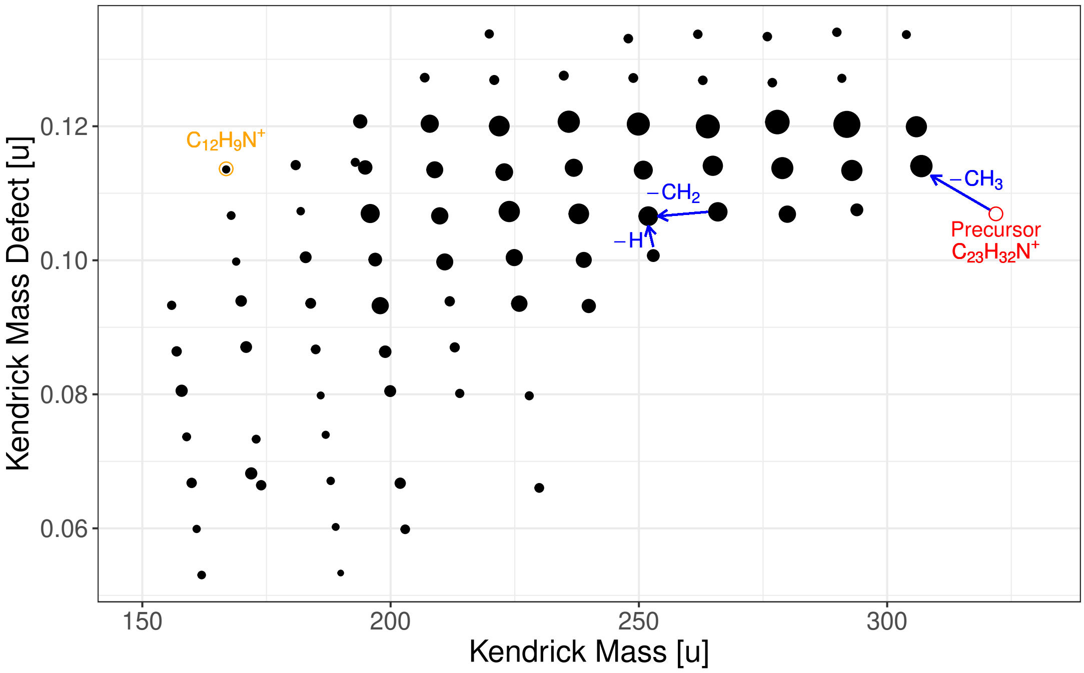

Figure 6.3.2: Kendrick mass against Kendrick mass defect for fragments of M_1 ($C_{23}H_{32}N$). Molecules displayed in a horizontal line differ in amounts of CH_2 adducts, while slanted vertical lines differ in amounts of H. Point radii are proportional to the abundance of fragment ions. Since $C_{23}H_{32}N$ contains atoms of only three different elements with a strongly bound N, the fragments form a clear, grid-like pattern. The most abundant fragments are close to the path of separated alkyl chains $(CH_2)_n{}^+CH_3$ of different lengths n from the precursor molecule down to $C_{12}H_9N$.

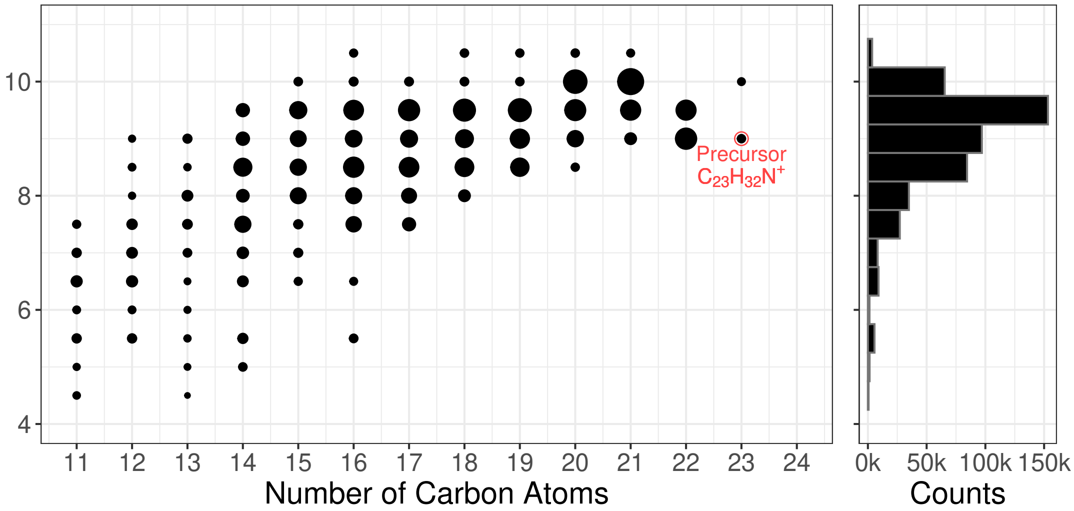

Figure 6.3.3: DBE Plot of M_1 ($C_{23}H_{32}N$) fragments with a DBE histogram to the side. Point radii are proportional to the fragment abundance. The histogram shows the sum of the abundances of all molecules with the same DBE value.

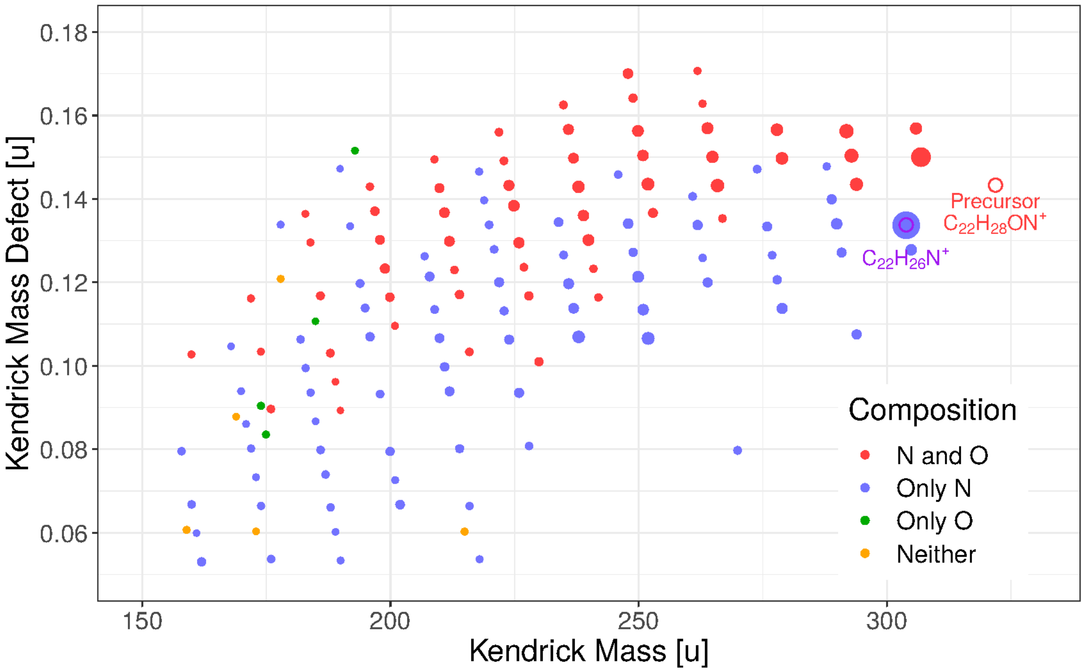

Figure 6.3.4: Kendrick mass against Kendrick mass defect for fragments of M_4 ($C_{22}H_{28}ON^+$). Molecules displayed in a horizontal line differ in the number of CH_2 adducts. Point radii are proportional to fragment abundance. $C_{22}H_{28}N$ is a fragment of very high abundance, which suggests a stable structure. The groups with and without oxygen are similar in total abundance and expansion, suggesting a mixture of isomers in the precursor signal where oxygen is in a sidearm or within the molecule core.

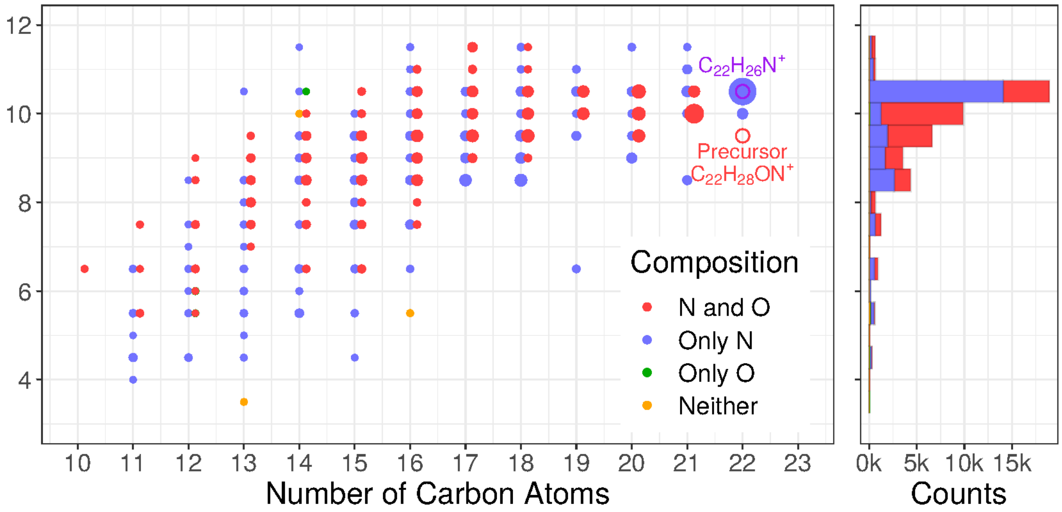

Figure 6.3.5: DBE Plot of M_4 ($C_{22}H_{28}ON^+$) fragments with a stacked DBE histogram to the side. Point radii are proportional to the fragment abundance. The stacked histogram width shows the sum of abundances for all molecules with common DBE values. The pattern of oxygen-containing fragments is slightly shifted horizontally to avoid overlapping.

6.3.2 Fragments of M_2 ($C_{21}{}^{13}C_2H_{30}N^+$)

The plot shown in Figure 6.3.6 displays the KMD plot of the fragments of the molecule M_2. This precursor signal is likely composed of $C_{21}{}^{13}C_2H_{30}N^+$ (322.243 99 u/e), but also may contain $C_{19}H_{34}N_2S^+$ (322.243 72 u/e), which can not be resolved with the available resolving power. The distinctive atoms in both molecules, ^{13}C and S, serve as markers to assign the detected fragments to a specific precursor molecule, since their cleavage is improbable. The S-atom is typically strongly bound, while cleavage of the ^{13}C-isotope is statistically low. In addition, a closer look into the KMD plot reveals a large portion of molecules already observed in M_1. While the isolation spectrum in Figure 6.2.5 implies mostly clean isolation, the resemblance to the fragment spectrum of M_1 is an indicator for a voltage drift which shifted the re-trapping window closer to the highly abundant M_1 precursor signal during the measurement. Due to the uncertainty of the fragment's origin and the overlapping patterns, the structural information was not analyzed further.

In order to distinguish the fragments of M_2, the KMD plot uses colors to distinguish fragments containing two, one, or no ^{13}C atoms. The patterns of one and two ^{13}C atoms lead down to C_{15} (209 u), while the pattern without ^{13}C atoms reaches lower (C_{11}) and shows a high similarity to M_1. The fragments without ^{13}C atoms pose 76 % of the total abundance, while 9 % comes from fragments with one ^{13}C atom and 16 % from fragments with two ^{13}C atom.

The DBE plot in Figure 6.3.7 of the fragments of M_2 also suggests that most fragments without ^{13}C atoms originate from M_1. Their pattern and dominant DBE value of 9.5 are close to the one of M_1 shown in Figure 6.3.3. The fragments with one or two ^{13}C atoms both show DBE changes of 0 - 1 compared to the DBE value of the precursor molecule of 9.5.

6.3.3 Fragments of M_3 ($C_{17}{}^{13}CH_{34}OSNa^+$)

Due to its complex composition with ^{13}C, oxygen, sulfur, and sodium, the pattern of the M_3 molecule ($C_{17}{}^{13}CH_{34}OSNa^+$, 322.225 61 u/e) fragments is rather complex. Furthermore, a different molecule, $C_{22}{}^{13}CH_{29}O$ (322.224 65 u/e), might be a component of the isolated precursor signal, since the resolving power is too low to properly resolve the molecules. As with M_2, there is also again a chance that the isolation window shifted due to voltage drifts and, thus, contaminated the fragment spectrum with fragments of the neighboring signal, which, in this case, is M_4.

The KMD plots shown in Figure 6.3.8 display an attempt at assigning the identified fragments to the possible precursor molecules. The first plot (a) identifies fragments that contain a nitrogen atom and, thus, likely originate from the neighboring precursor signal M_4. The fragments without nitrogen are further divided in the second plot (b) by whether they contain a ^{13}C isotope, which has a statistically low chance of being severed during fragmentation. Fragments that fulfill both conditions are shown in plot (c) and colored by the remaining distinctive atoms of oxygen, sodium, and sulfur. However, due to the overlap of the assumed precursor molecule $C_{17}{}^{13}CH_{34}OSNa^+$ with $C_{22}{}^{13}CH_{29}O$ and M_4, and the complex composition of fragments, which shows few characteristic patterns, there was no further analysis of structural information of the precursor molecule M_3.

Fragments of the precursor molecule M_4 are also visible in the DBE plot of the fragments of M_3 shown in Figure 6.3.9. The dominant fragment $C_{22}H_{26}N^+$ and the prevalence of DBE values at 10.5 are similar to the DBE plot of M_4 in Figure 6.3.5.

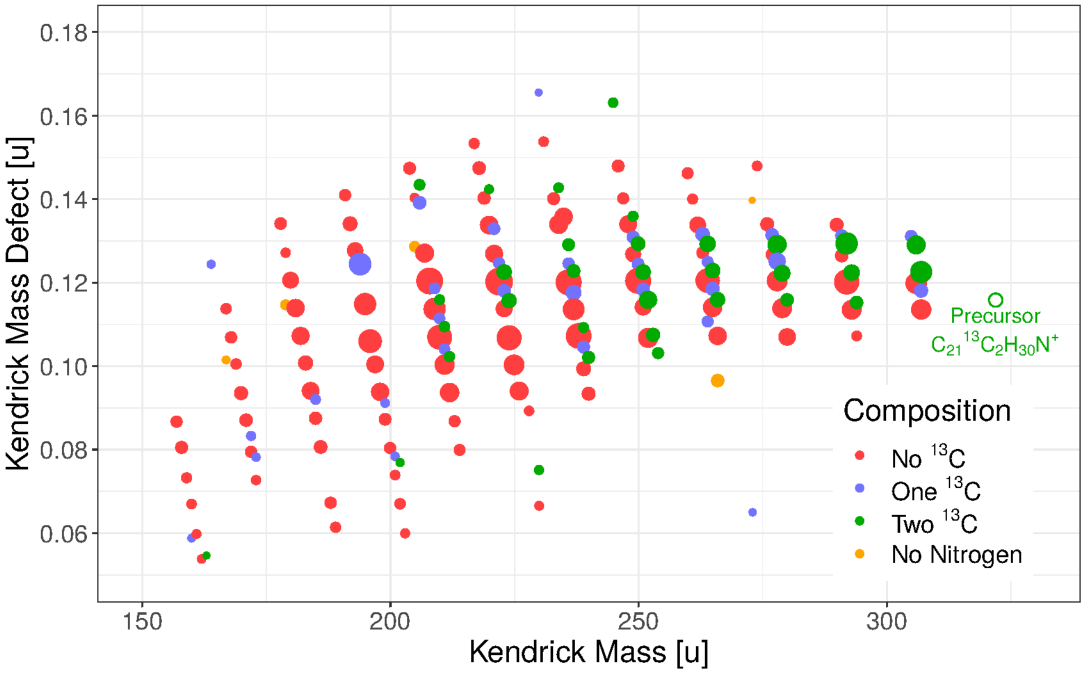

Figure 6.3.6: Kendrick mass against Kendrick mass defect of M_2 ($C_{21}{}^{13}C_2H_{30}N^+$). Molecules displayed in a horizontal line differ in amounts of CH_2 adducts. Point radii are proportional to fragment abundance. Points of nitrogen-containing fragments are colored according to the number of ^{13}C and nitrogen atoms they contain.

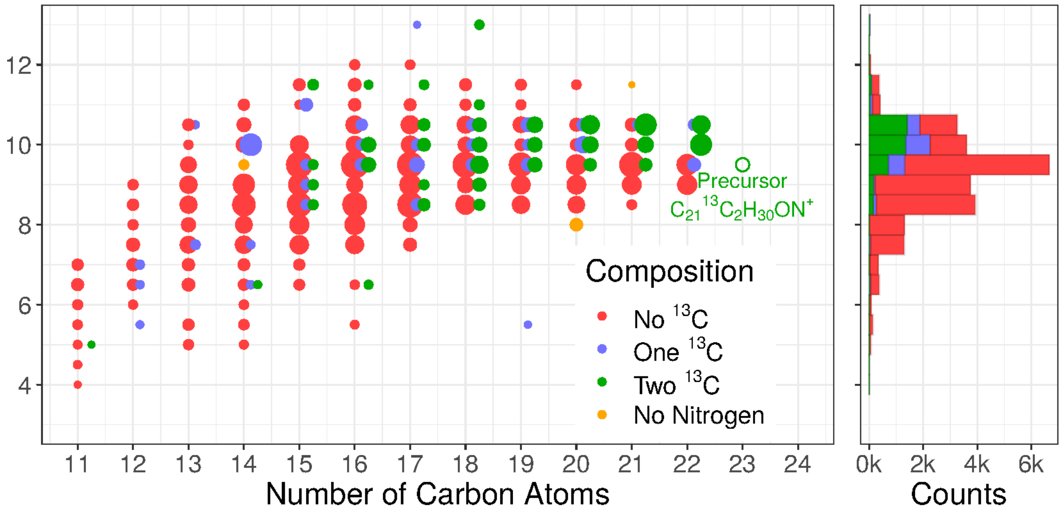

Figure 6.3.7: DBE Plot of M_2 ($C_{21}{}^{13}C_2H_{30}N^+$) fragments with a stacked DBE histogram to the side. Point radii are proportional to the fragment abundance. The stacked histogram width shows the sum of abundances for all molecules with common DBE values. Point color refers to whether molecules contain ^{13}C. Points are shifted horizontally depending on their color to improve visibility. The ^{13}C-free pattern has a strong resemblance to the DBE plot of M_1 fragments (see Figure 6.3.3).

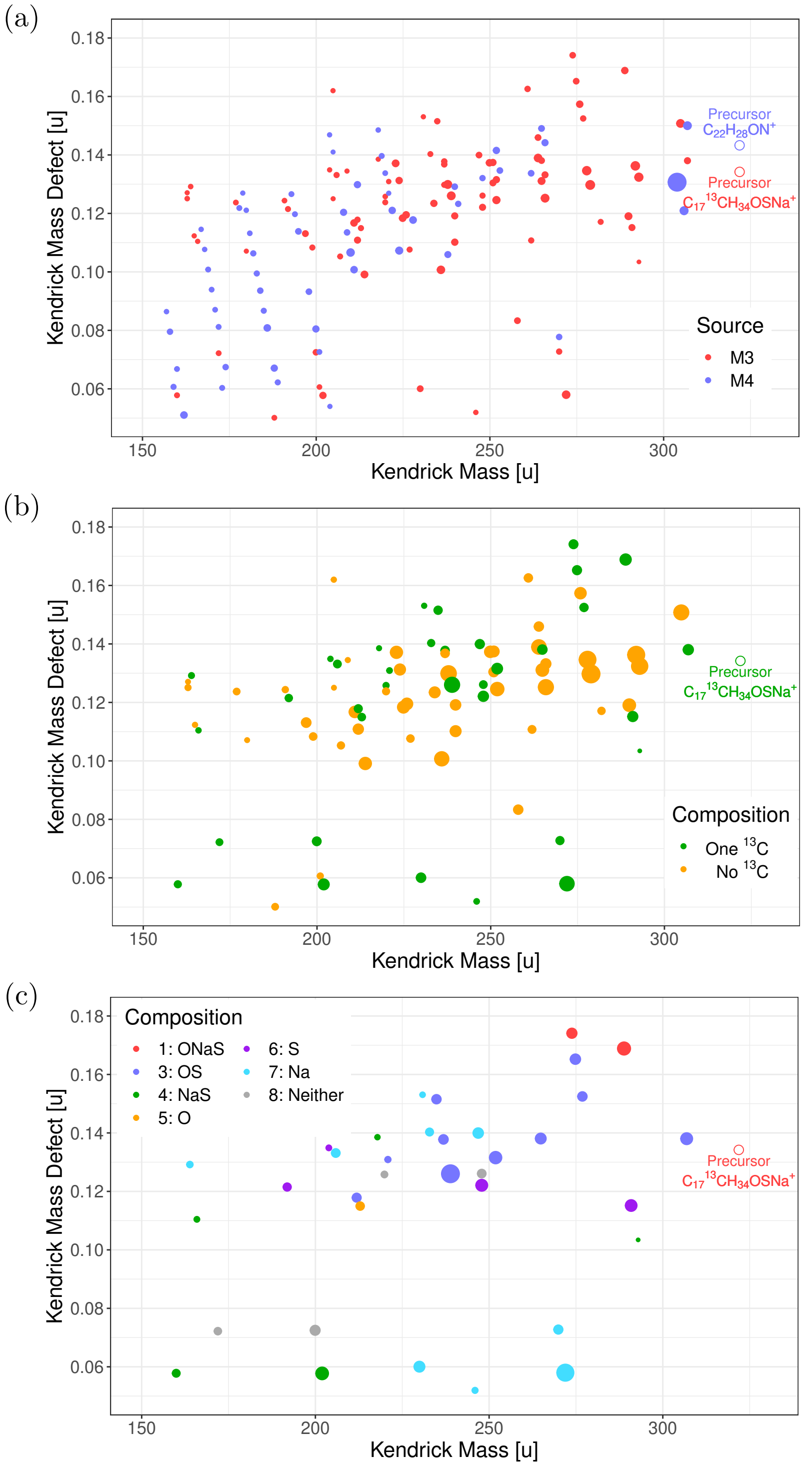

Figure 6.3.8: Visualization of Kendrick mass (abscissa) against Kendrick mass defect (ordinate) of M_3 ($C_{17}\,{}^{13}CH_{34}OSNa^+$). Molecules displayed in a horizontal line differ in the number of CH_2 adducts. Point radii are proportional to fragment abundance. Due to contamination with fragments originating from M_4, a three-stage filter approach is used.

(a) Contamination with nitrogen-containing fragments originating from M_4.
(b) The nitrogen-free fragments are further categorized according to whether they contain a ${}^{13}C$ atom like the precursor molecule.
(c) The nitrogen-free fragments with a ${}^{13}C$ atom likely originate from M_3.

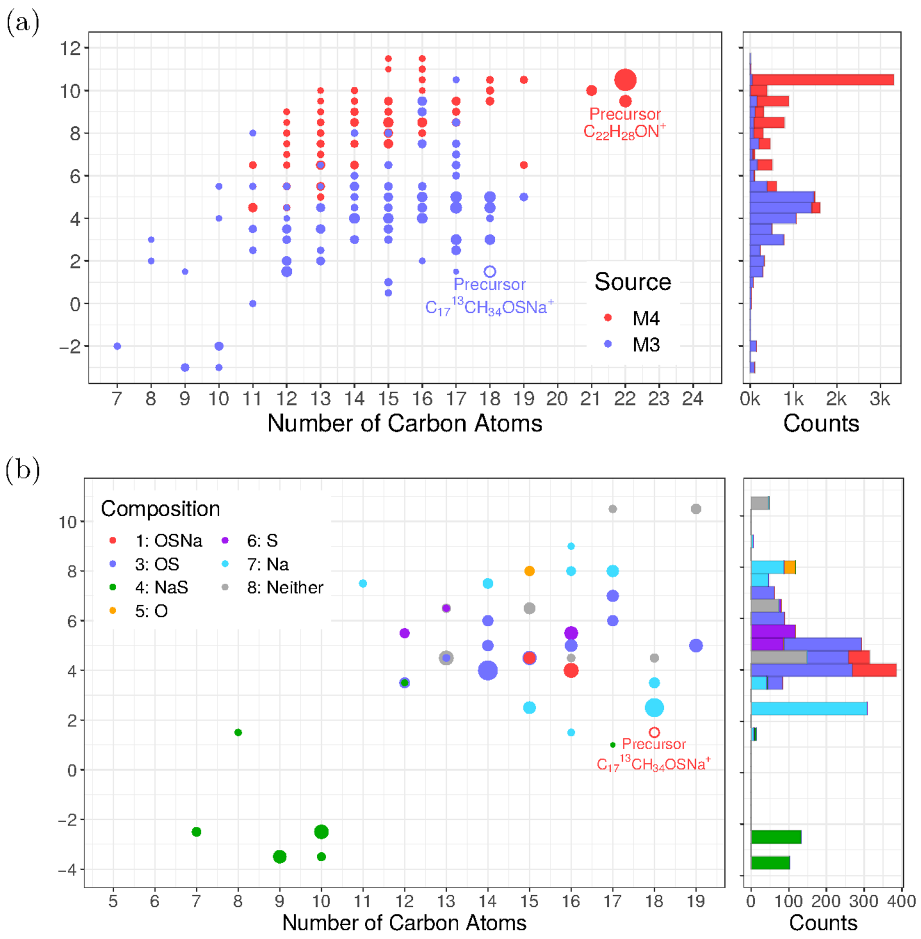

Figure 6.3.9: DBE Plot of M_3 ($C_{17}\,{}^{13}CH_{34}OSNa^+$) fragments with a stacked DBE histogram to the side. Point radii are proportional to the fragment abundance. The stacked histogram width shows the sum of abundances for all molecules with common DBE values. Molecules of different colors are slightly shifted horizontally to improve visibility.
(a) Contamination with M_4 fragments
(b) M_3 fragments with ${}^{13}C$ and without nitrogen divided into compositions by color.

The remaining fragments without nitrogen possess DBE values mostly within 1.5 - 5, which differ strongly from the range 8.5 - 10.5 of the fragments of M_4. The DBE change of 0 - 3.5 also indicates different fragmentation processes and thus a different prevalent molecular structure for the isomers in M_3.

6.4 Comparison with an FTMS for Fragments of precursor M_1

To demonstrate the challenge and reliability of the system, the WG Schrader shared data from a measurement of the same sample. Ions in the mass spectrum shown in Figure 6.4.1 were produced with an Atmospheric Pressure Photo Ionization (APPI), where a vacuum-UV-Kr-lamp is set to produce photons at 10.0 eV and 10.6 , and acquired with the 7T LTQ FT-ICR-MS device from Thermo Fisher Scientific in Bremen, Germany. The recorded mass spectrum has a resolving power above 500 000, which allows to better estimate the molecules that compose M_1 to M_4 in Figure 6.2.4.

Due to the dominating abundance of the nitrogen-containing precursor molecule

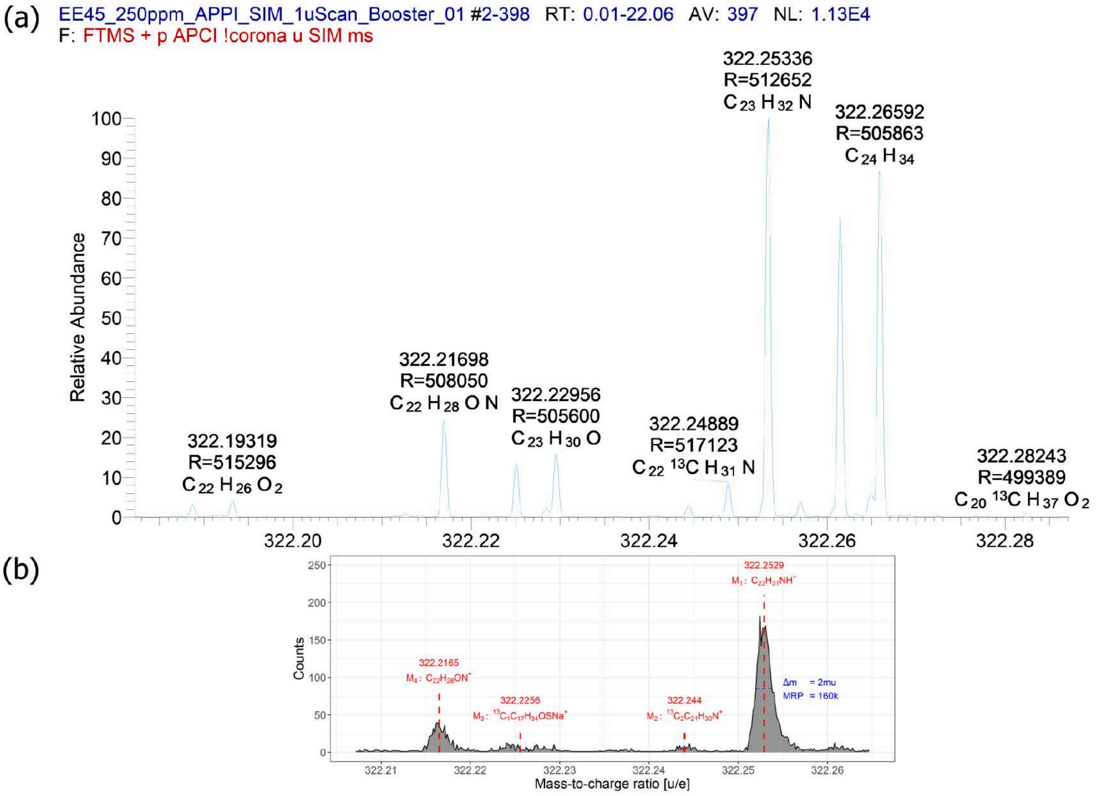

Figure 6.4.1: (a) Mass spectrum of the medium-heavy crude oil sample acquired with an 7T LTQ FT-ICR-MS from Thermo Fisher Scientific, Bremen, Germany. A vacuum UV Kr lamp was used with an photons of 10.0 eV and 10.6 eV.
(b) shows Figure 6.2.5 scaled to have same mass scale aligned to the plot above.

M_1, the workgroup was able to acquire a mass spectrum of fragment molecules that were deduced to stem from M_1 as well, but not from M_2 to M_4. The spectra of the WG Schrader were acquired with an ESI ion source operated at 4 kV and a resolving power R= A comparison with the mass spectrum acquired in this work is shown in Figure 6.4.2.

The mass spectra of the two devices show high similarities with most fragment molecules contained in both plots with similar abundances. The mass spectrum acquired in this work shows an additional population of molecules with a mass-to-charge range within 150 - 200 u/e, a higher abundance of molecule groups within 200 - 260 u/e and a more dominant abundance of the first prevalent molecule in each group ($C_{17}H_{18}N, C_{18}H_{20}N, C_{19}H_{22}N, C_{20}H_{24}N, C_{21}H_{26}N, C_{22}H_{28}N$). These differences are likely caused by higher collision energy, which also explains the absence of the precursor ion at 322.253 u/e. However, the similarity of both spectra demonstrates that the device can reliably replicate CID fragment spectra in addition to its high precursor separation power. The comparison in Figure 6.4.3 shows a zoomed section of the plots in Figure 6.4.2, where also all fragments of higher abundance were detected by both deviced. Here, the device of this work shows an additional signal of $C_{19}H_{21}N^+$, likely due to the higher CID energy. The spectrum of the FT-ICR-MS of the WG Schrader shows a lot of smaller signals with a relative abundance lesser than 2 %. Their absence in our spectrum is easily explained by the data analysis process, where only signals of higher abundance were investigated and, thus, appear in the reconstructed spectrum.

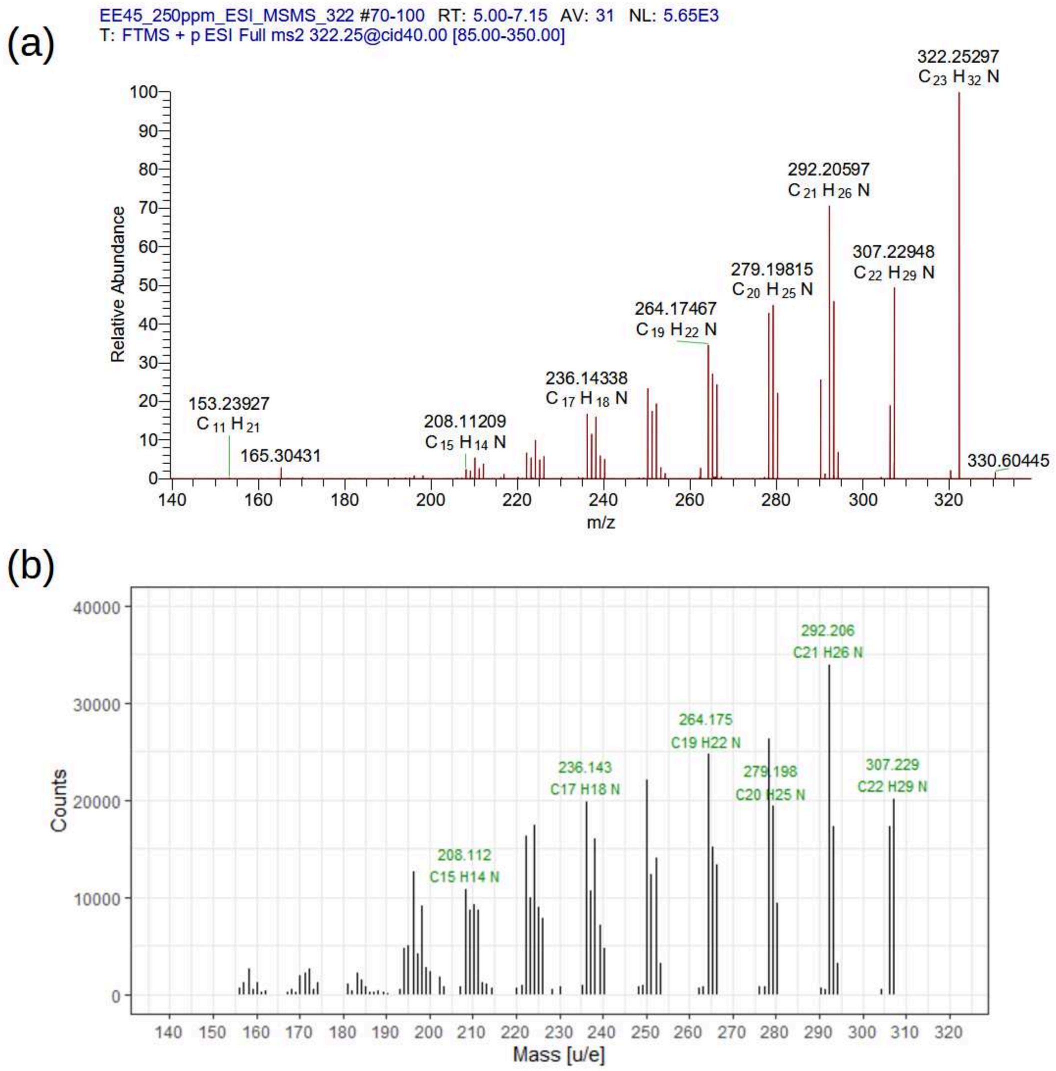

Figure 6.4.2: Comparison between measurements of the medium-heavy crude oil sample by the WG Schrader (a) and the data acquired in this work (b). The ions of the spectrum acquired by the WG Schrader were produced using an ESI ion source at 4 kV in positive mode and data data acquired with an 7T LTQ-FTICR-MS from Thermo Fisher Scientific, Bremen, Germany. The plots are horizontally aligned to share the same mass-to-charge axis.
The two devices detect mostly the same molecules with similar abundances while our device shows a larger abundance of lighter molecules, likely due to a higher CID energy.

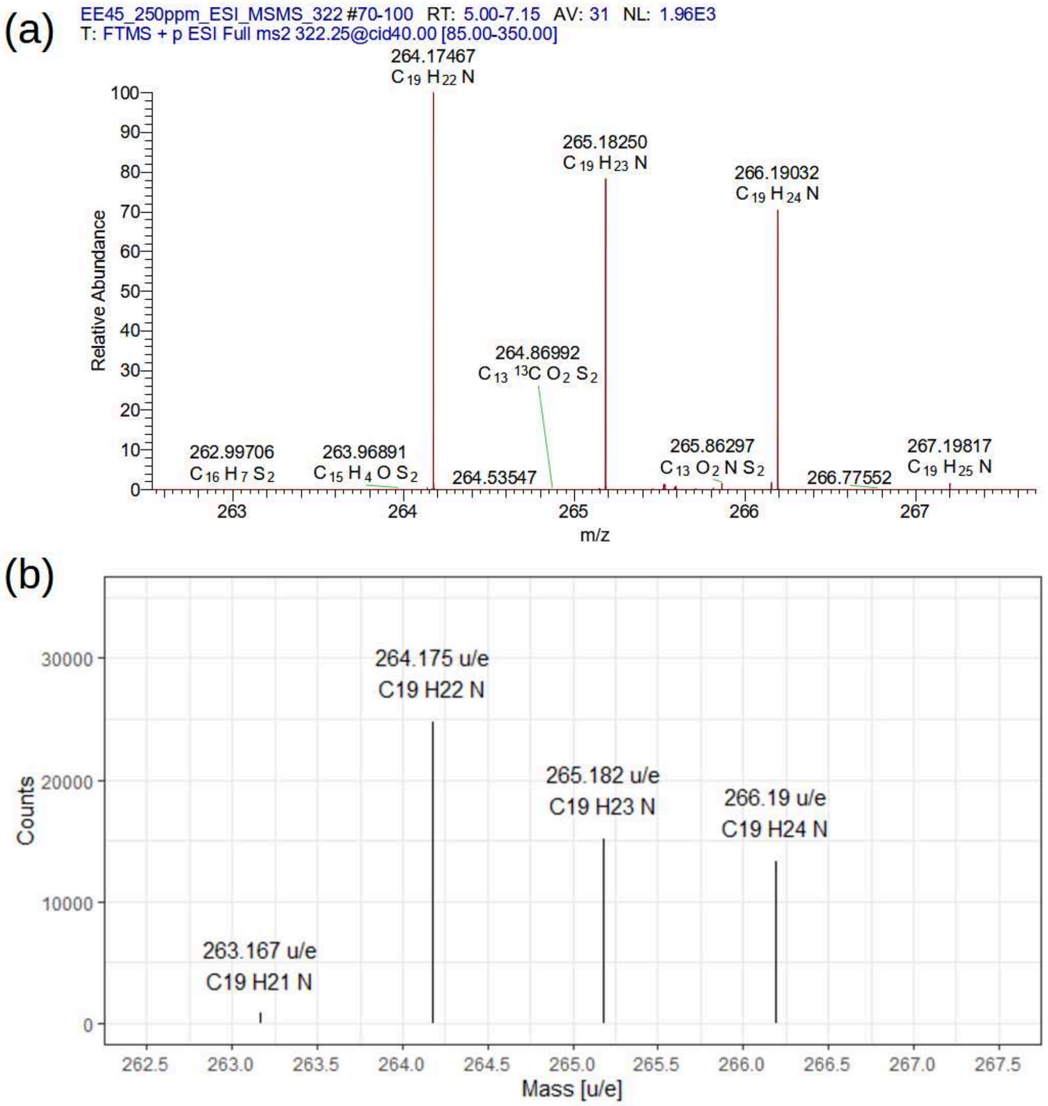

Figure 6.4.3: Comparison between measurements of the medium-heavy crude oil sample by the WG Schrader (a) and the data acquired in this work (b). The ions of the spectrum acquired by the WG Schrader were produced using an ESI ion source at 4 kV in positive mode and data data acquired with an 7T LTQ FT-ICR-MS from Thermo Fisher Scientific, Bremen, Germany. The plots are horizontally aligned to share the same mass-to-charge axis.
This plots shows a zoom into the mass-to-charge range of 262 - 268 u/e. Both plots show the abundant fragments with similar abundance ratios. Differences can be observed in the low abundance fragments, where a CID energy lead to a small signal of $C_{19}H_{21}N$ in (b), while the FT-ICR-MS produced spectrum in (a) shows more fragments below 2 % relative abundance. Only signals of high abundances were analyzed in the third stage of the turn deconvolution process described in Section 6.2.5 to simplify the analysis, leading to the absence of low-abundance signals in plot (b).

6.5 Identified Structures

The information collected in the previous chapters was analyzed by the WG Schrader. The data of the precursor signals M_2 and M_3 did not yield satisfying results due to the precursor molecule's ambiguous composition and complex fragmentation pattern. However, the data of the cleanly isolated precursor molecules M_1 and M_4 enabled the identification of multiple new molecular structures.

6.5.1 Structures of M_1 ($C_{23}H_{32}N$)

The structural elucidation process of M_1 is demonstrated by the two isomeric molecular structures (a) and (b) shown in Figure 6.5.1. Once a candidate is found, its possible fragmentations and variations are estimated and the mass values for the resulting fragments are calculated. Variations include a deviating number or length of alkyl chains, while cleavage at different positions within an alkyl chain is improbable [VETERE et al. 2018]. This list of predicted fragments is then compared with the list of measured mass values and their suspected molecular compositions. If most of the predicted fragments have matches with high abundance, the molecular structure is likely part of the precursor signal's composition.

The fragments likely produced by the two structures shown in Figure 6.5.1 (a) and (b) are marked in the measured mass spectrum shown in Figure 6.5.2. The predicted patterns are contained well within the measured spectrum, implying that the assumed base structures and variations in their alkyl chains are likely contained within the M_1 precursor molecule signal.

Further investigation yielded the list of ten more identified isomeric structures depicted in Figure 6.5.3 with their fragmentation process. The structure appears to be dominated by carbazoles due to the DBE change of +0.5/+1 and the prevalence of sigma bond cleavage in alkylated aromatic systems. Amines are also likely present due to fragmentation processes outside their ring structure. However, carbazoles are more likely to dominate since no long-chained alkyl groups exist.

Fragments with a DBE change of +1.5/+2 are challenging to explain with known fragmentation processes. While their formation is also observed in experiments in other commercially available devices, they are likely the product of a chain reaction of multiple fragmentations during the CID exposition time of 10 ms.

6.5.2 Structures of M_4 ($C_{22}H_{28}ON$)

Due to its isobaric dominance, the fragmentation pattern of the prevalent M_1 precursor signal can already be analyzed in commercially available devices with less mass separation power, since it does not need to be isolated from the other isobars. However, investigating the fragmentation pattern of the M_4 precursor molecule $C_{22}H_{28}ON^+$ isolated from M_1 is only possible due to the capabilities of this device.

The structural elucidation of M_4 follows the same workflow as described for M_1. Two candidates for existing molecular structures within the precursor signal are listed in Figure 6.5.4 (a) and (b) with possible fragments and variations in their alkyl chains listed in (c) and (d), respectively. The comparison with the measured spectrum in Figure 6.5.5 shows again a good match to the predicted fragments, making both structures likely components of the precursor signal M_4.

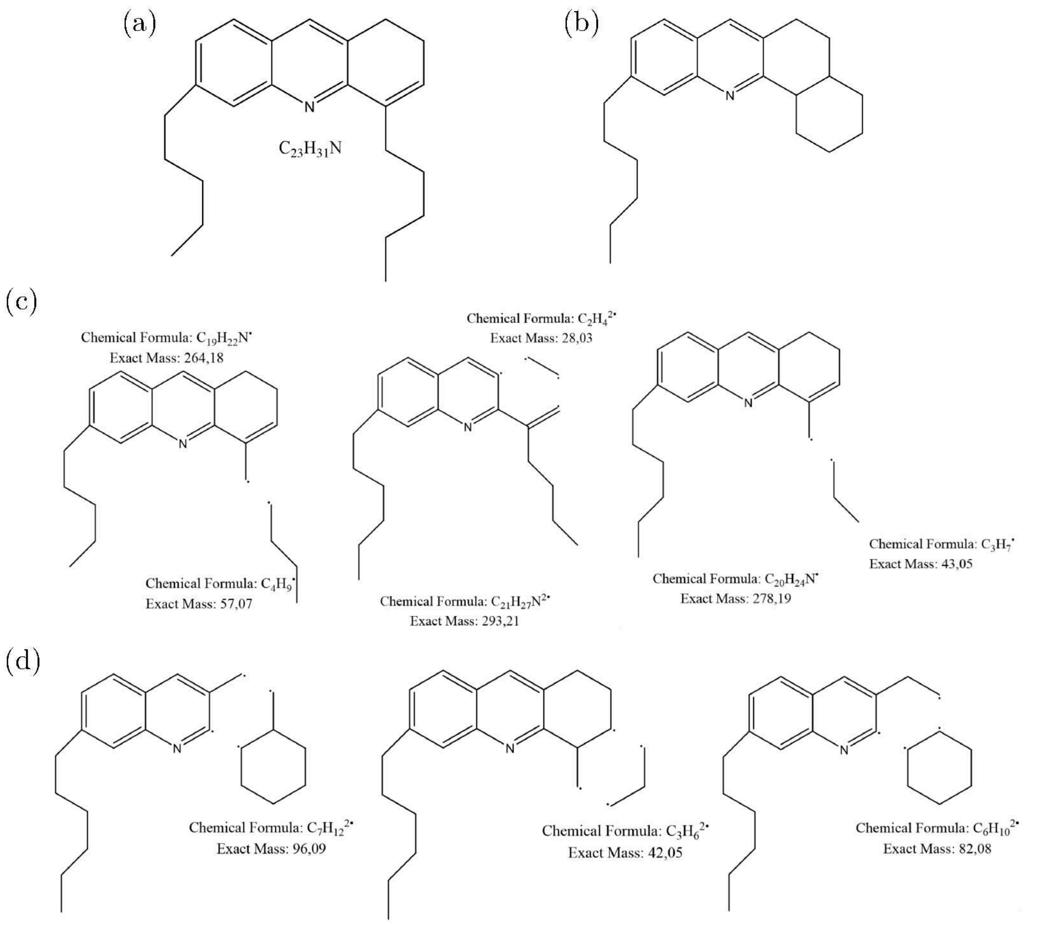

Figure 6.5.1: Two candidate isomeric molecular structures (a) and (b) for the precursor molecule M_1 and examples for their respective fragmentation processes and variations (c) and (d) for (a) and (b), respectively.

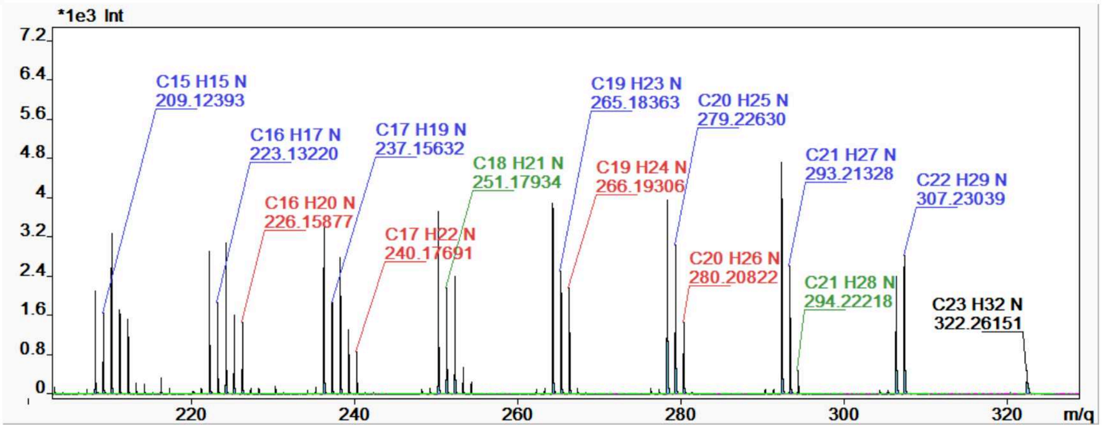

Figure 6.5.2: Measured mass spectrum of M_1. The fragment molecules originating from the structures shown in Figure 6.5.1 (c) and (d) are labeled with their elemental composition and mass-to-charge value in u/e. Blue labels are related to structure (a) and red labels relate to structure (b). Green labels can be produced by both structures. The black label marks the precursor molecule.

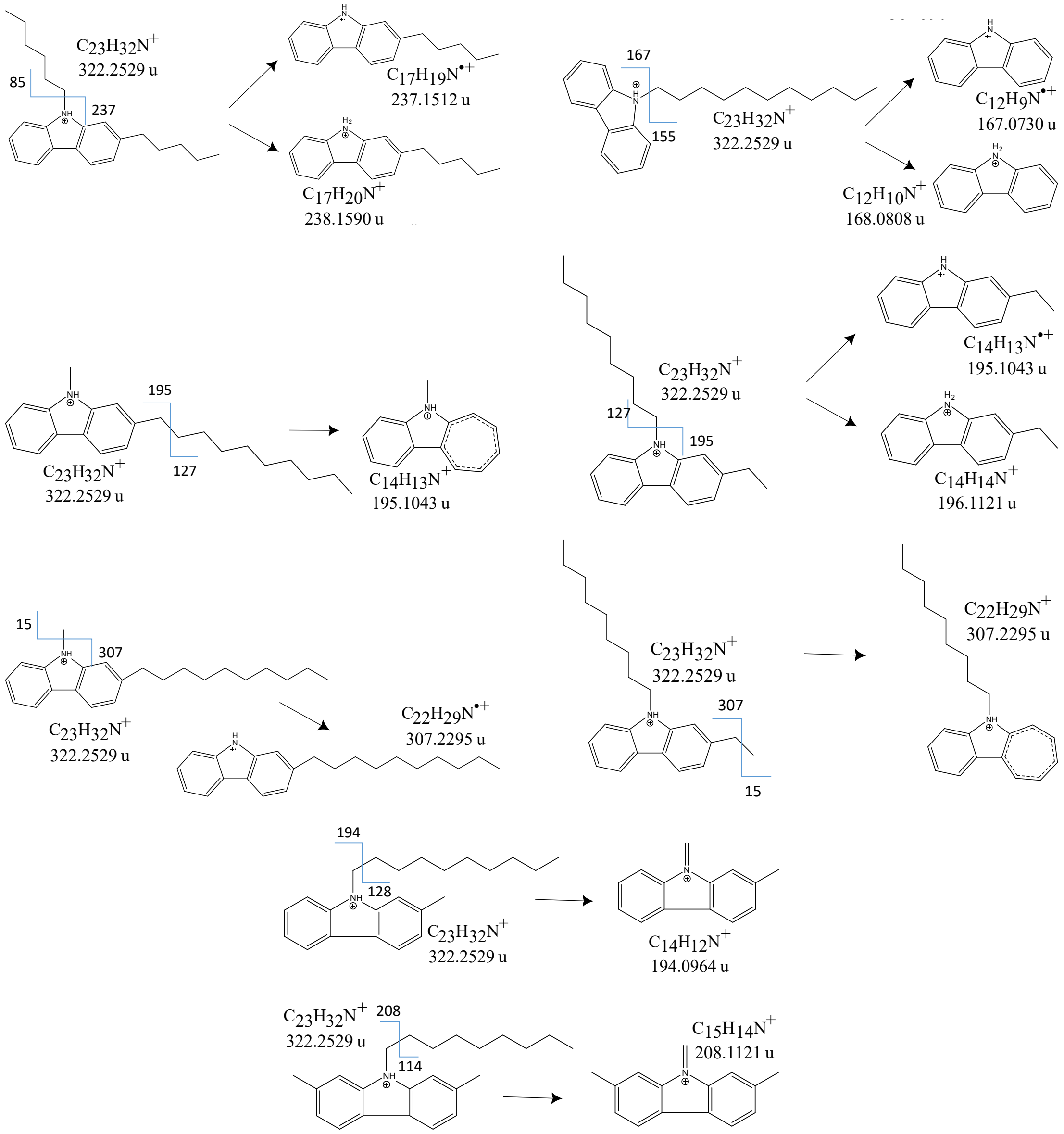

Figure 6.5.3: Identified structures formulas for the M_1 molecule $C_{23}H_{32}N^+$, fragmentation processes and measured fragments. Structural formulas derived by Jens Dreschmann from the WG Schrader.

A repeated loss of ethene indicates a dominance of alkyl groups within the M_4 isomers. This led to several structures depicted in Figure 6.5.6, which were confirmed to match with acquired data. Furthermore, archipelago-type structures, where a carbon chain connects two carbon ring groups, were confirmed by detecting the fragmented half which is carrying the charge after the carbon ring was severed. In total, sixteen likely structural formulas that contribute the the M_4 precursor signal, were identified.

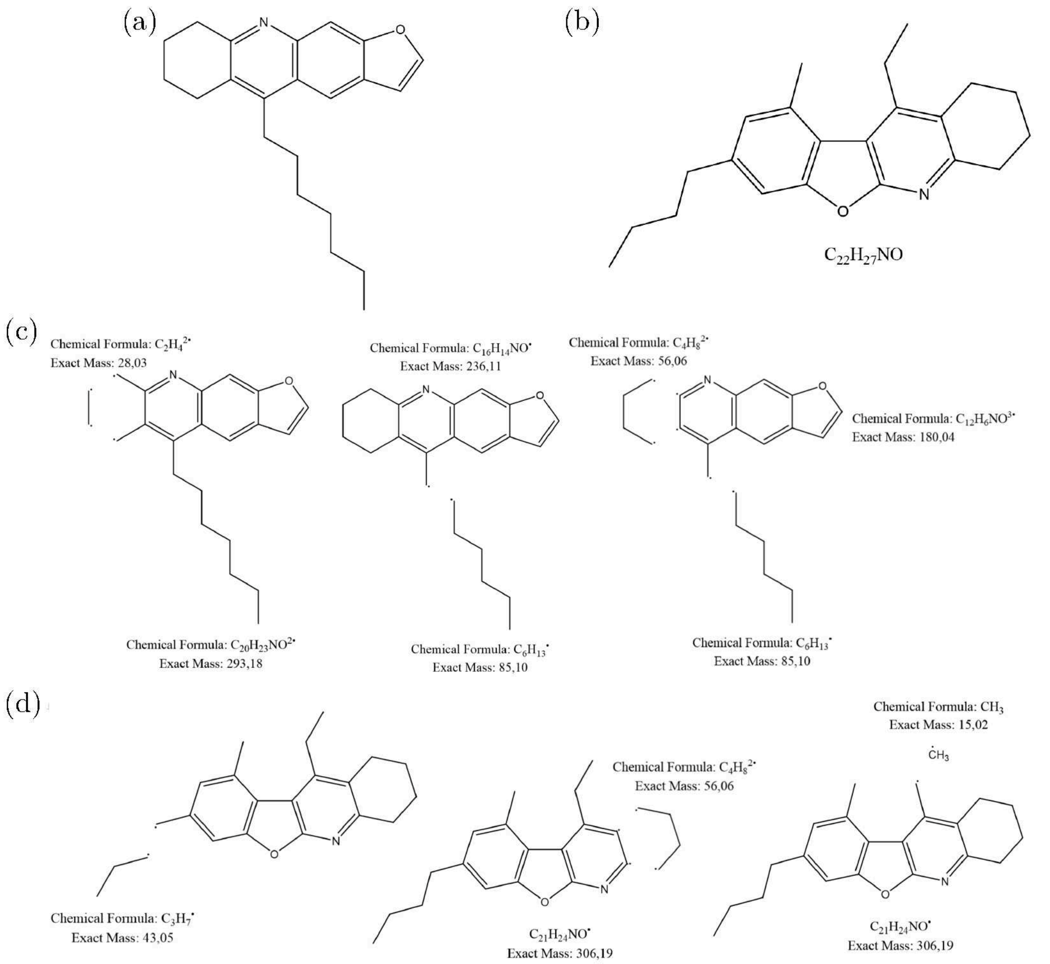

Figure 6.5.4: Two candidate isomeric molecular structures (a) and (b) for the precursor signal M_1 and examples for their respective fragmentation processes and variations (c) and (d) for (a) and (b), respectively.

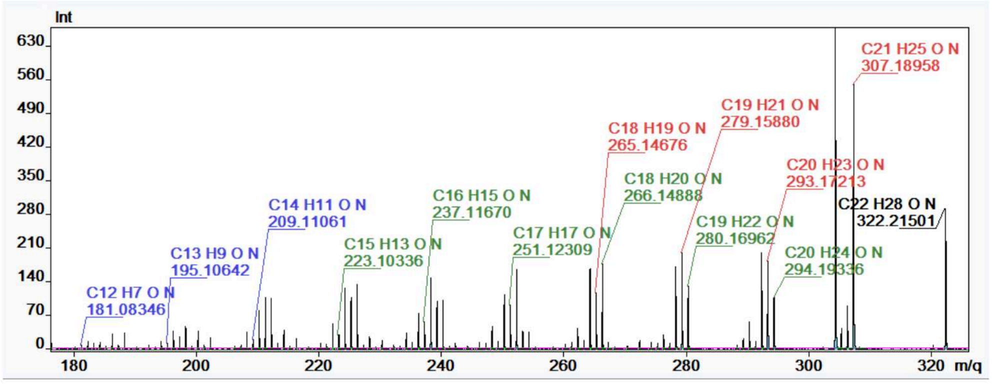

Figure 6.5.5: Measured mass spectrum of M_4. The fragment molecules originating from the structures shown in Figure 6.5.4 (c) and (d) are labeled with their elemental composition and mass-to-charge value in u/e. Blue labels are related to structure (a) and red labels relate to structure (b). Green labels can be produced by both structures. The black label marks the precursor molecule.

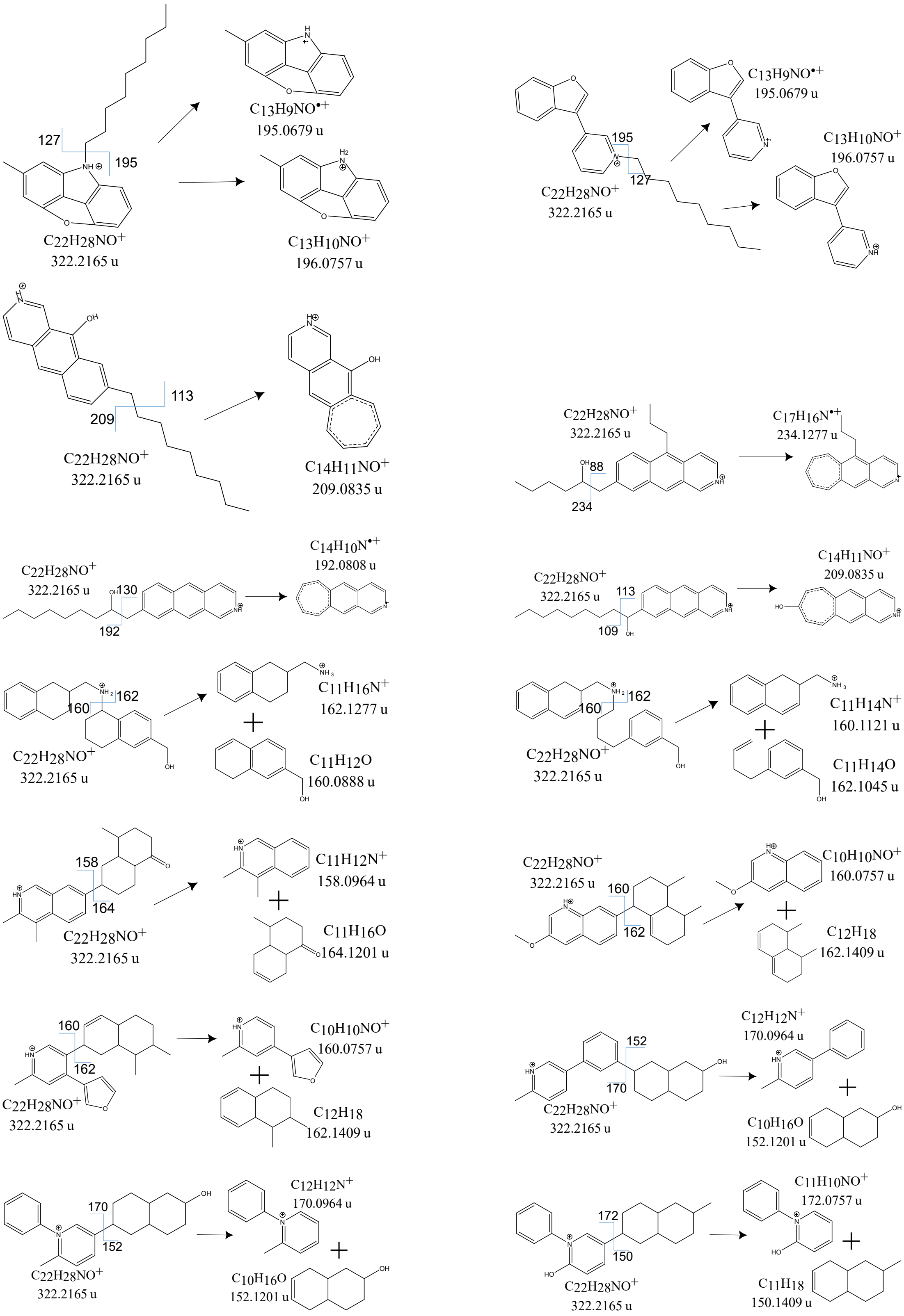

Figure 6.5.6: Identified structural formulas for the M$_4$ molecule C$_{22}$H$_{28}$ON$^+$, fragmentation processes and measured fragments. Structural formulas created by Jens Dreschmann from the WG Schrader.

7 Conclusion and Outlook

The MR-TOF-MS of this work was adapted and employed for ultra-high resolution analytical tandem mass spectrometry, for the first time. It has proven itself to be a versatile and useful tool up to MS^4 thanks to its ultra-high mass separation power and other excellent performance parameters.

The newly designed API and ion sources provide a reliable, efficient, and low-maintenance operation, even for viscous samples like heavy crude oil residue. Multiple ion sources can be used in parallel to add calibrants without causing chemical reactions, including two heated inlet capillaries for self-build nano-ESI and micro-ESI ion source, and a thermal ion source. Its radio-frequency carpet realizes a compact, efficient and fast solution to funnel the ions to the RFQ transport line, leading to an API transmission time of produced ions of only 0.5 ms.

The TOFControl software package was developed with features that were tailored to operate MR-TOF-MS devices from acquisition to data analysis. The software features automatically setting up the measurement by converting parameters like the desired mass range, resolving power and precursor mass to voltages and HV pulse sequences in real time. Its enhanced visualization features allow operators to predict, monitor and adapt the acquisition process in real time while information is stored in the background. It also provides further automated features, which are applied in real time during a measurement, like a time-of-flight drift correction, the scanning of measurement parameters, and automatic gain control. Furthermore, it assists during analysis with its time-resolved calibration technique for closed-path MR-TOF-MS and its enhanced elemental composition identification. In addition, acquisition procedures and analysis tools were developed to acquire a broad mass range of multiple hundred u/e, while retaining a high mass accuracy and mass resolving power. Its usefulness and versatility are also shown by its usage at MR-TOF-MS devices at particle accelerators, i.e. like MR-TOF-MS of the FRS Ion Catcher at GSI, Darmstadt, and the MR-TOF-MS of TITAN at TRIUMF in Vancouver.

The device routinely features a mass resolving power (FWHM) of up to 300 000 at a mass accuracy of 0.3 ppm and a linear dynamic range of 5 orders of magnitude with a sensitivity down to 10 mol/l. With the developed acquisition procedures, a mass range spanning multiple hundreds of u/e can be acquired. This was demonstrated with a spectrum of a crude oil sample with the mass-to-charge range of 300 - 550 u/e. Furthermore, molecules as heavy as human insulin (5810 u) have been analyzed. For tandem mass spectrometry, its re-trapping technique allows for a precursor mass separation power of up to 250 000 at an efficiency of 10 % or up to 100 000 with an efficiency of 80 %.

Tandem mass spectrometry of a sample of medium-heavy crude oil residue was performed. Four isobaric mass signals in a sample of medium-heavy crude oil were individually isolated within an isolation window of 10 mu and a suppression factor of 200. The 500 CID fragments with mass-to-charge values within 300 - 500 u of each of the four precursor molecules were analyzed and their elemental composition was identified.

For two of the isolated precursor molecules, $C_{23}H_{32}N^{+}$ and $C_{23}H_{28}ON^{+}$, 26 molecular structures were derived with the help of the Mass Spectrometry workgroup of the Max Planck Institute in Mülheim an der Ruhr, led by Prof. Dr. Schrader. This structural elucidation was only possible due to the unprecedented, ultra-high mass separation power of the device cleanly isolating the precursor molecules.

For future applications of the device, investigation of less understood crude oil samples as well as applications in life sciences, for example regarding oil spills or e-fuels, are envisioned.

List of Figures

List of Tables

Bibliography

[Ayet San Andrés et al. 2019]
Ayet San Andrés, Samuel et al. (June 2019). *High-resolution, accurate multiple-reflection time-of-flight mass spectrometry for short-lived, exotic nuclei of a few events in their ground and low-lying isomeric states.* Phys. Rev. C 99 (6), p. 064313.

[Back 1996]
Back, Thomas (1996). *Evolutionary algorithms in theory and practice: evolution strategies, evolutionary programming, genetic algorithms.* Oxford university press.

[Badertscher et al. 2001]
Badertscher, Martin et al. (2001). *A novel formalism to characterize the degree of unsaturation of organic molecules.* Journal of chemical information and computer sciences 41.4, pp. 889–893.

[Bergmann 2015]
Bergmann, J. (2015). *Entwicklung und Anwendung einer integrierten Systemsteuerung und Datenaufnahme für Flugzeitmassenspektrometer.* Master Thesis. Justus Liebig University Gießen.

[Bergmann 2023]
Bergmann, J. (2023). *TofControl Manual, A software for hardware control, data acquisition, and analysis at MR-TOF mass spectrometers.*

[Bruins 1998]
Bruins, Andries P (1998). *Mechanistic aspects of electrospray ionization.* Journal of Chromatography A 794.1-2, pp. 345–357.

[Choi et al. 2013]
Choi, Sung-Seen et al. (2013). *Fragmentation patterns of protonated amino acids formed by atmospheric pressure chemical ionization.* Rapid Communications in Mass Spectrometry 27.1, pp. 143–151.

[Dass 2007]
Dass, C. (2007). *Fundamentals of Contemporary Mass Spectrometry.* New Jersey: John Wiley & Sons.

[Dehmelt 1967]
Dehmelt, H. G. (1967). *Radiofrequency Spectroscopy of Stored Ions I: Storage.* Adv. At. Mol. Phys. 3, pp. 53–72.

[T. Dickel 2010]
Dickel, T. (2010). *Design and Commissioning of an Ultra-High-Resolution Time-of-Flight Based Isobar Separator and Mass Spectrometer.* PhD Thesis. Justus Liebig University Gießen.

[T. Dickel, Plass, et al. 2015]
Dickel, T., W. R. Plass, et al. (2015). *A high-performance multiple-reflection*

time-of-flight mass spectrometer and isobar separator for the research with exotic nuclei. Nucl. Instrum. Methods A 777, pp. 172–188.

[T. Dickel, M. I. Yavor, et al. 2017]
Dickel, T., M. I. Yavor, et al. (2017). *Dynamical time focus shift in multiple-reflection time-of-flight mass spectrometers.* Int. J. Mass Spectrom. 412, pp. 1–7.

[Timo Dickel et al. 2017]
Dickel, Timo et al. (June 2017). *Isobar Separation in a Multiple-Reflection Time-of-Flight Mass Spectrometer by Mass-Selective Re-Trapping.* J. Am. Soc. Mass Spectrom. 28.6, pp. 1079–1090.

[EU-directive 2019]
EU-directive (2019). *Richtlinie (EU) 2019/1258 der Kommission vom 23. Juli 2019 zur Änderung des Anhangs der Richtlinie 80/181/EWG des Rates hinsichtlich der Definitionen der SI-Basiseinheiten zwecks ihrer Anpassung an den technischen Fortschritt.* `https://eur-lex.europa.eu/legal-content/DE/TXT/PDF/?uri=CELEX:32019L1258`.

[Dole et al. 1968]
Dole, Malcolm et al. (1968). *Molecular beams of macroions.* The Journal of chemical physics 49.5, pp. 2240–2249.

[ETP electron multipliers 2013]
ETP electron multipliers (2013). *MagneTOF A New Class of Robust Sub-nanosecond TOF Detectors with Exceptional Dynamic Range.* dm167. PD-0257-A RevB. ETP electron multipliers.

[Glish et al. 2008]
Glish, G. L. and D. J. Burinsky (2008). *Hybrid Mass Spectrometers for Tandem Mass Spectrometry.* J. Am. Soc. Mass Spectrom. 19, pp. 161–172.

[Grinfeld et al. 2014]
Grinfeld, D. et al. (2014). *Space charge effects in an electrostatic mutireflection ion trap.* Eur. J. Mass Spectrom. 20, pp. 131–142.

[Jafari et al. 2011]
Jafari, MT, B Rezaei, and M Javaheri (2011). *A new method based on electrospray ionisation ion mobility spectrometry (ESI-IMS) for simultaneous determination of caffeine and theophylline.* Food chemistry 126.4, pp. 1964–1970.

[Jesch 2008]
Jesch, C. (2008). *Injektions-Ionenfallensystem für ein Multireflektions-Flugzeitmassenspektrometer.* Diploma Thesis. Justus Liebig University Gießen.

[Jesch 2016]
Jesch, C. (2016). *The Multiple-Reflection Time-of-Flight Isobar Separator for TITAN and Direct Mass Measurements at the FRS Ion Catcher.* PhD Thesis. Justus Liebig University Gießen.

[Jesch et al. 2015]
Jesch, C. et al. (2015). *The MR-TOF-MS isobar separator for the TITAN facility at TRIUMF.* Hyperfine Interact. 235, pp. 97–106.

[Karas et al. 2000]
Karas, M, U Bahr, and T Dülcks (2000). *Nano-electrospray ionization mass*

spectrometry: addressing analytical problems beyond routine. Fresenius' journal of analytical chemistry 366.6, pp. 669–676.

[Kendrick 1963]
Kendrick, Edward. (1963). *A Mass Scale Based on CH2 = 14.0000 for High Resolution Mass Spectrometry of Organic Compounds*. Analytical Chemistry 35.13, pp. 2146–2154. doi: 10.1021/ac60206a048.

[Ketabchi et al. 2019]
Ketabchi, Elham et al. (2019). *Integration of Fossil Fuel-based with Bio-based Industries: The Use of Waste Streams and Biomass to Produce Syngas and Added Value Products*. IFAC-PapersOnLine 52.1. 12th IFAC Symposium on Dynamics and Control of Process Systems, including Biosystems DYCOPS 2019, pp. 616–621. issn: 2405-8963. doi: https://doi.org/10.1016/j.ifacol.2019.06.131. url: https://www.sciencedirect.com/science/article/pii/S2405896319302186.

[Kind et al. 2007]
Kind, Tobias and Oliver Fiehn (2007). *Seven Golden Rules for heuristic filtering of molecular formulas obtained by accurate mass spectrometry*. BMC bioinformatics 8.1, pp. 1–20.

[Kondradi and S. Ayet n.d.]
Kondradi and S. Ayet (n.d.). *Generation of radiofrequency signals*. Private communication.

[Lang 2016]
Lang, Johannes Sebastian (2016). *Development of a Mobile High-Resolution Multiple-Reflection Time-of-Flight Mass Spectrometer for In-Situ Life Science Application*. PhD thesis. Justus Liebig University Gießen.

[Langmuir et al. 1925]
Langmuir, I. and K. H. Kingdon (1925). *Thermionic effects caused by vapours of alkali metals*. Proc. Roy. Soc. London (A) 107.741, pp. 61–79.

[Lippert 2016]
Lippert, W. (2016). *Further Development and Application of a Mobile Multiple-Reflection Time-of-Flight Mass Spectrometer for Analytical High-Resolution Tandem Mass Spectrometry*. PhD Thesis. Justus Liebig University Gießen.

[Major et al. 1968]
Major, F. G. and H. G. Dehmelt (1968). *Exchange-Collision Technique for the rf spectroscopy of stored ions*. Phys. Rev. 170.1, pp. 91–107.

[March et al. 2005]
March, R. E. and J. F. Todd (2005). *Quadrupole ion trap mass spectrometry*. Hoboken, New Jersey: John Wiley & Sons, Inc. isbn: 0-471-48888-7.

[Marshall et al. 2008]
Marshall, Alan G and Ryan P Rodgers (2008). *Petroleomics: Chemistry of the underworld*. Proceedings of the National Academy of Sciences 105.47, pp. 18090–18095.

[Mathieu 1868]
Mathieu, Émile (1868). *Mémoire sur le mouvement vibratoire d'une membrane de forme elliptique*. Journal de mathématiques pures et appliquées 13, pp. 137–203.

[McLachlan 1947]
McLachlan, N. W. (1947). *Theory and Application of Mathieu Functions.* Oxford: Oxford University Press.

[Murray et al. 2013]
Murray, Kermit K et al. (2013). *Definitions of terms relating to mass spectrometry (IUPAC Recommendations 2013).* Pure and Applied Chemistry 85.7, pp. 1515–1609.

[Nelder et al. 1965]
Nelder, John A and Roger Mead (1965). *A simplex method for function minimization.* The computer journal 7.4, pp. 308–313.

[Panda et al. 2007]
Panda, Saroj K, Jan T Andersson, and Wolfgang Schrader (2007). *Mass-spectrometric analysis of complex volatile and nonvolatile crude oil components: a challenge.* Analytical and bioanalytical chemistry 389.5, pp. 1329–1339.

[Paul et al. 1956]
Paul, Wolfgang and Helmut Steinwedel (1956). *Verfahren zur Trennung bzw. zum getrennten Nachweis von Ionen verschiedener spezifischer Ladung.*

[Plass 1997]
Plass, W. R. (1997). *Aufbau eines Flugzeitmassenspektrometers zur Analyse von flüchtigen organischen Verbindungen bei geringem Partialdruck.* Diploma Thesis. Justus Liebig University Gießen.

[Plass 2001]
Plass, W. R. (2001). *The Dependence of RF Ion Trap Mass Spectrometer Performance on Electrode Geometry and Collisional Processes.* PhD Thesis. Justus Liebig University Gießen.

[Plass, T. Dickel, Ayet San Andrés, et al. 2015]
Plass, W. R., T. Dickel, S. Ayet San Andrés, et al. (2015). *High-performance multiple-reflection time-of-flight mass spectrometers for research with exotic nuclei and for analytical mass spectrometry.* Phys. Scr. T 166, p. 014069.

[Plass, T. Dickel, Purushothaman, et al. 2013]
Plass, W. R., T. Dickel, S. Purushothaman, et al. (2013). *The FRS Ion Catcher - A Facility for High-Precision Experiments With Stopped Projectile and Fission Fragments.* Nucl. Instrum. Methods B 317, pp. 457–462.

[Plass, T. Dickel, and Scheidenberger 2013]
Plass, W. R., T. Dickel, and C. Scheidenberger (2013). *Multiple-Reflection Time-of-Flight Mass Spectrometry.* Int. J. Mass Spectrom. 349, pp. 134–144.

[Rayleigh 1882]
Rayleigh, Lord (1882). *XX. On the equilibrium of liquid conducting masses charged with electricity.* The London, Edinburgh, and Dublin Philosophical Magazine and Journal of Science 14.87, pp. 184–186.

[Reiter 2015]
Reiter, M. P. (2015). *Pilot Experiments with Relativistic Uranium Projectile and Fission Fragments Thermalized in a Cryogenic Gas-Filled Stopping Cell.* PhD Thesis. Justus Liebig University Gießen.

[Reuben et al. 1996]
Reuben, A .J. et al. (1996). *Ion trajectories in exactly determined quadrupole fields.* Int. J. Mass Spectrom. Ion Proc. 154.1, pp. 43–59.

[S. Ayet n.d.]
S. Ayet (n.d.). *Fast high voltage switches.* Private communication.

[Schrader 2013]
Schrader, W. (2013). *Research Report.* url: https://www.kofo.mpg.de/268371/Research-Report-Schrader-2011-2013.pdf.

[Schury et al. 2009]
Schury, P. et al. (2009). *Multi-reflection time-of-flight mass spectrograph for short-lived radioactive ions.* Eur. Phys. J. A 42, pp. 343–349.

[Stafford Jr et al. 1992]
Stafford Jr, George C, Dennis M Taylor, and Stephen C Bradshaw (Apr. 1992). *Method of increasing the dynamic range and sensitivity of a quadrupole ion trap mass spectrometer.* US Patent 5,107,109.

[Stresau et al. 2006]
Stresau, D. et al. (2006). *A new class of robust sub-nanosecond TOF detectors with high dynamic range. 54th ASMS Conference on mass spectrometry and applied topics.* Seattle, Washington.

[Taylor 1964]
Taylor, Geoffrey Ingram (1964). *Disintegration of water drops in an electric field.* Proceedings of the Royal Society of London. Series A. Mathematical and Physical Sciences 280.1382, pp. 383–397.

[Toker et al. 2009]
Toker, Y. et al. (2009). *The kick-out mass selection technique for ions stored in an electrostatic ion beam trap.* J. Instrum. 4, P09001.

[Tolmachev, Chernushevich, et al. 1997]
Tolmachev, A. V., I. V. Chernushevich, et al. (1997). *A collisional focusing ion guide for coupling an atmospheric pressure ion source to a mass spectrometer.* Nucl. Instrum. Methods B 124, pp. 112–119.

[Tolmachev, Udseth, et al. 2000]
Tolmachev, A. V., H. R. Udseth, and R. D. Smith (2000). *Charge Capacity Limitations of Radio Frequency Ion Guides in Their Use for Improved Ion Accumulation and Trapping in Mass Spectrometry.* Analytical Chemistry 72.5, pp. 970–978. doi: 10.1021/ac990729u. eprint: http://pubs.acs.org/doi/pdf/10.1021/ac990729u. url: http://pubs.acs.org/doi/abs/10.1021/ac990729u.

[units 2006]
units, The international system of (2006). *de la Conventon d Mètre, O.I. (2006 (updated in 2014)).* http://centaur.reading.ac.uk/7226/1/si_brochure_8.pdf.

[Vetere et al. 2018]
Vetere, Alessandro et al. (2018). *Studying the fragmentation mechanism of selected components present in crude oil by collision-induced dissociation mass spectrometry.* Rapid Communications in Mass Spectrometry 32.24, pp. 2141–2151.

[Wada et al. 2003]
Wada, M. et al. (2003). *Slow RI-beams from projectile fragment separators.* Nucl. Instrum. Methods B 204, pp. 570–581.

[Weizsäcker 1935]
Weizsäcker, C. F. v. (1935). *Zur Theorie der Kernmassen.* Z. Phys. 96 (7), pp. 431–458.

[Wells et al. 2005]
Wells, J Mitchell and Scott A McLuckey (2005). *Collision-induced dissociation (CID) of peptides and proteins.* Methods in enzymology 402, pp. 148–185.

[Wilm et al. 1994]
Wilm, Matthias S and Matthias Mann (1994). *Electrospray and Taylor-Cone theory, Dole's beam of macromolecules at last?* International Journal of Mass Spectrometry and Ion Processes 136.2-3, pp. 167–180.

[Wolf, Errit, et al. 2011]
Wolf, R. N., M. Errit, et al. (2011). *A multi-reflection time-of-flight mass separator for isobaric purification of radioactive ion beams.* Hyperfine Interact. 199, pp. 115–122.

[Wolf, Marx, et al. 2012]
Wolf, R. N., Gerrit Marx, et al. (2012). *Static-mirror ion capture and time focusing for electrostatic ion-beam traps and multi-reflection time-of-flight mass analyzers by use of an in-trap potential lift.* Int. J. Mass Spectrom. 313, pp. 8–14.

[Wollnik et al. 1990]
Wollnik, H. and M. Przewloka (1990). *Time-of-Flight Mass Spectrometers With Multiply Reflected Ion Trajectories.* Int. J. Mass Spectrom. Ion Processes 96, pp. 267–274.

[Yamaguchi et al. 2021]
Yamaguchi, T. et al. (2021). *Masses of exotic nuclei.* Progress in Particle and Nuclear Physics 120, p. 103882. issn: 0146-6410. doi: https://doi.org/10.1016/j.ppnp.2021.103882. url: https://www.sciencedirect.com/science/article/pii/S0146641021000363.

[M. Yavor 2009]
Yavor, M. (2009). *Optics of Charged Particle Analyzers.* Ed. by P. W. Hawkes. Vol. 157. Advances in Imaging and Electron Physics. Amsterdam: Academic Press, Elsevier.

[M. I. Yavor 2010]
Yavor, M. I. (2010). *High quality axially symmetric mirror for shuttle-type MR TOF spectrometers.* Internal report.

[M. I. Yavor 2014]
Yavor, M. I. (2014). *Theoretical concept of the time focus shift-ing mode.*

[M. I. Yavor et al. 2015]
Yavor, M. I. et al. (2015). *Ion-optical design of a high-performance multiple-reflection time-of-flight mass spectrometer and isobar separator.* Int. J. Mass Spectrom. 381-382, pp. 1–9.

[Zhu et al. 2022]
Zhu, Zhiwen et al. (2022). *Recent advances in chemical and biological degradation of*

spilled oil: A review of dispersants application in the marine environment. Journal of Hazardous Materials 436, p. 129260. ISSN: 0304-3894. DOI: `https://doi.org/10.1016/j.jhazmat.2022.129260`. URL: `https://www.sciencedirect.com/science/article/pii/S0304389422010500`.

Acknowledgements

I would like to honestly thank the following people who made writing this thesis possible.

Prof. Dr Christoph Scheidenberger and Prof. Dr Dr h.c. Hans Geissel offered me the opportunity to join the IONAS workgroup and supported me during my studdies. Dr Wolfgang Plaß gave me excellent supervision and showed me how to work accurately and analytically. Dr Timo Dickel for always giving excellent advice during my work in the lab and the fruitful scientific discussion.

I thank Prof. Dr Wolfgang Schrader, who leads the workgroup Massenspektrometrie at the MPI für Kohleforschung in Mülheim an der Ruhr and his staff members Alessandro Vetere and Jens Dreschmann for this collaboration, their helpful insights on analytical mass spectrometry and of course the analysis of the acquired data presented in this work.

Regarding the experimental setup of the tandem-MR-TOF-MS, I thank Wayne Lippert and Johannes Lang, who implemented and investigated most of the fundamental components and introduced me to working in the lab. I also thank my coworkers Tobias Murböck and Lisa Marie Brück, who helped me with acquiring and analyzing the data of the crude oil sample and Jan Hofmann who contributed largely to the FSS feature of the TOFControl software. For helping with simulation and CAD designs of the API I would also like to thank my coworkers Ivan Miskun, Jens Ebert and Thomas Wasem, who designed most of the technical drawings.

For the software development, I thank Alexander Pikhtelev (MAc) and Christian Jesch (trigger system) for providing the basis for many of the TOFControl features and willingly sharing their code or VIs. In general, I am grateful to the users of the TOFControl software for their feedback, which improved the quality of the software, their patience, which allowed me the time to do that, and their gratitude.

The secretary of the IONAS workgroup, Evelin Prinz, also has my gratitude for all the quick and fast help with any bureaucratic or organizational matter. I also thank the team of the *Feinmeschanische Werkstatt der physikalischen Institute* for their fast and precise work at machining the parts of the experimental setup and providing support and repairs.

I thank my other colleagues of the IONAS workgroup in Gießen for helping without hesitation whenever I needed help with theory, testing or labwork and in general being very supportive: Gabriella Kripko-Koncz, Daler Amanbayev, Heinrich Wilsenach, Makar Simonov, Florian Greiner, Moritz Pascal Reiter, Kriti Mahajan, Jiajun Yu, Marcel Diwisch, Ann-Kathrin Rink, Christine Hornung, Lizzy Gröf, and Samuel Ayet San Andrés.

Außerdem möchte ich mich herzlich bei meiner Mutter dafür bedanken, welche immer an mich geglaubt und mich unterstützt hat. Ich kann mir keine bessere Mutter vorstellen.

And last, but most importantly, I thank my mother for always supporting and believing in me and being the best mother I can imagine.

Versicherung

Studiengang: ____

Name: ____

Matrikelnummer: _ _ _ _ _ _ _

Erklärung zur Abschlussarbeit (Thesis)

Ich erkläre hiermit, dass ich die Thesis selbständig verfasst und keine anderen als die angegebenen Hilfsmittel benutzt habe. Die Stellen der Arbeit, die anderen Werken im Wortlaut oder dem Sinn nach entnommen sind, sind durch Angaben und Quellen kenntlich gemacht. Dies gilt auch für Zeichnungen, Skizzen, bildliche Darstellungen und dergleichen.

Weiterhin erkläre ich, dass die Abschlussarbeit (Thesis) noch nicht im Rahmen einer staatlichen oder anderen Prüfung (z. B. als Magister-, Diplom- oder Staatsexamensarbeit) eingereicht wurde.

Mit der Überprüfung meiner Abschlussarbeit mittels einer Anti-Plagiatssoftware bin ich einverstanden und reiche die Abschlussarbeit auch in digitaler Form ein.

_____________________ (Ort, Datum)

______________________________ (eigenhändige Unterschrift)